Gonçalo Laurentino Gomes

Licenciado em Engenharia Geológica

Spatial simulation of the W-Sn ore grades of São Pedro das Águias skarn mineral deposit (Tabuaço, northern Portugal)

Dissertação para obtenção do Grau de Mestre em Engenharia Geológica

Orientador: Doutor José António de Almeida, Professor Associado, FCT/UNL
Co-orientador: Mestre Filipa Vieira Matias, Estudante de Doutoramento, FCT/UNL

Júri:

Presidente: Doutor Martim Afonso Ferreira de Sousa Chichorro
Arguente: Doutor António Jorge Gonçalves de Sousa
Vogal: Doutor José António de Almeida

FACULDADE DE CIÊNCIAS E TECNOLOGIA
UNIVERSIDADE NOVA DE LISBOA

Junho 2016

Gonçalo Laurentino Gomes

Licenciado em Engenharia Geológica

Spatial simulation of the W-Sn ore grades of São Pedro das Águias skarn mineral deposit (Tabuaço, northern Portugal)

Dissertação para obtenção do Grau de Mestre em Engenharia Geológica

Orientador: Doutor José António de Almeida, Professor Associado, FCT/UNL
Co-orientador: Mestre Filipa Vieira Matias, Estudante de Doutoramento, FCT/UNL

Caparica

2016

Spatial simulation of the W-Sn ore grades of São Pedro das Águias skarn mineral deposit (Tabuaço, northern Portugal)

"*If the results disagree with informed opinion, do not admit a simple logical interpretation, and do not show up clearly in a graphical presentation, they are probably wrong. There is no magic about numerical methods, and many ways in which they can break down. They are a valuable aid to the interpretation of data, not sausage machines automatically transforming bodies of numbers into packages of scientific fact.*"

F. H. C. Marriot

ACKNOWLEDGMENTS

In this part of the present work I would like to thank to all entities and people who have contributed directly, or not, to the rise, development and conclusion of this study. Consequently, in my opinion, this is maybe the most difficult section of this thesis, because I am always thinking about: “I must not forget of anyone!”. Thus, if this happens (which I hope not), I would like to apologize in advance to those I have forgotten, and leave written down that all were important to me and to the conclusion of my master thesis and, as consequence, to ending of this important stage of my life.

Therefore, a big and heartfelt thank you to the following:

To Colt Resources Inc. for gently providing all data, informations and help needed, for all the reliance and for having authorized the publication of this master thesis and previous scientific publications about this work. Without the data of this company the present study would not be possible.

To *FCT – Fundação para a Ciência e Tecnologia* (Science and Technology Fundation) for funded this study through the Project UID/GEO/04035/2013.

To the Faculty of Sciences and Technology of NOVA University of Lisbon and to its Earth Sciences Department for having accepted and hosted me for many years, to study and develop my hard skills.

To Professor José António for this opportunity and excellent orientation. Thank you also for your constant motivation, imagination, availability, patience and professionalism, for all the answered questions, our published works and friendship. All the last points and qualities motivated me to work more and to believe in the final result. I am really grateful!

To Filipa for the given orientation, advices, our published works, and discussions, suggestions and revisions of the models and texts. Thank you for having always been the bridge between me and the professors’ hard acknowledgment, and me and the practical and complex mining and business reality. I am also thankful for the constant availability and built friendship!

To Professor Martim for all the geological discussions, suggestions and revisions of the model and texts even without being my supervisor. I am also grateful for your availability, patience, advices, sympathy, explanations, answered questions, our published works and friendship. Thank you Professor Martim!

To the remaining professors and staff of the Earth Sciences Department of Faculty of Sciences and Technology of NOVA University of Lisbon who marked my academic formation, specially to Professor Ana Paula, Graça, Sofia, Zenaide, Joaquim, Kullberg, Nuno, Paulo and Pedro and to Fátima. Thank you all for the constant conversations, discussions, sharing, help and motivation provided and, mostly, demonstrated friendship.

To Professor Maria dos Anjos of the Faculty of Sciences of the University of Porto for the healthy

discussion about the studied region and for providing Doctor Manuel Bernardo de Sousa's Ph.D. thesis.

To Now Club's staff and colleagues who improved greatly my English skills, specially to Ivan and Super Mike. Without you maybe I would never have reached to this ambitious goal, of writing my thesis completely in English. Thanks a lot!

To my colleagues and friends of the faculty, specially to Catarina, Daniela, Inês, Inês, Laura, Lúcia, Marta, Rita, André, Brasil, Brissos, Chicão, David, Estevens, Gonçalo, Luís, Mário, Pedro, Ricardo, Ricardo and Sanches. Thank you all for all conversations and discussions, funny and relaxed moments, harder and softer projects and, mainly, for the created and special friendships!

To my homeland and unforgotten friends Ana, Daniela, Diana, Cátia, little Matilde, David, Fábio, Flávio, Hugo, Renato, Rui, Rui and Rui. Thank you for all the unconditional friendship, constant support and conversations, and for being always with me in the better and the worst moments!

Lastly, the last are always the first, to my family. To my bother Gil, my grandmothers Jesus and Maria, my grandfathers, Chico and Tóino, who God has, my godson Rui and to my aunts, uncles and cousins for the constant support, encouragement, love and open heart. Finally, a special and great thanks to my parents Bina and Tó Manel for all the unconditional love, support and encouragement, for the constant parents' pride, patience and comprehension in spite of everything, and for this big opportunity, my academic formation. I am who I am because of you two.

ABSTRACT

The purpose of this study is the W-Sn grades simulation of São Pedro das Águias skarn ore deposit (Tabuaço, northern Portugal). This skarn deposit hosts a mineralization of scheelite and cassiterite. The grades modelling constrained by lens-shaped skarns is challenging, because they are numerous, thin, constrained to the structure shape and orientation, and recognized only in the drill-holes without indication of interconnections. Despite of the complexity, the proposed methodology constructs a geological model of the lens-shaped skarns, and generates a conditional model of the grades.

The geological model construction begins with the automatic simulation of scenarios of the interconnections between the lens-shaped intersected by the drill-holes, conditioned to the orientation of the structure. For the simulated geometry scenarios represented by polylines in several cross-sections thicknesses are added according to the drill-cores, and the skarn relative proportion of each block is evaluated. Finally, the grid blocks between the cross-sections are filled using direct the DSS algorithm with local means from the skarn proportion variable (continuous variable). So long as the skarn thicknesses are much smaller than the blocks size, the morphological model reports the skarn proportion variable. The W-Sn grades model encompasses the local histograms estimation conditional to the geological model, and uses the PFS algorithm to generate the final images. The local histograms estimation results of a grades mixture according to the calculated skarn proportion between each block, and of a simple W-Sn simulated images conditional to the skarn and no-skarn lithological groups.

The simulated grades are finally compared with the equivalent resources obtained by ordinary kriging. The simulated images enable the evaluation of the local uncertainty, and may be used for mine planning and optimizations.

Keywords: skarn ore deposits, Bateiras Formation, W-Sn grades model, lens-shaped skarns, spatial simulation, uncertainty evaluation

RESUMO

O objectivo deste estudo é a simulação dos teores de W-Sn do depósito de *skarn* de São Pedro das Águias (Tabuaço, norte de Portugal). Este depósito de *skarn* possui mineralizações de scheelite e cassiterite. A modelação de teores condicionada a lentículas de *skarn* é um desafio, porque estas são numerosas, finas, condicionadas à forma e orientação da estrutura e reconhecidas só nas sondagens, sem indicação de conexões entre as mesmas. Apesar da complexidade, a metodologia proposta constrói um modelo geológico das lentículas de *skarn* e gera um modelo condicional de teores.

A construção do modelo geológico inicia-se com a simulação automática de cenários das conexões das lentículas reconhecidas nas sondagens, condicionadas à orientação da estrutura. Para os cenários simulados da geometria, representados por *polylines* em vários perfis, é adicionada uma espessura de acordo com as sondagens e é avaliada a proporção relativa de *skarn* dentro de cada bloco da malha. Finalmente, os blocos entre perfis são preenchidos por SSD com médias locais a partir da variável proporção de *skarn* (variável contínua). Visto que a espessura das lentículas de *skarn* é mais reduzida que a dimensão dos blocos, o modelo morfológico reporta a variável proporção de *skarn*. O modelo de teores de W-Sn envolve a estimação de histogramas locais condicionais ao modelo geológico e utiliza a PFS para gerar as imagens finais. A estimação dos histogramas locais resulta de uma mistura de teores de acordo com a proporção de *skarn* calculada entre cada bloco e origina simples imagens simuladas de W-Sn condicionais para os tipos de rocha *skarn* e *no-skarn*.

Os teores simulados são finalmente comparados com os recursos equivalentes obtidos por krigagem normal. As imagens simuladas permitem a avaliação da incerteza local e podem ser utilizadas para o planeamento e optimização mineira.

Palavras-chave: depósitos de minério de *skarn*, Formação de Bateiras, modelo de teores de W-Sn, lentículas de *skarn*, simulação espacial, avaliação da incerteza

CONTENTS

FIGURES

TABLES

LIST OF ABBREVIATIONS, ACRONYMS AND INITIALS

General

3D – Three-dimensional

AD – *Anno Domini*

Ag – Silver

Al – Aluminum

Au – Gold

As – Arsenic

Ba – Barium

Be – Beryllium

Bi – Bismuth

BC – Before Christ

Ca – Calcium

Cd – Cadmium

Ce – Cerium

Co – Cobalt

CO_2 – Carbon dioxide

Colt – Colt Resources Inc.

Cr – Chromium

Cu – Copper

ex. gr. – *Exempli gratia* (for exemple or for instance)

et al. – *Et alii* (and other authors)

etc. – *Et cetera* (and others or and other things)

EU – European Union

Fe – Iron

Ga – Gallium

Ge – Germanium

H_2O – Water

ha – Hectare

HREE – Heavy Rare Earth Elements

i.e. – *Id est* (that is or in other words)

K – Potash

kbar – Kilobar

km – Kilometers

La – Lanthanum

Li – Lithium

LREE – Light Rare Earth Elements

m – Meters

Ma – Million years

mm – Millimeters

Mg – Magnesium

Mn – Manganese

Mo – Molybdenum

Mt – Million tonnes

Na – Sodium

Nb – Niobium

Ni – Nickel

O – Oxygen

P – Phosphorus

Pb – Lead

PGM – Platinum Group Metals

Rb – Rubidium

S – Sulfur

Sb – Antimony

Sc – Scandium

Se – Selenium

SEREM – *Société d'Études de Recherches et d'Exploitations Minières* (Research and Mining Exploitatiojn Studies Society)

SFM – *Serviço de Fomento Mineiro* (Mining Development Service)

Si – Silicon

Sn – Tin

SPE – *Sociedade Portuguesa de Empreendimentos* (Ventures Portuguese Society)

Sr – Strontium

t – Tonnes

Ta – Tantalum

Te – Tellurium

Th – Thorium

Ti – Titanium

Tl – Tallium

U – Uranium

UV – Ultra Violet

V – Vanadium

W – Tungsten or wolfram

WO_3 – Tungsten trioxide

wt% – Weight percentage

Y – Iridium

Zn – Zinc

Zr – Zirconium

Geological related

APL – Aplites

BLS – Black/dark grey schists

BLX – Biotite schists

CAV – Solution cavities

CLS – Core losses

CRB – Carbonates or calcschists

CRV – Calcite veins

CSR – Calcsilicate lithologies or poorly developed skarns

D_1 – First Variscan deformation phase

D_2 – Second Variscan deformation phase

D_3 – Third Variscan deformation phase

FBX – Faults breccia

FLG – Faults filled with gauge

FLP – Probable faults

FLT – Obvious faults

GNT – Granites

OVB – Overburden

QZV – Quartz veins

SKL – Skarns layered

SKM – Skarns layered to massive

SKN – Skarns indifferentiated

Geostatistical related

BLUE – Best Linear Unbiased Estimator

CCDF – Conditional Cumulative Distribution Function

CDF – Cumulative Distribution Function

CoDSS – Direct Sequential Co-Simulation

CoSGS – Sequential Gaussian Co-Simulation

DEM – Digital Elevation Model

DSS – Direct Sequential Simulation

DTM – Digital Terrain Model

F – Factor

F^{SK} – Skarn relative proportion

F^{NSK} – No-skarn relative proportion

IK – Indicator Kriging

KED – Kriging with External Drift

OCoK – Ordinary Co-Kriging

OK – Ordinary Kriging

PC – Principal Component

PCA – Principal Component Analysis

PFS – Probability Field Simulation or P-Field Simulation

SCoK – Simple Co-Kriging

SICoS – Sequential Indicator Co-Simulation

SGS – Sequential Gaussian Simulation

SIS – Sequential Indicator Simulation

SK – Simple Kriging

1. Introduction

The present section has the aim of reporting the setting, goals and organization of this work. The geographical, geomorphological and historical setting of the case study area or region, *i.e.*, the São Pedro das Águias skarn ore deposit, are also presented.

1.1. Setting and goals of the thesis

The main goal of this thesis is to propose and check a methodology that generates a W and Sn grades simulated model conditional to a morphological model, with inclusion of geological information into the construction of the later. The methodology was tested in the São Pedro das Águias skarn ore deposit (Tabuaço, northern Portugal), which hosts a mineralization of scheelite ($CaWO_4$) and cassiterite (SnO_2). The present deposit is part of the Tabuaço Tungsten Project, which contains an on-going Experimental Mining License. Colt owns 100% of the rights on the concession covering the Tabuaço Tungsten Project and, consequently, the Tabuaço Experimental Mining License was granted to the company (O'Donovan *el al.*, 2012, Beare and MacDougall, 2013).

W, also known as tungsten or wolfram, is a transition metal with atomic number 74 and of both 6^{th} group and period. The former came from the Swedish term *tung sten*, which means heavy stone, respectively, owing to its high density. The the latter derived from the German words *wolf rahm* that mean wolf lather, respectively. This meaning becomes from the Middle Ages because it was harder to obtain Sn from the ores when they also contained W, forming some lather that seemed "to eat" the Sn. This chemical element is normally in the solid phase and owns a high density of about 19.3 g/cm^3 and the highest melting point of 3410°C (Moura and Velho, 2012).

In the Earth's crust, W is widespread with an average grade of 1 ppm (Dill, 2010) and can be found in forty-five minerals (Moura and Velho, 2012). However, economically, W may just be recovered from wolframite (76 wt% W) and scheelite (80 wt% W) (Dill, 2010; Mora and Velho, 2012). These two are mined from 0.2 to 0.4% WO_3 of ore grade. The presence of Au, Ag, Sc, Nb and Ta increase the value of the W ore; while if Sn > 1.5%, As > 0.2%, P > 0.03%, S > 0.3% and the existence of Sb, Cu, and Mo may be detrimental to the quality of the ore (Dill, 2010). The applications of W pass by W carbide to harden alloys, ferrotungsten, stainless steel/high-grade steel, W filaments for lamps, thermionic uses, and heavy-duty tools (such as drill-bits, by the recycling of steel alloyed with W and powder-metallurgical material, as W carbide) (Dill, 2010; Moura and Velho, 2012).

Sn is a post-transition metal with atomic number 50 of the group 14 and the period 5. It is known as tin, which came from the Latin word *stannum*. Sn is also normally in the solid phase and has a density of about 7.3 g/cm^3 and a low melting point of 232°C (Moura and Velho, 2012). In the Earth's crust, Sn is more widespread than W, averaging 35 ppm (Dill, 2010) and can be found in

ninety-four mienerals (Moura and Velho, 2012). However, economically, it can just be recoverd from cassiterite (78.8 wt% Sn) (Dill, 2010; Moura and Velhor, 2012). Sn primarily was used for food containers, in form of Sn- and tern-plates; however, the uses of Sn on nowadays are in form of alloys (for instance, bronze, brass and babbitt metal, with Sb and Cu in the glass and ceramic industries), solders, tinning steel sheets, for electronic devices (for example LCD displays), and pigments (Dill, 2010; Moura and Velho, 2012).

According to Kwak (1987), both W and Sn deposits occur in belts all over the world, which are mainly distributed by the western part of North America (Appalachian Sn-W Belt), northern South America (Eastern Brazilian and Ondonro-Guinean Brazilian Belts), Europe (Armorican Belt), Africa (Nigerian and Liberian-Moroccan Belts), eastern Asia and eastern Australia (Figure 1.1). These belts can also be grouped into a global-scale by plate tectonic reconstructions, for example the Appalachian Sn-W Belt match with the Armorican Belt, and the Eastern Brazilian and Ondonro-Guinean Brazilian Belts with the Nigerian and Liberian-Moroccan Belts (Kwak, 1987). The deposits of W and Sn of the Iberian Peninsula are inserted in a W and Sn metallogenic province. In Portugal, in turn, this metallogenic province is situated in the Galiza–Trás-os-Montes Zone and Central Iberian Zone (Martins, 2012) to the east of the Porto-Tomar Shear Zone and to the northeast of the Juromenha Thrust Fault (Neiva, 1944, *in* Ribeiro and Pereira, 1982; Thadeu, 1977), with exception of the polymetallic sulphide deposits situated in the Pyrite Belt of the South Portuguese Zone (Ribeiro and Pereira, 1982; Martins, 2012). The major part of these deposits are directly or indirectly associated with granite intrusions and inside of their contact metamorphic aureoles (Martins, 2012).

Scheelite and the cassiterite are the two most important minerals for the present case study. Scheelite ($CaWO_4$) is a calcic tungstate mineral, in which contains 13.92% of Ca, 63.85% of W, and 22.23% of O. According to Dana's classification (Klein and Dutrow, 2008) this mineral is an anhydrous molybdate and tungstate, in which Mo may substitute W forming partial series between scheelite and powellite ($CaMoO_4$). Scheelite has a Mohs hardness between 4.5-5, a specific gravity of 5.9-6.1, and presents fluorescence, being an useful characteristic for prospection when UV light is used. About cassiterite, it is a Sn (SnO_2) oxide mineral, according to Dana's classification (Klein and Dutrow, 2008), including 78.6% of Sn and 21.4% of O. Sn can be substituted by Nb and Ta in the mineral, and it may contain small amounts of Fe^{3+}. This mineral has a Mohs hardness of about 6-7, and a specific gravity of 6.8-7.1.

According to the EU (DG-ENTR, 2010, 2014), the variety and stock of materials used in the existent products has growth during the recent years. Thus, the EU defined a list of fifty-four non-energy and non-agricultural raw materials that it considers fundamental to Europe's economy, growth and jobs, and essential for maintaining and improving people's quality of life (DG-ENTR, 2014). In this list there were defined critical and non-critical raw materials by having a higher or lower economic importance and the risk associated with their supply (DG-ENTR, 2010, 2014). Therefore, according to their supply risk and economic importance, a threshold of 1.0 to the former

and of 5.0 to the latter was defined, in which the raw materials that are below these thresholds are non-critical and those that are above are critical (Figure 1.2 and Table 1.1). Hence, one important point that indicates if one raw material is critical or not, is the technological change and the rapid diffusion of new technologies (DG-ENTR, 2010).

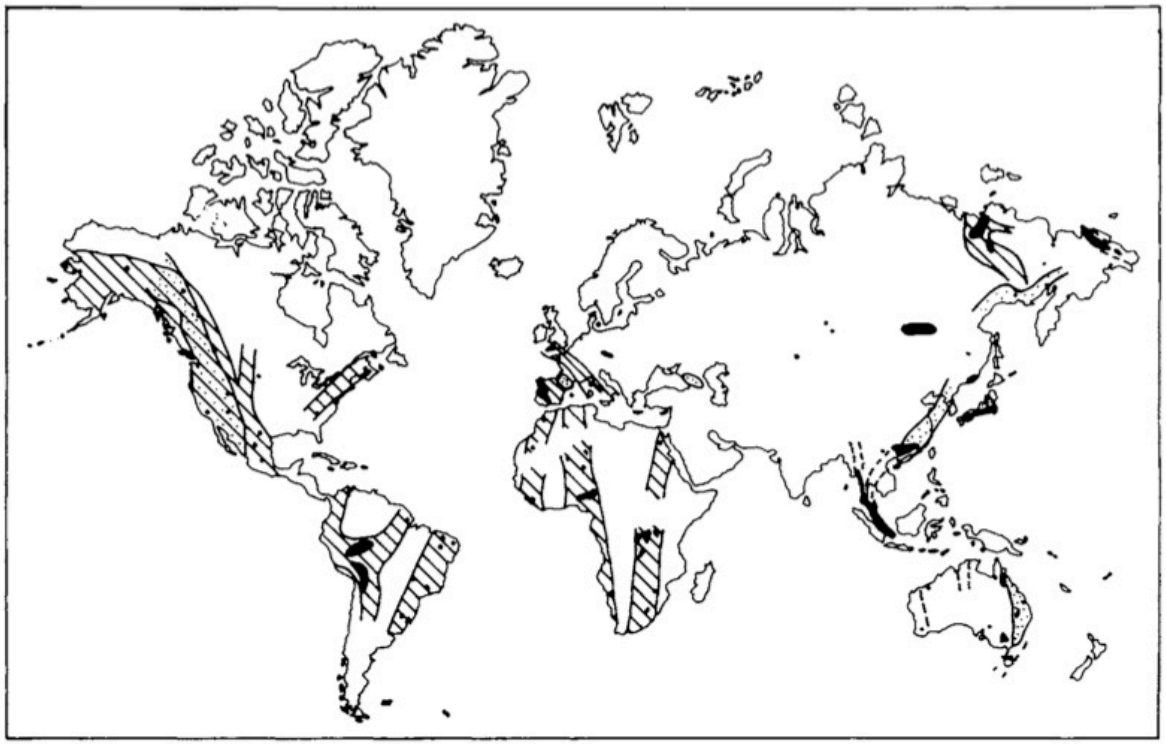

Figure 1.1 – World's sketch showing the distribution of W- and Sn-bets; cross-hatched and black areas – Sn-belts; dotted areas – W-belts (Kwak, 1987).

Both W and Sn metals are raw materials included into the EU's list (Figure 1.2 and Table 1.1). W is clearly considered a critical raw material with less than 3% supply in the EU (Figure 1.2 and Table 1.1; DG-ENTR, 2010, 2014), being the main resulting product of São Pedro das Águias possible exploitation. According to DG-ENTR (2010), the reasons for the criticality of W are: (1) the supply is dominated by China (that has the largest reserves in the world), which may cause a price and quantitative disruption; (2) growing risks a "predatory" behaviour of that country on the W scrap market; (3) limited substitute alternatives by the cost of the materials/technologies, lesser performance, and less friendly environmental options; and (4) if EU value chain is broken there is a loss of know-how in the world, because the EU is the leader in the development of a lot of W products for many industries (such as automotive), resulting in a total dependence from abroad. In the other hand, Sn is not considered a critical raw material (Figure 1.2 and Table 1.1), however its supply in the EU is less than 1% (Table 1.1) and it is placed close to the supply risk threshold (Figure 1.2). This fact makes Sn a possible by-product, or a minor one of São Pedro das Águias

possible exploitation. Sn may even turn critical, because of its proximity to the supply risk threshold.

The data base used to support this methodology contains informations about the São Pedro das Águias skarn ore deposit drilling campaign, and was gently provided by Colt. It includes informations about the drill-hole cores collected, such as their spatial position, lithologies, and element grades.

A set of computer software was used to process all the information and to develop the present work. The utilized software was: (1) an automatic algorithm proposed by Simões (2014) adapted to the case study; (2) GeoMS; (3) ANDAD; and (4) Move™.

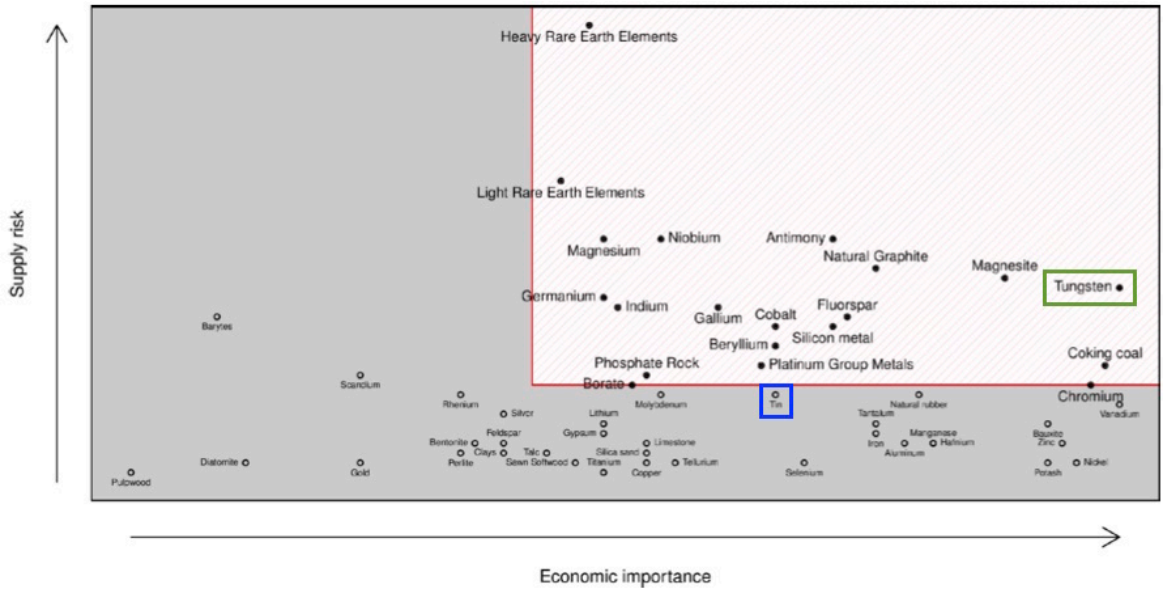

Figure 1.2 – EU critical and non-critical raw materials combined with their supply risk and economic importance, and respective thresholds; green square – W raw material; blue square – Sn raw material (adapted from DG-ENTR, 2014).

Table 1.1 – EU critical and non-critical raw materials combined with the EU supply (adapted from DG-ENTR, 2014).

Critical raw materials		Gallium Magnesite	Silicon metal Coking coal Fluorspar Germanium Indium	Chromium **Tungsten**	Antimony Beryllium Borate Cobalt Magnesium Natural graphite Niobium PGM Phosphate rock HREE LREE
EU supply	**> 20%**	**< 20%**	**< 10%**	**< 3%**	**< 1%**
Non-critical raw materials	Clays (and kaolin) Diatomite Feldspar Hafnium Limestione Perlite Sawn softwood Silica sand Tellurium	Bentonite Gypsum Potash Pulpwood Selenium Talc	Aluminium Copper Rhenium Silver Zinc	Barytes Bauxite Iron Lithium Nickel	Gold Manganese Molybdenum Natural rubber Scandium Tantalum **Tin** Titanium Vanadium

1.2. Organization of the thesis

This thesis is organized into seven main sections. The first section (**1. Introduction**) reports the setting, goals, and organization of this thesis. This section also introduces the geographical, geomorphological and historical setting of the São Pedro das Águias skarn ore deposit. The second section **2. Geological setting of skarn deposits** has the aim of presenting the geological aspects about the skarn deposits in general. Therefore, it covers their genesis and processes, classifications, and examples both in Portugal and all over the world. The geological issues about the São Pedro das Águias skarn deposit in particular are presented in **3. Materials**. In this section are discussed all the issues which are involved in the São Pedro das Águias skarn deposit formation, from the Variscan Orogeny, passing by the Iberian Massif, the Central Iberian Zone, the regional geology, to the local geology, the available database, and a multivariate analysis of correlations between elements fingerprints, lithologies and hydrothermal alteration types.

The forth section, **4. Methodology and theoretical background**, starts by presenting the state-of-

the-art, followed by an explanation of the applied methodology, and ending with a review of the used theoretical background. The case study itself is handled in **5. Case study**. This section covers the data description and processing, and the obtained results, from the univariate and bivariate analysis, passing by the results from each step of the methodology, to the summary of the resources present in the deposit. At last, the conclusions of all the present work and the further studies or works are reported in **6. Final remarks**. The bibliography and references used during this study are covered in the last section (**7. References**).

1.3. Geographical and geomorphological setting

The Tabuaço Experimental Mining License is located in the north-central part of Portugal, in a Porto wine growing area, namely in the Armamar-Penedono region. It is situated approximately 300 km to north-northeast of Lisbon (capital of Portugal), and 100 km to the east-southeast of Oporto (the second largest city of Portugal; O'Donovan *et al.*, 2012; Beare and MacDougall, 2013; Figure 1.3). The São Pedro das Águias skarn ore deposit is located in the municipality of Tabuaço (district of Viseu), more precisely in the civil parish of Távora. It is cropping out in the western bank of the Távora River, in the São Pedro das Águias farmland area (Figure 1.4). The Távora River is a tributary of the Douro River (the northern main river of Portugal). The São Pedro das Águias farmland is situated approximately 2 km to the southeast of the village of Távora, and 5 km to the same direction of the town of Tabuaço.

According to the geomorphological setting, the terrain around São Pedro das Águias ore deposit is conditioned by two existent lithologies: (1) granites; and (2) metasediments. The study area is hilly and varies from: (1) steep peaks with v-shaped valleys in the central, northeastern and eastern parts; to (2) undulating rolling hills in the southwestern areas. The schists and greywackes (metasediments) are predominant in the former zone. On the other hand, in the latter zone one can verify the existence of granites (Sousa, 1982; Ferreira and Sousa, 1994; O'Donovan *et al.*, 2012; Beare and MacDougall, 2013). The elevation of this area ranges from 225 m to 500 m above the sea level.

The drainage system of this area is constrained by the main faulting system, with direction of north-northwest–south-southeast. However, the fractures with directions of north-south and north-northeast–south-southwest also condition the rivers of this drainage system (Sousa *et al.*, 1979; Sousa, 1982; Ferreira and Sousa, 1994). The direction of the Távora River confirms this evidence. When the Távora River crosses granite terrains it goes in a straight direction according to the main fractures. When it crosses metasediment terrains it goes in a more irregular direction, but it is still conditioned by the fractures. There are occurrences of breccia-quartz veins filling some fractures. These veins are in relief owing to the differential erosion (Sousa *et al.*, 1979; Sousa, 1982; Ferreira and Sousa, 1994), such as São Pedro das Águias-Granjinha-Monte Verde Vein, which has northeast-southwest direction and makes the contact between the granites and the

metasediments.

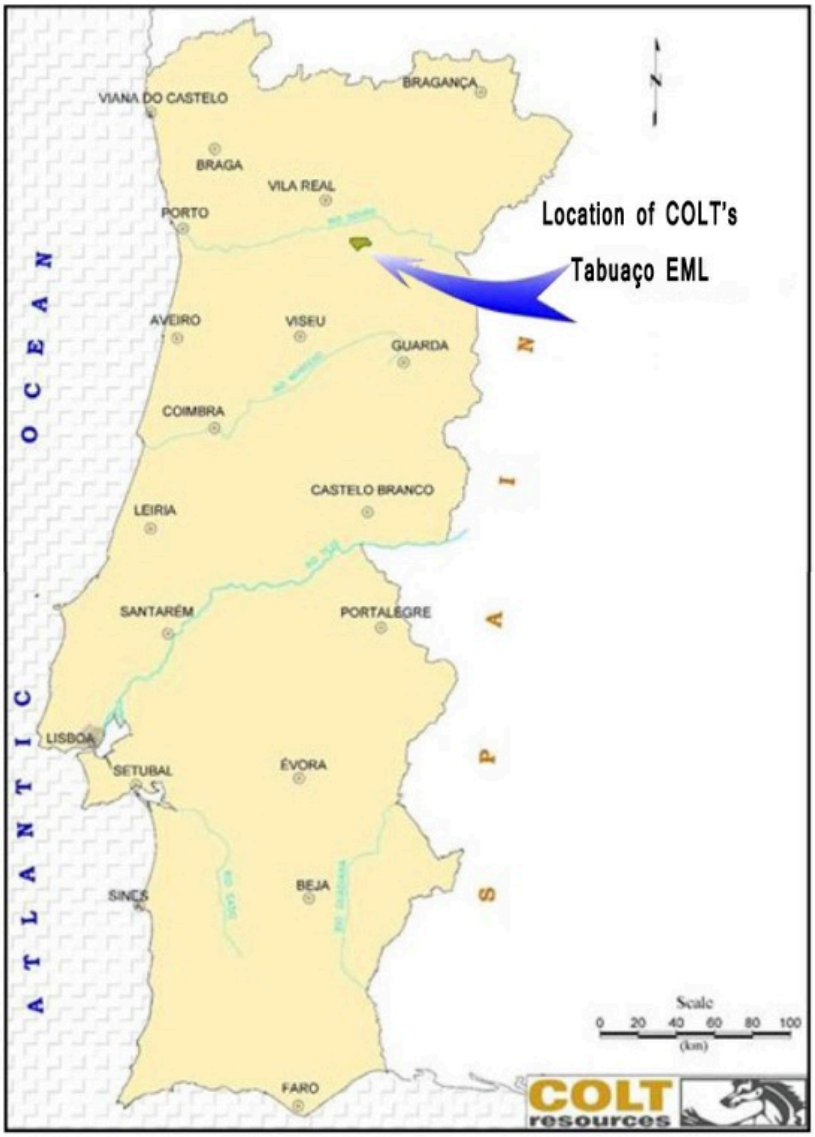

Figure 1.3 – Portugal's map showing the location of the Tabuaço Experimental Mining License in Portugal (O'Donovan, 2012; Beare and MacDougall, 2013).

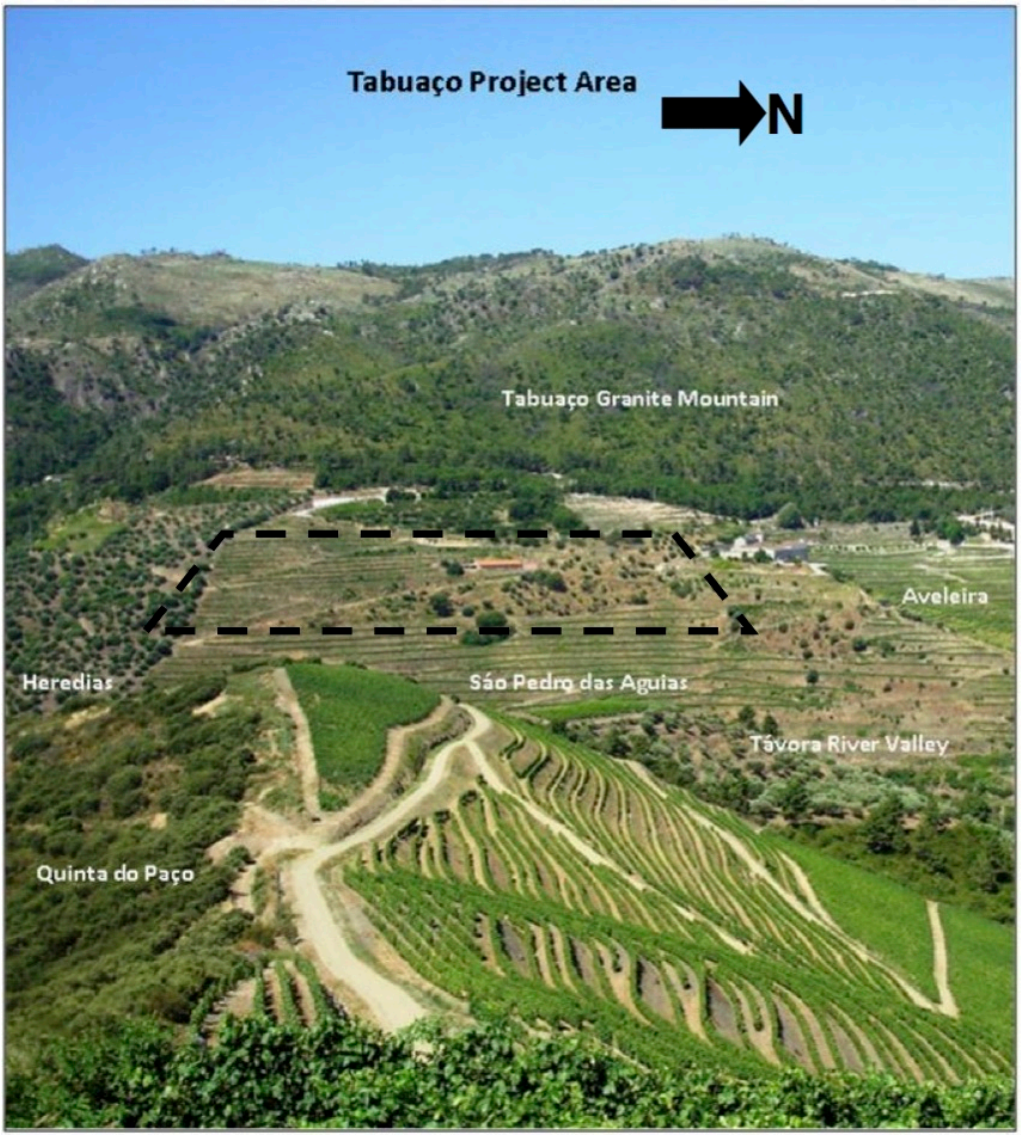

Figure 1.4 – Eastern view of the São Pedro das Águias skarn deposit area; the dashed trapezium represents the approximated location where the skarns are cropping out (O'Donovan, 2012; Beare and MacDougall, 2013).

1.4. Historical setting of the São Pedro das Águias ore deposit

Comparing with other mined occurrences in Portugal, the studied deposit is considered a recent one, discovered approximately 40 years ago. In the Tabuaço area there is no record or evidence of prior scheelite mining (Sousa *et al.*, 1979; Moura and Velho, 2012; O'Donovan *et al.*, 2012; Beare and MacDougall, 2013). This fact may be verified taking a few examples, for instance the Penedono gold deposit, and the Panasqueira tungsten deposit that were both discovered much earlier (Murton, 2007; Moura and Velho, 2012). The mining of the Penedono gold deposit was started by Romans, from 200/300 BC to 300/400 *AD*. After and much later from 1930's to 1950's, then only investigated from the 1970's to 1990's, and finally to the present. About the Panasqueira

deposit, its first exploration license was granted in 1886. The mine was founded in 1896 and only stopped the mining operations in two small periods, after the II World War and in the 1990's.

According to Sousa *et al.* (1979, *in* O'Donovan *et al.*, 2012, and Beare and MacDougall, 2013), there were some small artisan Sn mines in the opposite flank of the Távora River. However, the scheelite skarns along Távora's margins were only discovered in the 1970's by *SFM*, during geological fieldwork and mineral-light exploration (with short-wave UV lamp). Therefore, during the period from 1979 to 1984, the Armamar-Meda Licence (that includes the Tabuaço area) was included in the Alto Douro exploration concession (Sn-W, Au, *etc.*), and a joint venture between the Portuguese *SPE* and the French *SEREM* (*SPE-SEREM*) was formed in order to keep the exploration in the Tabuaço area (Moura and Velho, 2012; O'Donovan *et al.*, 2012; Beare and MacDougall, 2013).

Hence, from 1980 to 1981, the *SPE-SEREM* started the joint venture initial phase of prospection works in Tabuaço. These prospection works were focused on regional mapping, UV lamp exploration, grab sampling, channel rock sampling, and stream sediment and soil sampling programmes (O'Donovan *et al.*, 2012; Beare and MacDougall, 2013). The majority of the prospection works were in the São Pedro das Águias ore deposit. All vegetation there was removed to enable an extensive sampling of the northern and southern skarn outcrops. The northern outcrops samples gave a mean grades between 0.55 and 0.67% W and 0.086% Sn, and the southern samples gave grades within 0.10 and 0.55% W and 0.05% Sn.

The *SPE-SEREM* joint venture carried out an initial drilling prospection with six drill-holes, during the period of 1981-1982, to define the geometry, structure, and grades of the scheelite mineralized skarns in the Tabuaço area (Moura and Velho, 2012; O'Donovan *et al.*, 2012; Beare and MacDougall, 2013). Three of the drill-holes intersected the best mineralized horizons. The two easternmost drill-holes intersected an upper carbonate and a lower mineralized skarn horizon, with sub-horizontal dip, reporting grades from 0.48 to 0.93% WO_3. And the northernmost one crossed approximately 19 m of mineralization with 1.18% WO_3. Attending this drill-hole, it was thought that this part of the deposit represented its central area. However no further drilling exploration was done to verify this supposition. As a result of the upper exploration programme in the Tabuaço area, the *SPE-SEREM* joint venture has estimated a geological resource of approximately 1 Mt of scheelite mineralized skans in stratiform horizons, with an average grade of 0.87% WO_3.

Later, between 2007 and 2012, Colt acquired the Armamar-Meda exploration concession, and started a new exploration campaign. The company began with an extensive outcrop sampling work and a drilling prospection program, in which were involved more than 100 drill-holes with over 11.400 m until now (O'Donovan *et al.*, 2012; Beare and MacDougall, 2013). Although the surface rights are subordinated to the mining rights, in 2011 the company acquired 140 ha of surface rights (including vineyards, a winery, and a former Cistercian monastery) to prevent delays imposed by the landowners during the exploration and remaining activities. Finally, the Tabuaço Experimental Mining License, that covers a total area of 45.13 km^2, was granted to Colt in 2013, which

continues the deposit evaluation to the date.

2. Geological setting of skarn deposits

This section presents the geological issues about skarn deposits in general. It has the aim of discussing the general aspects of the skarn deposits genesis and processes, classifications, and examples both in Portugal and all over the world.

2.1. Skarn deposits

The word “skarn” was originally employed by old Swedish miners to refer to the very tough rocks comprised by coarse-grained calc-silicate gangue associated with the Precambrian magnetite and chalcopyrite deposits in Sweden (*ex. gr.*, Burt, 1977; Robb, 2005). However, there is evidence of mining skarn deposits since at least 4000 years ago by the ancient Chinese, Greek, and Roman empires (*ex. gr.*, Nicolescu and Mârza, 1989, *in* Meinert *et al.*, 2005). Afterward, only since the 19th century, did skarn deposits begin to be described in scientific publications (Meinert, 1992). Although there were earlier descriptions of skarn forming processes and deposits, Alfred Elis Törnebohm may be considered the first author to use the term “skarn” in a scientific publication in 1875 (Meinert *et al.*, 2005).

Nowadays, the widely used definition of “skarn” (Robb, 2005; which is also used in the present study) is the one discussed by Einaudy *et al.* (1981, *in* Kwak 1986, 1987), which defends the replacement-style rocks. Thus, a skarn is a calc-silicate rock formed by metasomatic replacement of carbonate lithologies (independent of whether they are Ca- or Mg-rich) by silicate minerals, during regional or contact metasomatic processes connected to igneous intrusions (Pirajno, 1992, 2009). Therefore, a skarn is a metasomatic rock with a complex mineralogy of granoblastic texture, composed by calc-silicate minerals, such as garnets (either andradite or grossular), epidote, vesuvianite, diopside, and wollastonite, originated from percolation of magmatic fluids in a carbonate rock (Moura and Velho, 2011).

2.1.1. Genesis and formation

According to Pirajno (1992, 2009), the generation of skarns implicates a sequence of processes related to and correlated with the late magmatic and hydrothermal events associated with a magmatic intrusion in sedimentary rocks. Therefore, as explained above, it results from the replacement of carbonate lithologies by silicate minerals. This alteration type is called silication, which is a process connected with the metamorphic and metasomatic contact with those carbonate rocks, promoted by the emplacement and cooling of some intrusion.

Consequently, skarn deposits are originated in three sequential stages (Figures 2.1 and 2.2; Einaudi *et al.*, 1981, *in* Robb, 2005; Meinert, 1992; Pirajno, 1992, 2009): (1) an isochemical prograde thermal metamorphic stage; (2) a metasomatic stage; and (3) a retrograde hydrothermal

alteration stage. According to Pirajno (1992, 2009), these stages match with the early potassic and later hydrolytic alterations on the porphyry stock or intrusion; skarns develop at temperatures varying from 200 to 700°C, and pressures ranging from 0.3 to 3 kbar; and the salinities of metasomatic fluids vary between 10 and about 45 wt%.

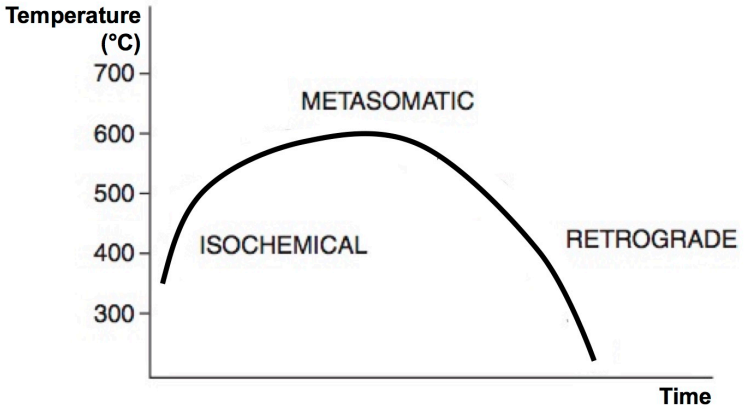

Figure 2.1 – Formation stages of skarns in function of temperature and time (adapted from Pirajno, 2009).

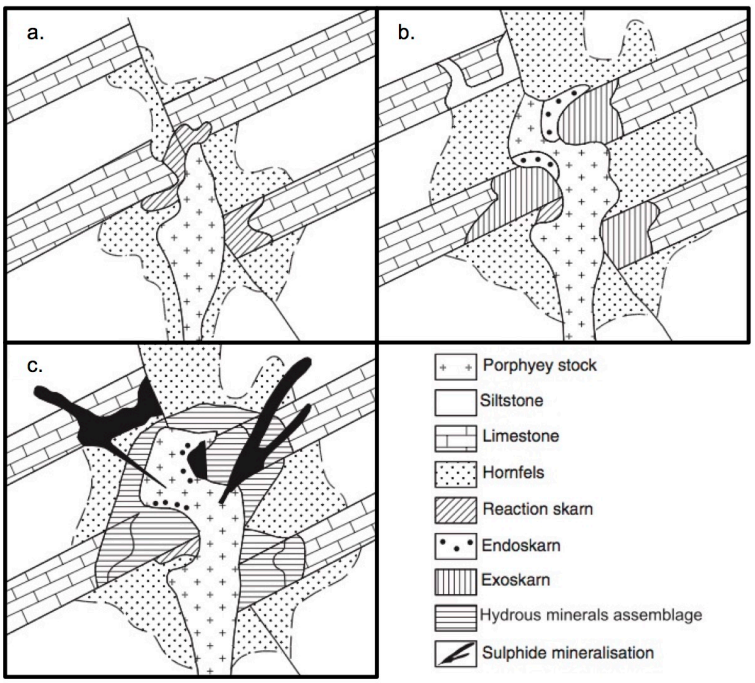

Figure 2.2 – Schematic formation stages of skarns: (a) isochemical prograde thermal metamorphism; (b) metasomatism; (c) retrograde hydrothermal alteration (adapted from Pirajno, 2009).

The isochemical prograde thermal metamorphic stage (Figures 2.1 and 2.2 a) is induced by a contact metamorphism mostly caused by thermal effect, originating mainly hornfels (Robb, 2005).

In spite of the thermal contact during this stage, there is also fluid circulation of mostly H_2O and CO_2 as a result of the prograde metamorphic reactions. The present stage has no associated mineralizations, however there are dehydration processes near the borders of the intrusion that might be important to increase the porosity of the source rocks and to ease up the fluid flux of later mineralization phases.

Continuing by the metasomatic stage (Figures 2.1 and 2.2 b), at deeper crustal levels the fluid flux is probably concentrated by structural or bedding parallel conducts, whilst at upper levels it is more pervasively distributed. Although the alteration is more pervasive and coarse-grained at this stage, comparing with the uppermost stage, the metasomatic mineral assemblages are similar. Ca, Mg and CO_2 (which are into the carbonate sediments) are replaced by Si, Al and Fe, and are inserted into the metasomatic system. During this stage sulfide mineralizations do not occur, but magnetite and scheelite precipitate in the final phases (Robb, 2005).

Finally, the retrograde hydrothermal alteration stage (Figures 2.1 and 2.2 c) comprises the progressively cooling and decline of the high temperature magmatic fluid system, because the fluids become gradually dominated by shallow meteoric waters (Burt, 1977). Thus a sequence of retrograde reactions and the precipitation of sulfide-related mineralization occur (Einaudi *et al.*, 1981, *in* Robb, 2005). The paragenetically late precipitation of most skarn-related ores indicates that the precipitation of the metals is linked to the declining temperature of the ore fluids (and a consequent drop in solubilities), the fluid mixing, or the ore fluid neutralization by the reaction with the carbonate rocks (Robb, 2005).

2.1.2. Classifications

There are several classifications for skarn deposits. Burt (1977) referred that the skarn deposits have been classified by their scale, structure, replaced rock and mined metals. Meinert (1992) noted that they may be classified according to descriptive and genetic characteristics, such as the prevailing economic metals, the protolith composition, the temperature of formation, and the mechanism of fluid movements. In spite of there being so many classifications followed by different authors, they refer roughly the same types and definitions. The more adopted classification is based on the prevailing economic metals, although not all skarns have economic mineralizations (Meinert *et al.*, 2005). Hence, the skarns that include ore mineralization, characteristically metalliferous, are named skarn deposits.

Adopting Burt's above referred classifications (1977), when skarns are classified by scale, there are two types: (1) the reaction skarns, diffusional skarns, bimetasomatic skarns, or metamorphic skarns; and (2) the replacement skarns, infiltrational skarns, ore skarns, or metasomatic skarns (Kwak, 1987). The first can be originated mostly by isochemical metamorphism of thinly interbedded shale and carbonate layers (Meinert, 1992; Meinert *et al.*, 2005; Pirajno, 2009), being of smaller scale (ranging from mm to m; Burt, 1977; Kwak, 1987). Whilst the latter contain

mineralization, formed by infiltration of fluids, which are from igneous intrusions (Pirajno, 2009), and post-date the metamorphic skarns, *i.e.*, they result by metasomatic processes interacting with the metamorphic skarns, being of larger scale (varying from cm to hundred m, or more; Burt, 1977; Kwak, 1987).

Continuing with the same classification, the replacement skarns may be classified according to their structural relations with an intrusion (Burt, 1972, *in* Burt, 1977) in: (1) normal or skarn around intrusive, if carbonate rocks are replaced by being adjacent to a small intrusive body; (2) inverse or intrusive around skarn, if roof pendants or xenoliths are replaced by a large intrusive batholith; and (3) no intrusive or skarn along a vein, if skarns take place along veins, far from an exposed intrusion.

Still following Burt´s referred classification (1977), skarns can also be classified according to the replaced lithology, that is, the initial protolith, as: (1) exoskarn; or (2) endoskarn. An exoskarn occurs when the protolith is a carbonate rock, *i.e.*, the metasomatic assemblage is external to the intrusion. Whereas, an endoskarn takes place if the protolith is an igneous or other aluminous rock, that is, the metasomatic assemblage is internal to the intrusion (Meinert, 1992; Pirajno, 1992, 2009; Meinert *et al.*, 2005; Robb, 2005).

In turn, the exoskarns can be divided into: (1) calcic skarns, when Ca-rich and if the protolith is a limestone; or (2) magnesian skarn, when Mg-rich and if the replaced rock has a dolomitic composition. As mineralogical content, the calcic skarns may have garnets (from andradite-grossularite series), clinopiroxenes (from diopside-hedenbergite series), wollastonite, scapolite, epidote, and magnetite. While magnesian skarns may have in silica-poor environments, diopside, forstrite, serpentinite, magnetite and talc, and in silica-rich environments, talc and tremolite-actinolite (Burt, 1977; Meinert, 1992; Pirajno, 1992, 2009; Meinert *et al.*, 2005; Robb, 2005). Pirajno (1992, 2009) also refers the existence of silica-pyrite skarns associated with some porphyry deposits, and Meintert *et al.* (2005) also makes reference to mangan skarns.

According to the prevailing economic metals/ores classification, Burt (1977) referred the subdivision of the skarn deposits in four cathegories: (1) Fe (iron skarns), when it contains magnetite or, rarely, specularite; (2) Cu (cupriferous skarns), when it has chalcopyrite, bornite and other sulfides; (3) Zn (zinciferous skarn), when it contains sphalerite; and (4) W (tungsten skarn), when have scheelite. Later, other authors have added two more types to this classification, which have stayed: (1) W; (2) Mo-Sn; (3) Cu; (4) Fe; (5) Zn; and (6) Au (Pirajno, 1992; Robb, 2005).

Pirajno (1992), for example, subdivided these types whether they are related with porphyry skarns or not: (1) Cu and Fe are porphyry-related skarns; while (2) Fe, W, Sn and Mo are non-porphyry-related skarns. So, despite there being exceptions, Robb (2005) associated the last types according to the composition of the igneous intrusions (Figure 2.3): (1) Fe and Au skarn deposits are usually linked with intermediate to mafic intrusions; (2) Cu, Zn and W deposits are normally associated with calc-alkaline, magnetite-bearing, I-type granitic intrusions; and (3) Mo-Sn are generally connected with more differentiated granites that may be of S-type and ilmenite-bearing.

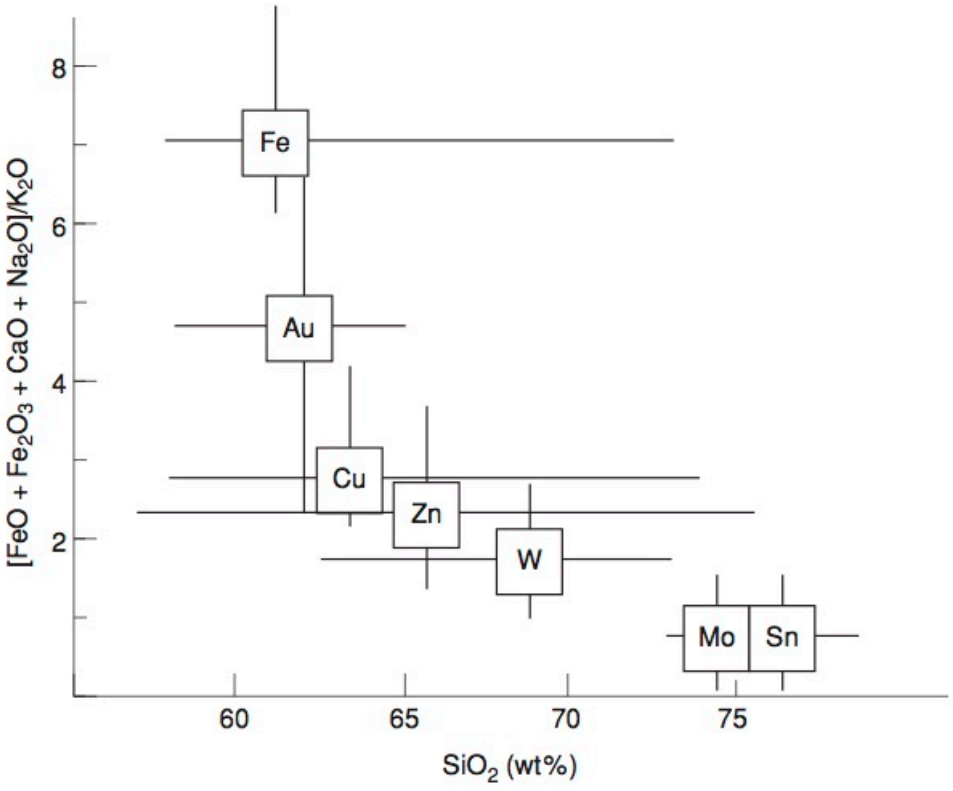

Figure 2.3 – Skarn deposits types according with the prevailing economic metals (adapted from Robb, 2005).

According to the above classifications, it is possible to refer that the case study skarn deposit is a replacement, normal, exo-calcic, and W skarn deposit (O'Donovan, 2012; Beare and MacDougal, 2013). Therefore, it is only missing to define what is a W skarn deposit. A W skarn deposit is referred to a skarn that holds anomalous W grades with Sn low-grade, or even no Sn. This kind of deposit is usually stratiform (extending for hundreds of m with thicknesses unusually exceeding 12 m), and derives from interlayered carbonates and pelites (Kwak, 1987). It is linked to coarse-grained equigranular batholiths with pegmatite and aplite dykes, and surrounded by large high-temperature metamorphic aureoles (Meinert, 1992). These batholiths are characteristically connected with calc-alkaline intrusions from a relatively deep environment (Robb, 2005; Pirajno, 2009) of generally I-type (Kwak, 1987), although there are exceptions of S-type intrusions, such as the batholith next to São Pedro das Águias skarn deposit (O'Donovan, 2012; Beare and MacDougal, 2013; Cerejo, 2013; Cerejo *et al.*, 2014).

2.1.3. Skarn deposits all over the world

Skarn deposits are broadly distributed all over the world (Kwak, 1987; Meinert, 1992; Meinert *et al.*, 2005), and are dated from practically all ages, since the Precambrian to the Late Tertiary. The

relatively younger deposits are the economically the most important (Burt, 1977). They are also one of the most plentiful ore types in the Earth's crust (Meinert *et al.*, 2005), and most of them were mined for a range of elements (Meinert, 1992) occurring in the most tectonic settings, such as oceanic steep subduction, continental drifting, etc. (Figure 2.4; Einaudi *et al.*, 1981, *in* Pirajno, 2009; Meinert *et al.*, 2005).

Figure 2.4 – Map showing the distribution of the large W and Sn skarn deposits and of the crustal elements; closed squares – W skarn deposits; crosses – Sn skarn deposits; dashed lines areas – Phanerozoic fold belts; dense dotted areas – Precambrian shields; lightly dotted areas – ancient platforms (Kwak, 1987).

Summing up, for instance Meinert (1992) and Pirajno (2009) selected a set of examples of the major skarn deposits divided by the prevailing economic metals. As few examples of Cu skarn deposits, there are Mines Gaspé (Quebec) and Bingham (Utah), both associated with porphyry Cu deposits. Continuing with the W-type, to exemplify the Pine Creek (California) and the King Islands (Tasmania). Passing by the Sn-type, Moina (Tasmania) and Lost River (Alaska), which are good examples. About Au-type, there are Crown Jewel (Washington) and Navachab (Namibia) for instance. For the Zn-type there are the Nakatatsu Mine (Japan) and the Naica (Mexico). Good examples of the Mo-type are Yangchiaachangtze (China) and Azegour (Morocco). Finally, for Fe-Skarns, there are Teya Deposit (Russia) and Larap (Philippines).

According to the case study skarn deposit type, Kwak (1987) presented the large W and Sn skarn deposits distributed all over the world and how they are related with the crustal elements (the

Phanerozoic fold belts, the Precambrian shields, and the ancient platforms; Figure 2.4). Apparently, these types of skarn deposits take place mostly into the Phanerozoic fold belts areas (more than 90% of the cases), both in marginal to major plates (Cordilleran area, North America) and within plates (central Asia).

2.1.4. Skarn deposits in Portugal

The skarn deposits in Portugal are mainly distributed in the central-northern part of the country. Most of the Portuguese skarns are located in the Central Iberian Zone, occurring in practically the whole the Dúrico-Beirão Supergroup lithostratigraphic sequences (Sousa, 1981). As the case study deposit, according to Martins (2012) the skarn deposits in the Dúrico-Beirão Supergroup contain scheelite, and are inserted in the Douro Scheelite Belt (Figure 2.5). Despite this fact, the same author and Moura and Velho (2012) also refer to the existence of small skarn deposits in Vila Nova de Cerveira and Covas (district of Viana do Castelo) in the Silurian sequences, and Pinto (1984) also refers that there are skarns in Ossa-Morena Zone, namely in Alvito.

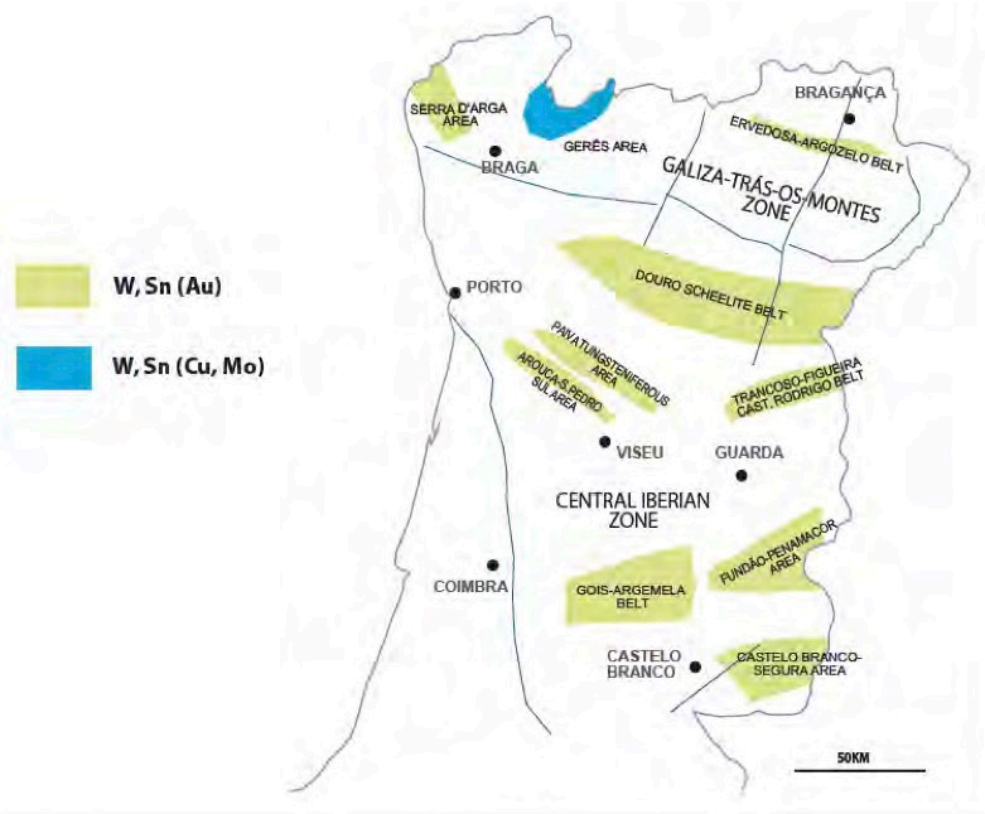

Figure 2.5 – Map showing the W and Sn potential areas in Portugal with mineralizations (Martins, 2012).

According to the skarn deposits in the Dúrico-Beirão Supergroup lithostratigraphic sequences, Moura and Velho (2012) give some more important examples. Those examples are the case study

itself in Tabuaço (as referred before), the Riba de Alva (between Barca de Alva and Freixo-de-Espada-à-Cinta), the Santo Antão in Lamego, and the Machorrinho (Pinhel).

3. Materials

The present section intends to demonstrate the geological issues about the São Pedro das Águias skarn deposit in particular. It has the objective of reporting the particular topics that implicate the São Pedro das Águias skarn deposit formation, from the Variscan Orogeny, passing by the Iberian Massif, the Central Iberian Zone, the regional geology, to the local geology, the available database, and a multivariate analysis of correlations between elements fingerprints, lithologies and hydrothermal alteration types.

3.1. Geological setting of the São Pedro das Águias skarn deposit

The São Pedro das Águias skarn deposit is situated in the central sector of the Central Iberian Zone, a tectono-stratigraphic unit of the Iberian Massif of the Iberian Variscan Belt, which is in turn included in the European Variscan Fold Belt. These issues will be presented later in the present subsection. In order to introduce the geological setting of the São Pedro das Águias skarn deposit, it is necessary to go back to the period between the Late Proterozoic and the Early Paleozoic. In this time span two oceans opened in the Earth, Iapetus and Tornquist, which detached three continental masses (Catalán *et al.*, 2007): (1) Laurentia; (2) Baltica; and (3) Avalonia.

Possibly, Avalonia originated close to Gondwana, due to its fauna (Cocks and Fortey, 1988, *in* Catalán *et al.*, 2007). However in the Late Cambrian–Early Ordovician this microcontinent or terrane drifted forming the Rheic Ocean. Finally, during the Devonian, the closure of this ocean formed the Variscan Belt in central and western Europe and northern Africa, and the Alleghanian Orogen in North America (*ex. gr.*, Hatcher, 1982, *in* Catalán *et al.*, 2007), in which originated the Pangea Supercontinent (Catalán *et al.*, 2007).

The studied mineralizations are hosted in a Lower Cambrian stratigraphic sequence (Bateiras Formation of the Douro Group of the Dúrico-Beirão Supergroup), which ultimately records the break-up processes at the North-Gondwana margin (Catalán *et al.*, 2007).

3.1.1. Variscan Orogeny

The Variscan Orogeny began with the initial episodes of the oceanic closure that drove to the formation of Pangea. This oceanic closure, according to Catalán *et al.* (2007), took place by the actuation of three sets of orogenic diachronic episodes: (1) the initial one occurred during the Late Cambrian and the Middle Ordovician, and it was an arc-continent collision in both sides of the Iapetus Ocean (*ex. gr.*, Kelling *et al.*, 1985, *in* Catalán *et al.*, 2007), which originated the Scandinavian and the British Caledonides belts (the Finnmarkian and the Grampian belts,

respectively; Figure 3.1), and The Appalachians (the Taconic and the Penobscottian Belts; Figure 3.1); (2) the second event happened between the Early Silurian and the Late Devonian, and gave rise to Laurussia with the closure of Iapetus, and the collision of Laurentia with Baltica and Avalonia (forming an arc in the Avalonia side; *ex. gr.*, Soper, 1988, *in* Catalán *et al.*, 2007); and, finally, (3) the last one took place during the Carboniferous and the Early Permian, originating an intense deformation in Europe and Africa, and The Appalachians (the Variscan and the Alleghanian belts, respectively; Figure 3.1), resulting in the formation of Pangea with the closure of the Rheic and Theic Oceans, and the collision of Gondwana with Laurussia (Lefort, 1989, *in* Catalán *et al.*, 2007).

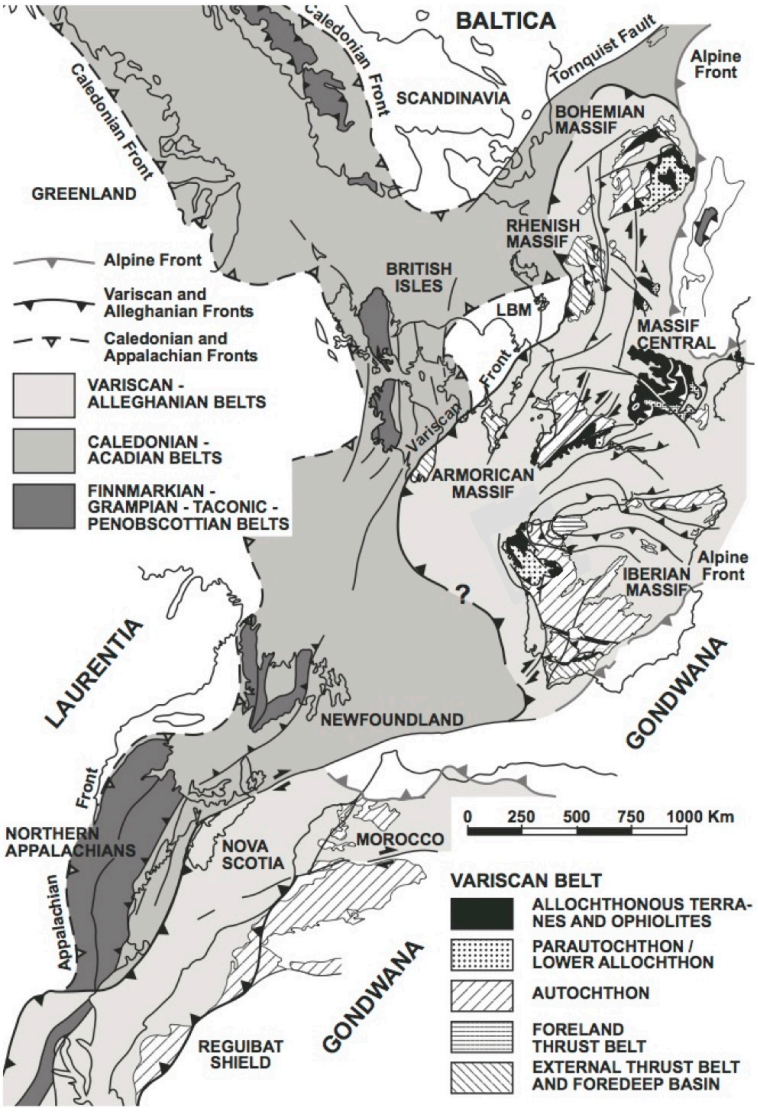

Figure 3.1 – Sketch showing the Iberia position in relation to the Appalachian, Caledonian and Variscan belts at the end of Variscan convergence; LBM – London-Brabant Massif (adapted from Catalán *et al.*, 2002, *in* Marínez Catalán *et al.*, 2007).

As consequence, the formation of the Pangea Supercontinent originated the Variscan Belt in the Europe region (Figure 3.2), which was formed during the complex and polycyclic collision between Laurentia and Baltica with Gondwana (Aguado *et al.*, 2005). This belt is composed by several massifs (such as the westernmost Bohemian Massif, and the easternmost Iberian Massif in Europe), and is a linear sinuous belt (Catalán *et al.*, 2007). It is also comprised of two oroclines or oroclinal arcs, from the northeast to the southwest of Europe (Figure 3.2): (1) the Bohemian Massif and the Massif Central (*ex. gr.*, Franke and Zelazniewicz, 2002, *in* Catalán, 2011); and (2) the Iberian-Armorican arc (*ex. gr.*, Ribeiro *et al.*, 1975, *in* Catalán, 2011). According to Dias *et al.* (2014), the formation of the Iberian-Armorican Arc is still controversial. Some authors defend that it was generated by self-subduction (*ex. gr.*, Johnston *et al.*, 2013, *in* Dias *et al.*, 2014), whilst others support that it was formed by indentation of a promontory of Gondwana (*ex. gr.*, Dias and Ribeiro, 1995, *in* Dias *et al.*, 2014).

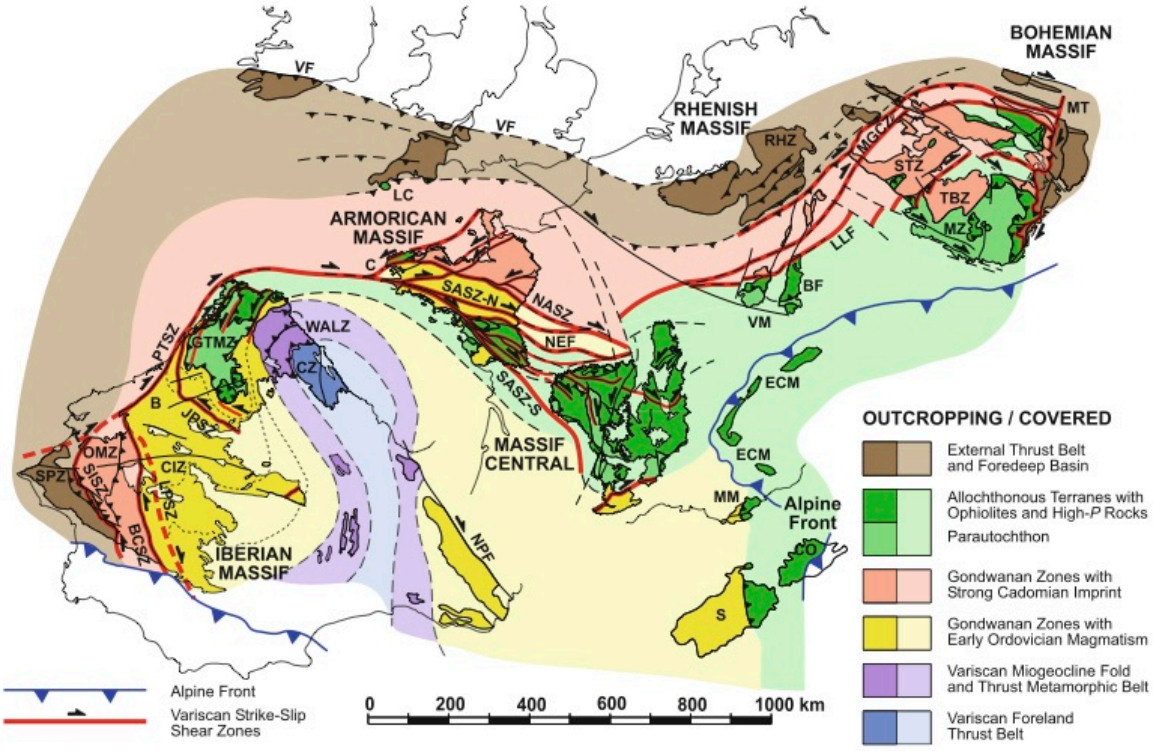

Figure 3.2 – Sketch showing the Variscan Belt in Europe; B – Buçaco; BCSZ – Badajoz-Córdova Shear Zone; BF – Black Forest; C – Crozon; LC – Lizard Complex; LLF – Layale-Lubine Fault; LPSZ – Los Pedroches Shear Zone; MGCZ – Mid German Crystalline Zone; MM – Maures Massif; MT – Moldanubian Thrust; NASZ – North Armorican Shear Zone; NEF – Nort-sur-Erdre Fault; NPF – North Pyrenean Fault; PTSZ – Porto-Tomar Shear Zone; RHZ – Rheno-Hercynian Zone; S – Sardinia; SASZ – South Armorican Shear Zone (-N and -S – Northern and Southern branches, respectivelly); SISZ – Southern Iberian Shear Zone; VF – Variscan Front; VM – Vosges Massif (Catalán *et al.*, 2007, *in* Catalán, 2011).

According to Catalán (2007), the Iberia-Armorican Arc is not the last orocline of the Variscan Belt

to the southwest. In the central part of the IM exists another arc with comparable magnitude, but opposite (clockwise) curvature, delineated by the curvature of D_1 Variscan folds (Figure 3.2 and Figure 3.3; Catalán, 2011). Firstly, it was suggested by Staub (1926, *in* Catalán, 2011), and named Castilian Bend. However, Lotze (1945b, *in* Catalán, 2011) did not regard the existence of another arc on his division of the Iberian Meseta Variscides. Only later, Aerden (2004, *in* Catalán, 2011) discerned its existence in the Central Iberian Zone of Julivert *et al.* (1972) by the presence of the Varican folds and magnetic anomalies.

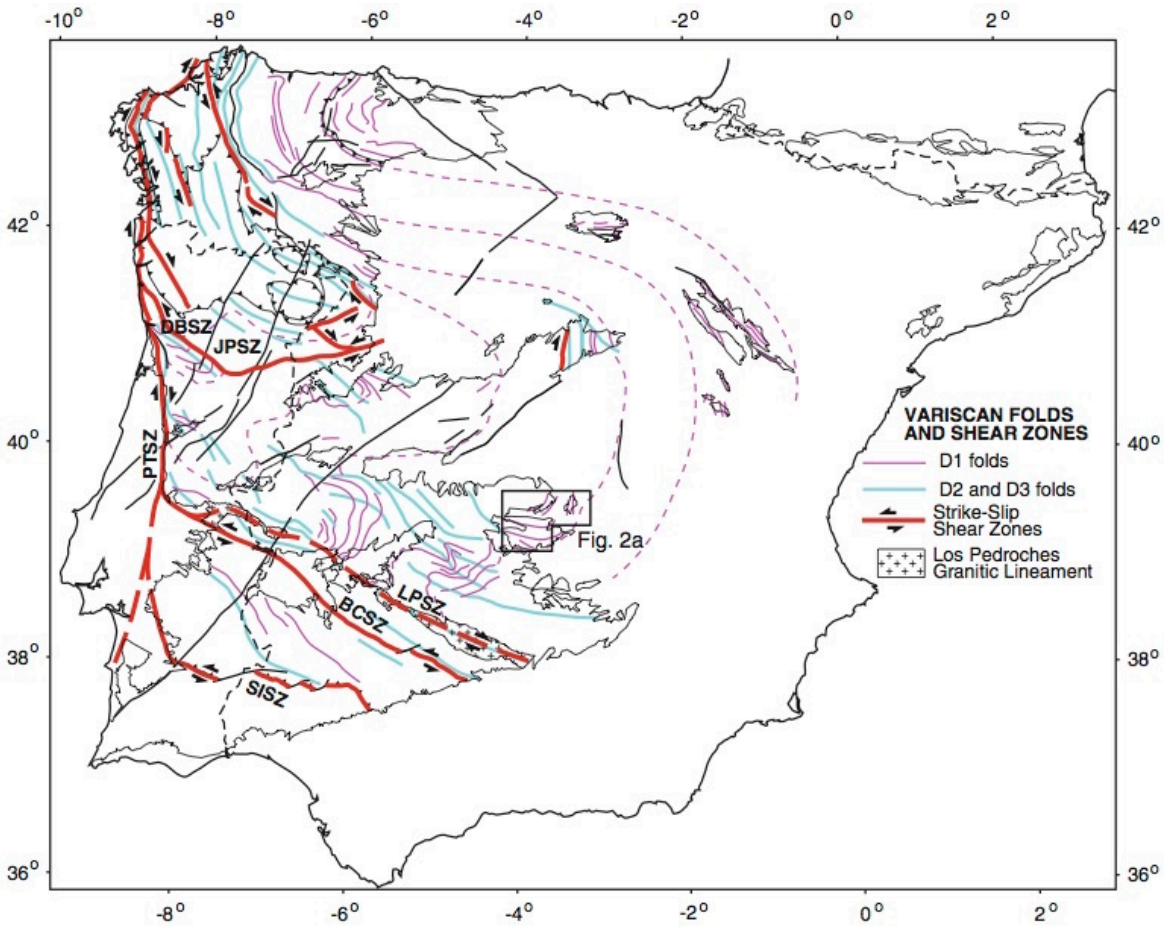

Figure 3.3 – Sketch showing the axial traces of the Variscan folds and the main discrete strike-slip shear zones demonstrating the curvature of the Central Iberian Arc; BCSZ – Badajoz-Córdova Shear Zone; DBSZ – Douro-Beira Shear Zone; JPSZ – Juzbado-Penalva Shear Zone; LPSZ – Los Pedroches Shear Zone; PTSZ – Porto-Tomar Shear Zone; SISZ – Southern Iberian Shear Zone (Catalán, 2011).

Later, Catalán (2010, *in* Catalán, 2011), owing to its development in Central Iberian Zone, named the above arc as Central Iberian Arc. Afterwards, the same author (Catalán, 2011) established that its hinge zone is located in the covered region between Guadalajara and Albacete, to the southeast of Madrid, and the Los Pedroches Shear Zone might represent its southern limit (Figures 3.2 and 3.3). Attending to Ribeiro (2013b), the Variscan Belt in the innermost part of the

Iberian Massif, namely in the Central Iberian Zone (Central Iberian Arc), is orientated northwest-southeast (Figure 3.3).

3.1.2. Iberian Massif

The Iberian Massif or Hesperian Massif form Iberia (Ribeiro, 2013a) represents the westernmost part of the Variscan Belt in Europe (Figure 3.2; Dallmeyer and García, 1990; Ribeiro, 2013b). This massif is delimited to the north by the Cantabrian Sea, and to the west and southwest by the Atlantic Ocean. Post-Variscan and Post-Alpine continental deposits are overlain its eastern border, and the southeastern boundary comprises the Guadalquivir Fault (Dallmeyer and García, 1990). According to Ribeiro (2013a), the Iberian Massif is divided into two blocks, separated by the Central Range and covered by Cenozoic basins: (1) the Northern Meseta; and (2) the Southern Meseta. The former encompasses the Douro Basin (with about 800 m of elevation above the sea level), while the second embraces the Superior Tagus (east) and the Lower Tagus-Sado (west) Basins (ranging its elevation between 900 and 200 m above the sea level). Beyond the above basins, two important Meso-Cenozoic sedimentary basins formed in the western and southern limits of the Iberian Massif, the Lusitanian or Western Basin, and the Algarve or Southern Basin, respectively (Ribeiro, 2013b).

Lotze (1945, *in* Dallmeyer and García, 1990) was the first subdividing the Iberian Massif into six different tectono-stratigraphic zones (Figure 3.4): (1) the Cantabrian Zone; (2) the West Asturian-Leonese Zone; (3) the Galaico-Castilhana Zone; (4) the Luso Oriental-Alcudian Zone; (5) the Ossa-Morena Zone; and (6) the South Portuguese Zone. Julivert *et al.* (1972, *in* Dallmeyer and García, 1990) proposed the Tectonic Map of Iberia and modified Lotze's subdivision using a structural criterion. Therefore, they combined the Galician-Castilian and the Lusitanian-Alcudian Zones and, consequently, created the Central Iberian Zone. They also recognized the existence of allochthonous materials in the Galaico-Castilhana Zone, and suggested the Galiza Média–Trás-os-Montes Subzone in that area (Dias and Ribeiro, 2013). Finally, Farias *et al.* (1987, *in* Dias and Ribeiro, 2013) formalized the Galiza–Trás-os-Montes Zone (Figure 3.5).

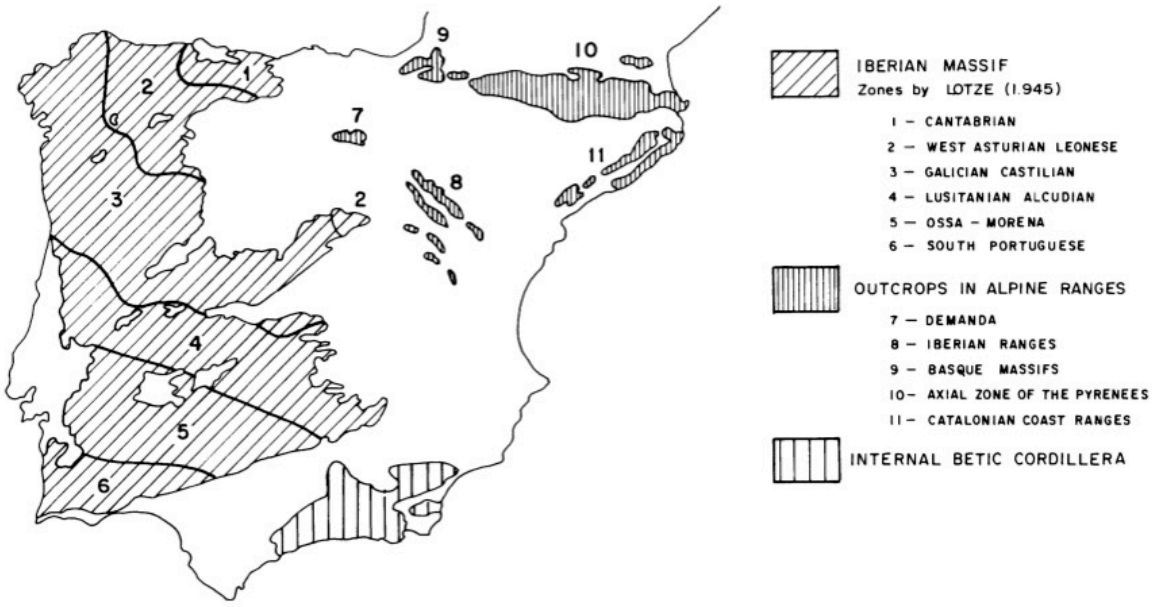

Figure 3.4 – Sketch showing the Lotze's subdivision of the Iberian Massif (Balda *et al.*, 1990).

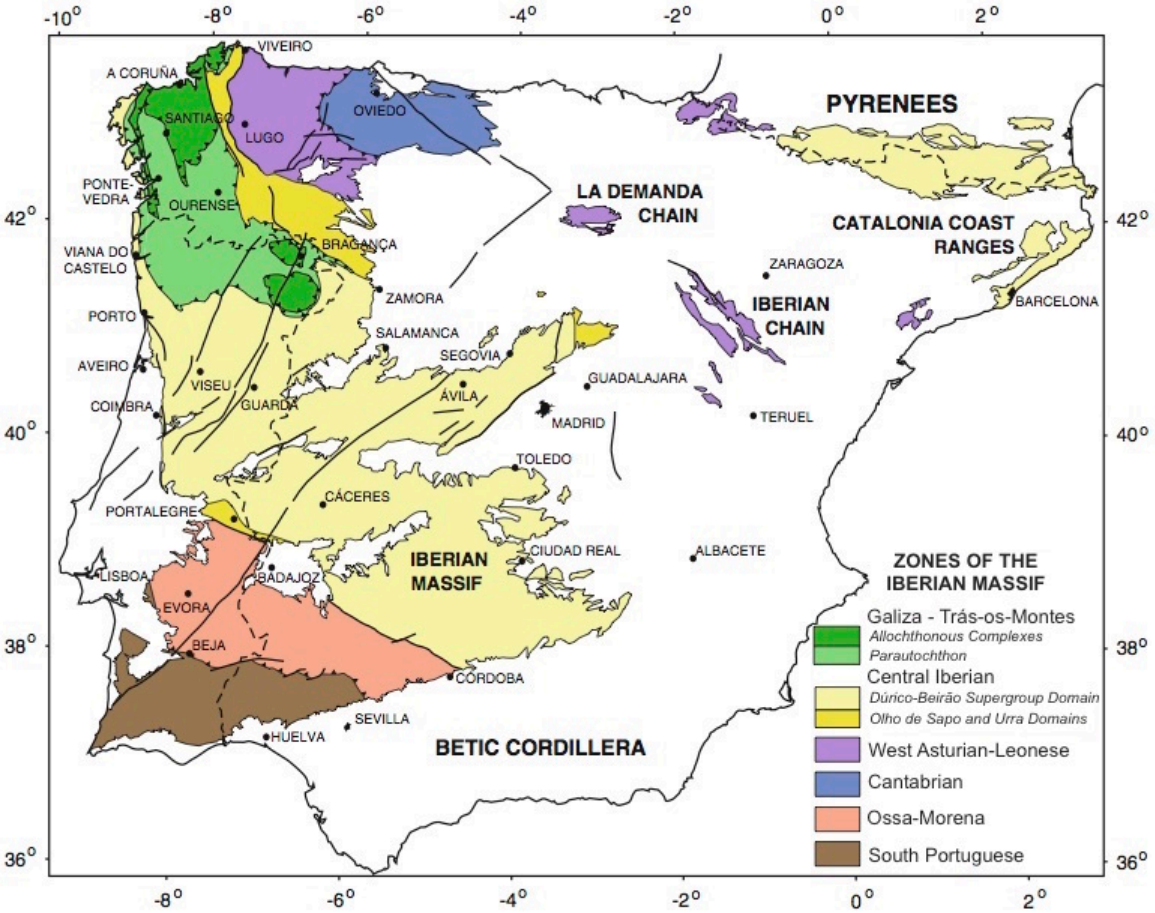

Figure 3.5 – Sketch showing the division of the Iberian Massif (adapted from Catalán, 2011).

3.1.3. Central Iberian Zone

The Central Iberian Zone is situated in the innermost part of the Iberian Massif (Villaseca *et al.*, 2014), between the West Asturian-Leonese Zone and the Ossa-Morena Zone (Vilas and San José, 1990), and is a major tectono-stratigraphic zone of Iberia (Julivert *et al.*, 1974, *in* Pereira *et al.* 2012; Figure 3.5). From the tectonic point of view, the Central Iberian Zone forms the axial domain of the Variscan Belt in Iberia (Ribeiro, 1990; Ribeiro, 2013b). Julivert *et al.* (1972, in Balda *et al.*, 1990) placed its northern and southern boundaries in the Olho-de-Sapo Anticlinorium and Los Pedroches Batholith, respectively (limits between the Central Iberian Zone and West Asturian-Leonese Zone, and Central Iberian Zone and Ossa-Morena Zone, respectively). However, later Catalán (1985, *in* Balda *et al.*, 1990) considered that the northern limit is the Vivero Fault and Olho-de-Sapo Anticlinorium is included in the Central Iberian Zone. Balda *et al.* (1990) proposed that, from both the structural and the stratigraphic standpoint, the southern border should be placed in the Badajoz-Córdova Shear Zone. The Porto-Tomar Shear Zone materializes the western limit of the Central Iberian Zone (Ribeiro *et al.*, 2005, *in* Catalán, 2011).

Lithostratigraphically, the Central Iberian Zone is characterized by a clear predominance of Precambrian to Cambrian metasediments, forming a thick and relatively monotonous sequence of phyllites and greywackes (*ex. gr.*, Villaseca *et al.*, 2014). Catalán *et al.* (2004, *in* Dias and Ribeiro, 2013) subdivided the Central Iberian Zone in three stratigraphic domains: (1) the Dúrico-Beirão Supergroup Domain; (2) the Olho-de-Sapo Domain; and (3) the Los Pedroches Batholith Domain. Afterwards, Catalán (2011) established two domains with the definition of the Central Iberian Arc based on the D_1 Variscan folds: (1) the Dúrico-Beirão Supergroup Domain; and (2) the Olho-de-Sapo and Urra Domains.

The Dúrico-Beirão Supergroup Domain includes the stratigraphic sequences between the Ediacaran and the Cambrian. These sequences comprise a succession of classic turbidites, and locally, continental, fluvial and/or fluvio-marine deposits (Sousa, 1982; José *et al.*, 1999; Silva, 2005). The Dúrico-Beirão Supergroup was named first by Delgado (1908, *in* Ferreira da Silva, 2005) as “Beiras Schists”. Only in 1950, Carrington da Costa (1950, *in* Meireles *et al.*, 2013) gave it the famous designation of Schist-Greywacke Complex. Later, Teixeira (1981, *in* Silva, 2005) named the Ediacaran-Cambrian sequences as Hispanian, and finally, Silva *et al.* (1987, *in* Silva, 2005), from the stratigraphical and paleogeographical point of view, referred to them as Dúrico-Beirão Supergroup.

As referred above, the first who attempt to devide the Central Iberian Zone was Lotze (1945, *in* Dallmeyer and García, 1990), which created the Galaico-Castilhana Zone to the north and the Luso Oriental-Alcudian Zone to the south (Figures 3.4 and 3.6). Later, Sousa (1983) subdivided the Dúrico-Beirão Supergroup into two groups of formations, as Lotze (1945, *in* Dallmeyer and García, 1990) initially did (Figure 3.6): (1) the Beiras Group to the south (mostly Ediacaran); and (2) the Douro Group to the north (mainly Cambrian). The former comprises a thick and monotonous succession of thin phyllites and greywackes intercalating with conglomerates (Sousa,

1984); while the latter includes a sequence from the base to the top of black schists, and intercalations of calc-silicate rocks and crystalline limestones with phyllites (Sousa *et al.*, 1979).

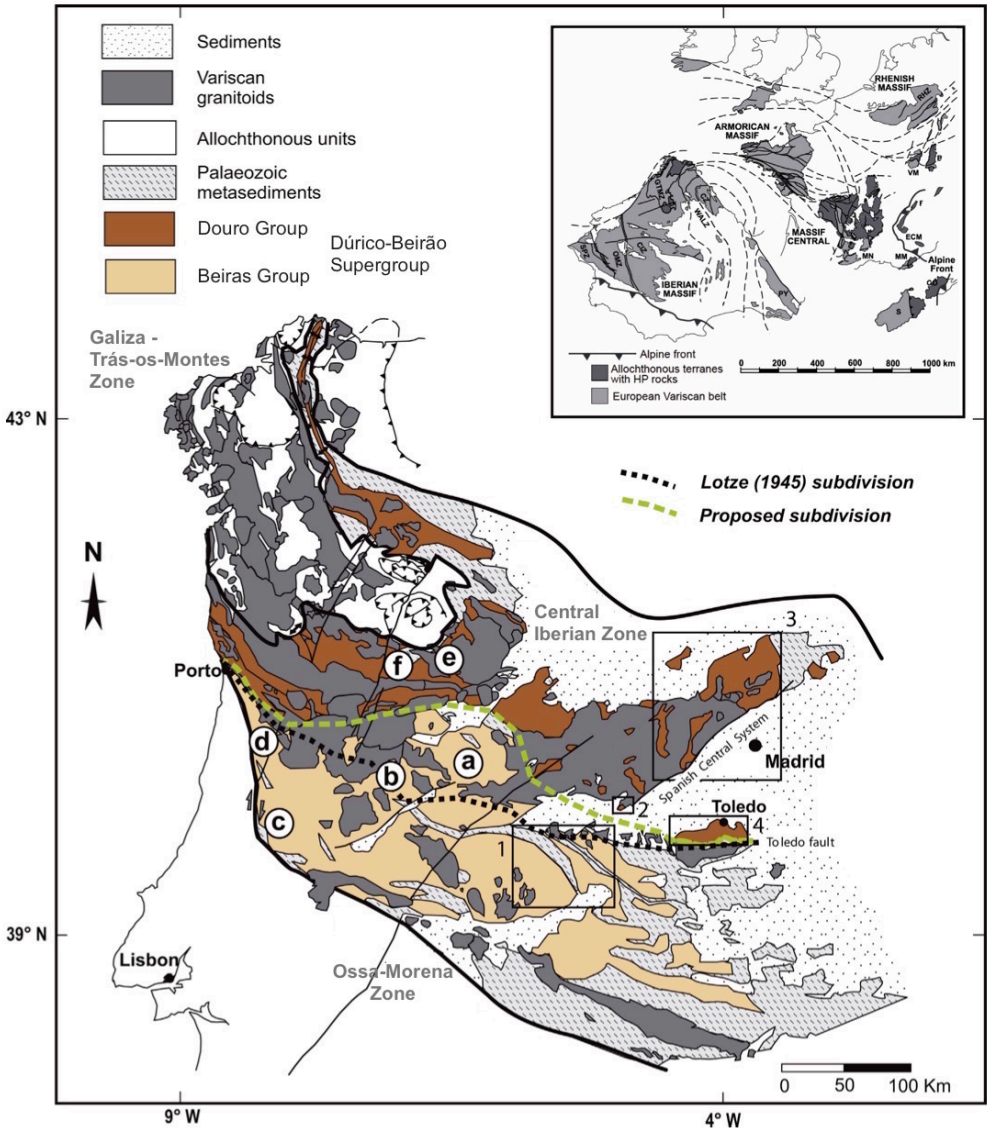

Figure 3.6 – Sketch showing the boundaries proposed by Lotze (1945) and Villaseca *et al.* (2014) for the lithostratigraphic domains of Central Iberian Zone (Dúrico-Beirão Supergroup and Olho-de-Sapo Domains); 1 – Schist-Greywacke Complex; 2 – Talavera area; 3 – Guadamarra area; 4 – Anatectic Complex of Toledo; a – Las Hurdes-Serra de Gata; b – Sabugal; c – Penacova area; d – Albergaria region; e – Tormes Dome; f – Carraceda de Ansiaes area (adapted from Villaseca *et al.*, 2014).

Oliveira *et al.* (1992, *in* Dias *et al.*, 2013) suggested a limit line that passes by S. João da Madeira, Viseu and the Malcata Range to separate both the Beiras Group and the Douro Group. This boundary marks the disappearance of the carbonate facies from the north (Douro Group) to the south (Beiras Group). However, Villaseca *et al.* (2014) proposed that both groups could have been

deposited in separated plate tectonic environments/basins, and suggested a new boundary between the Douro Group and the Beiras Group (Figure 3.6). The major difference between the subdivision of Lotze (1945, *in* Villaseca *et al.*, 2014) and of Villaseca *et al.* (2014) is the inclusion of the Las Hurdes-Sierra de Gata Massif in the Beiras Group.

A Major sedimentary hiatus between the Cambrian and the Early Ordovician (Armorican Quartzite) is represented by the Early Ordovician unconformity that has a regional character in the Central Iberian Zone (Balda *et al.*, 1990; Pereira *et al.*, 2012; Dias *et al.*, 2013). There are two theories that may explain this hiatus. Lotze (1956, *in* Diez Balda *et al.*, 1990) supported that this unconformity was produced by a deformation phase, denominated Sardic Deformation. The Sardic Deformation occurred during compressive regime (*ex. gr.*, RIbeiro, 1974, *in* Amaral *et al.*, 2014) caused by a transient inversion of the general extensional regime (Romão *et al.*, 2005, *in* Amaral *et al.*, 2014), and produced a weak folding without schistosity and regional metamorphism (Ortega and Lodeiro, 1986, *in* Balda *et al.*, 1990). Whilst, Pereira *et al.* (2012) defend that the extensional horizontal stresses during the Cambrian rift stage implied the basement structuration and the formation of rift shoulders, tilted blocks, and/or horsts and grabens, which were ultimately responsible by the Early Ordovician unconformity.

The Olho-de-Sapo and Urra Domains include two formations (Figure 3.5): (1) the Olho-de-Sapo Formation; and (2) the Urra Formation. The first is located in the northern border of the Central Iberian Zone, and comprises a porphyritic set of subvolcanic, volcanic and volcanoclastic rocks both from the Early Ordovician (Montes *et al.*, 2010, *in* Catalán, 2011). The Olho-de-Sapo Formation igneous units are underlying and partly intercalated with platform facies sediments, the designated Armorican Quartzite, and is overlying the Ediacaran-Cambrian Dúrico-Beirão Supergroup sequences. In turn, the second is situated in the southern boundary of the Central Iberian Zone, but it has similar facies and age of the Olho-de-Sapo Formation (Solá *et al.*, 2008, *in* Catalán, 2011). This formation may represent the continuation of the same volcanic axis (Catalán, 2011). The Urra Formation also stratigraphically underlies the Early Ordovician Armorican Quartzite, typical of the Central-Iberian Zone, however it unconformably overlies the previously deformed and metamorphosed Ediacaran sediments of the Série Negra, succession with Ossa-Morena Zone affinity (Solá *et al.*, 2008, *in* Catalán, 2011).

According to Balda *et al.* (1990), all the Central Iberian Zone structure was mostly deformed and metamorphosed by the Variscan Orogeny, producing appreciable internal deformation and metamorphism. The Variscan Orogeny overlapped three consecutive deformation phases in the present sequences, designated as (1) D_1, (2) D_2 and (3) D_3, and some later subvertical shear zones or faults. According to Arango *et al.* (2013), during the Paleozoic there were transferred terranes from peri-Gondwana to the Gondwana adjacent margin associated with crustal thickening (D_1). Still according to the same author, this transference and crustal thickening were followed by syn- and late-orogenic collapse of the orogenic belt developing intracontinental strike-slip systems and oroclinal bends (D_2 to D_3).

The D_1 originated the first continuous and penetrative deformation in the sequences of the Precambrian and the Paleozoic. Subvertical folds with a large wavelength and associated foliation (S_1) parallel to their axial plane were created in this deformation phase. The direction of these folds is variable, but the northwest-southeast direction predominates, and the inclination of the axes ranges substantially (Balda *et al.*, 1990). The production of these folds started an initial crustal thickening (*ex. gr.*, Balda, 1986, *in* Arango *et al.*, 2013). In turn, the D_2 is present in more localized areas and craeted new structures that overlapped over those ones of D_1, producing an internal deformation and fabric into the rocks (Balda *et al.*, 1990). It developed restricted to subhorizontal ductile bands (probably as a continuation of D_1) that are wider in the metasediments, extensional shear zones and thrust faults, and magmatic activity associated with thermal and gravitational re-equilibrium during the crustal thickening (*ex. gr.*, Balda *et al.*, 1990; Barbero, 1995, *in* Arango *et al.*, 2013). Finally, the D_3 developed open to tight upright folds, homoaxial with those D_1, subvertical or dipping to the east and northeast. Several sinistral and dextral subvertical transcurrent shear zones were also created contemporary with these folds. Later shear zones and faults were also originated with wrench movements or as normal accidents (Balda *et al.*, 1990; Catalán, 2011, *in* Arango *et al.*, 2013).

Tectonical- and structurally, Balda *et al.* (1990) subdivided the Central Iberian Zone into two domains (Figure 3.7) according to its megascopic structures of the D_1: (1) the Vertical Folds Domain to the south; and (2) the Recumbent Folds Domain to the North. Owing to the large amount of granitic intrusions, the definition of the limit between both domains becomes imprecise (Balda *et al.*, 1990). The former occupies the major part of Central Iberian Zone, where the terrains with low-grade metamorphism and narrow synclines are cropping out. While the latter is where the terrains with high-grade metamorphism are cropping out. However, high-grade metamorphism may crop out in some cores of antiforms of Vertical Folds Domain, and there are also large regions of low-grade metamorphism in the Recumbent Folds Domain (Balda *et al.*, 1990).

In the Central Iberian Zone, the Variscan deformation and metamorphism were also accompanied by syntectonic magmatism that originated dispersion of the Variscan granitoid plutons (Silva and Neiva, 1990). These plutons intruded a succession of metasediments between the Neoproterozoic and the Lower Carboniferous (*ex. gr.*, Ribeiro *et al.*, 1979, *in* Mateus and Noronha, 2010). The Central Iberian Zone is of all the segments of the Variscan Belt the one that has the major extension and a great diversity of granitoids cropping out (Azevedo and Aguado, 2006; Azevedo and Aguado, 2013). These granitoids were mostly formed during D_3 (*ex. gr.*, Iglesias and Ribeiro, 1981, *in* Ferreira *et al.*, 1987b; Azevedo and Aguado, 2006), and are distributed mainly by well-defined structural alignments (ductile shear zones; Ferreira *et al.*, 1987b; Mateus and Noronha, 2010). These meso- to tardi-Variscan granitoids, and shear zones reveal a spatial relationship with the main mineralization systems of Central Iberian Zone (Figure 3.8; Mateus and Noronha, 2010; Noronha *et al.*, 2013), producing them by granitic differentiation (Neiva, 1979).

The classification of the Variscan granitoids, are based on geological, geochronological, structural,

geochemical, and petrographical criteria (Ferreira *et al.*, 1987b). Schermechom (1986, *in* Ferreira *et al.*, 1987b) used geochronological and structural data to subdivide as oldest, older and younger granites; Capdevila and Floor (1970, *in* Ferreira *et al.*, 1987b) classified petrographically and geochemically the granitoids as alkaline and calc-alkaline. The fact that all authors recognized the importance of the Variscan Orogeny in the origin of those granitoids led Ferreira *et al.* (1987b) to classify them according to their installation period. Therefore, the Variscan granitoids are subdivided according to Ferreira *et al.* (1987b) as: (1) pre-orogenic; (2) synorogenic; and (3) tardi- to post-orogenic. The former includes the granitoides that are between 482 and 582 Ma old of gneissic facies with plane-linear texture. The seconds are subdivided in pre-D_3 and syn-D_3. The pre-D_3 granitoids are two-mica and biotite granites of S-type and peraluminous related to D_2; while the syn-D_3 granitoids are biotite with Ca-plagioclase granitoids, or two-mica or biotite granites, related to D_3. Finally, the latters comprise mostly biotite granites of I-type and slightly peraluminous that formed during the Late Carboniferous and Permian.

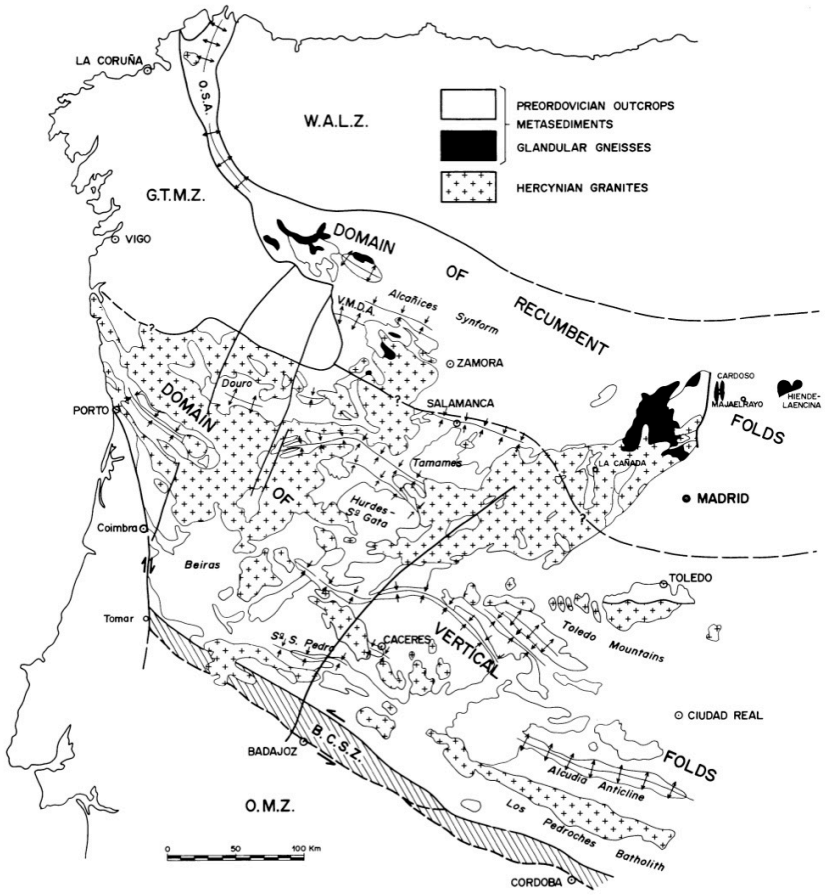

Figure 3.7 – Sketch showing the structural domains of Central Iberian Zone (Recumbent and Vertical Folds Domiains; Balda *et al.*, 1990).

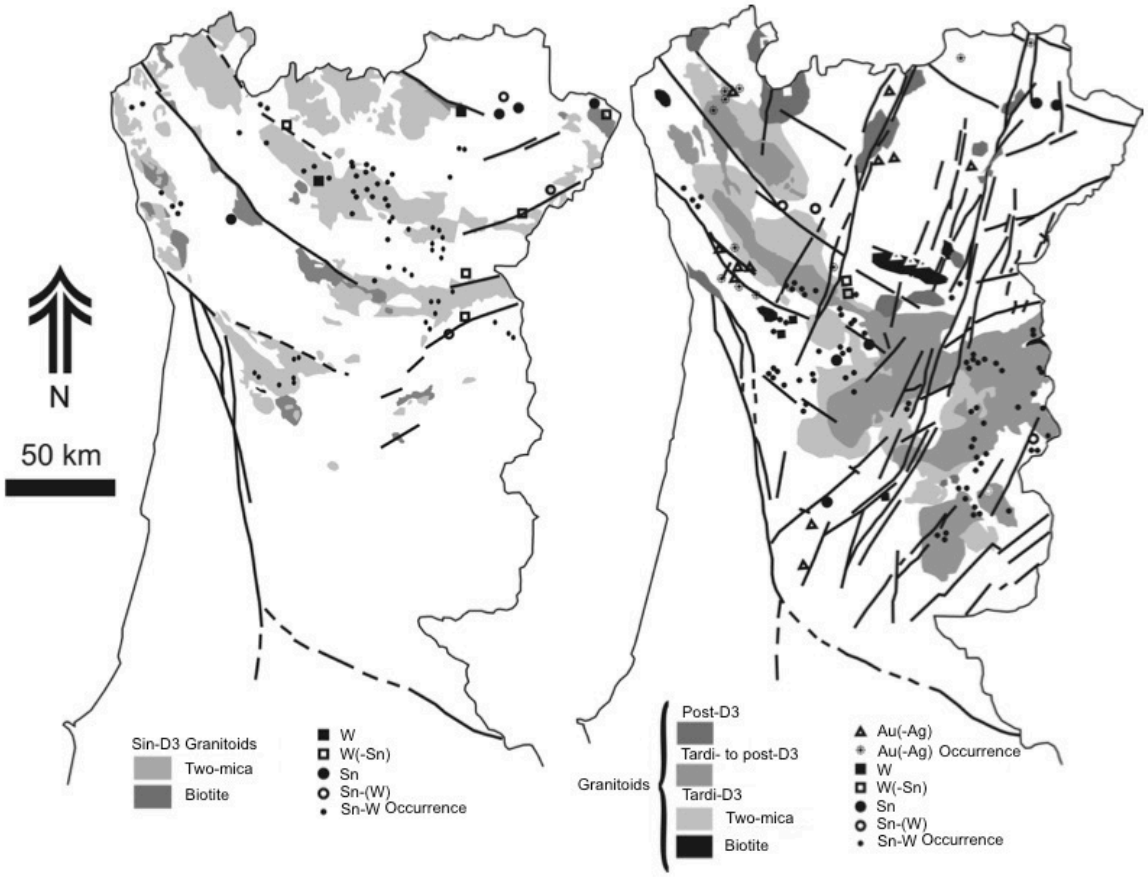

Figure 3.8 – Sketch showing the main mineralization systems spatial distribution of northern Portugal, and their relationship with the Variscan granitoids and Variscan shear zones (adapted from Mateus and Noronha, 2010).

3.1.4. Regional geology

As referred before, the case study is located in the Armamar-Penedono region that geologically comprises the Douro Group metasediments of the Dúrico-Beirão Supergroup (Figure 3.9), the Tabuaço Massif granitoids (Figure 3.10), and some aplites and pegmatites (Sousa, 1982; O'Donovan, 2012; Beare and MacDougal, 2013). The regional geology of the area is covered and represented in both 10-D Alijó and 14-B Moimenta da Beira Portugal's Geological Map at a scale of 1:50,000 (Sousa *et al.*, 1987; Ferreira *et al.*, 1987a; Sousa and Sequeira, 1989; Ferreira and Sousa, 1994).

Sousa (1979a, 1982, 1983) established the lithostratigraphy of the Douro Group. The same author in 1979 (Sousa, 1979a) started to define some lithostratigraphic units, which are from the base to the top: (1) Bateiras-Covas do Douro Crystalline Limestones and Black Schits; (2) Rio Pinhão-Ervedosa do Douro Greywackes; (3) Pinhão Chloritic Schist; (4) Desejosa Slate Schists; and (5) Castanheira do Sul Greywackes and Conglomerates. Later, the ultimate units gave rise to the actual formations of the Douro Group (Sousa, 1982, 1983). Those formations are six and are, from

the oldest to the latest (Figure 3.9): (1) Bateira Formation; (2) Ervedosa do Douro Formation; (3) Rio Pinhão Formation; (4) Pinhão Formation; (5) Desejosa Formation; and (6) S. Domingos Formation.

Afterwards, Silva and Ribeiro (1985, *in* Sousa, 1985) noticed the existence of a thrust fault in the Senhora do Viso region, named as the Senhora do Viso Thrust Fault. Supposedly, this thrust fault was produced during the Sardic Deformation Phase and, tectonically, duplicated the Douro Group while the deposition of the S. Domingos Formation was happening (Sousa, 1985). Therefore, the Rio Pinhão Formation is equivalent to the Bateiras Formation, the Pinhão Formation is equivalent to Ervedosa do Douro Formation, and the S. Domingos Formation is contemporary with the Senhora do Viso Thrust Fault. The duplication of the Douro Group led then to a subdivision in a group of autochthonous formations, which includes the Bateiras Formation and the Ervedosa do Douro Formation, and another of allochthonous formations that comprises the Rio Pinhão Formation, the Pinhão Formation and the S. Domingos Formation (Sousa, 1985). At this point it is possible to define each formation of the Douro Group.

The Bateiras Formation (autochthonous formation) is the basal formation of Douro Group and has unknown bottom limit (Sousa, 1982; Dias *et al.*, 2013). The known thickness of this formation is about 800 m (Sousa, 1982, 1983; Dias *et al.*, 2013). The Bateiras Formation is cropping out in some D_1 anticlines, such as the São Pedro das Águias Anticline (Sousa *et al.*, 1979; Sousa, 1982, 1983; Sousa *et al.*, 1987; Ferreira *et al.*, 1987a; Sousa and Sequeira, 1989; Ferreira and Sousa, 1994; Dias *et al.*, 2013). This formation includes metagreywackes, black graphitic phyllites, grey phyllites, and crystalline limestones (marbles), which give to the Bateiras Formation a black and tough appearance (Sousa, 1979a, 1982, 1983; Sousa and Sequeira, 1989; Ferreira and Sousa, 1994). The Bateiras Formation contains also scheelite skarns with economic interest (Sousa *et al.*, 1979; Sousa, 1981). These skarns are normally whitish to grey-greenish, but sometimes darkish (São Pedro das Águias), with thicknesses ranging from some centimeters to some meters (Sousa, 1981).

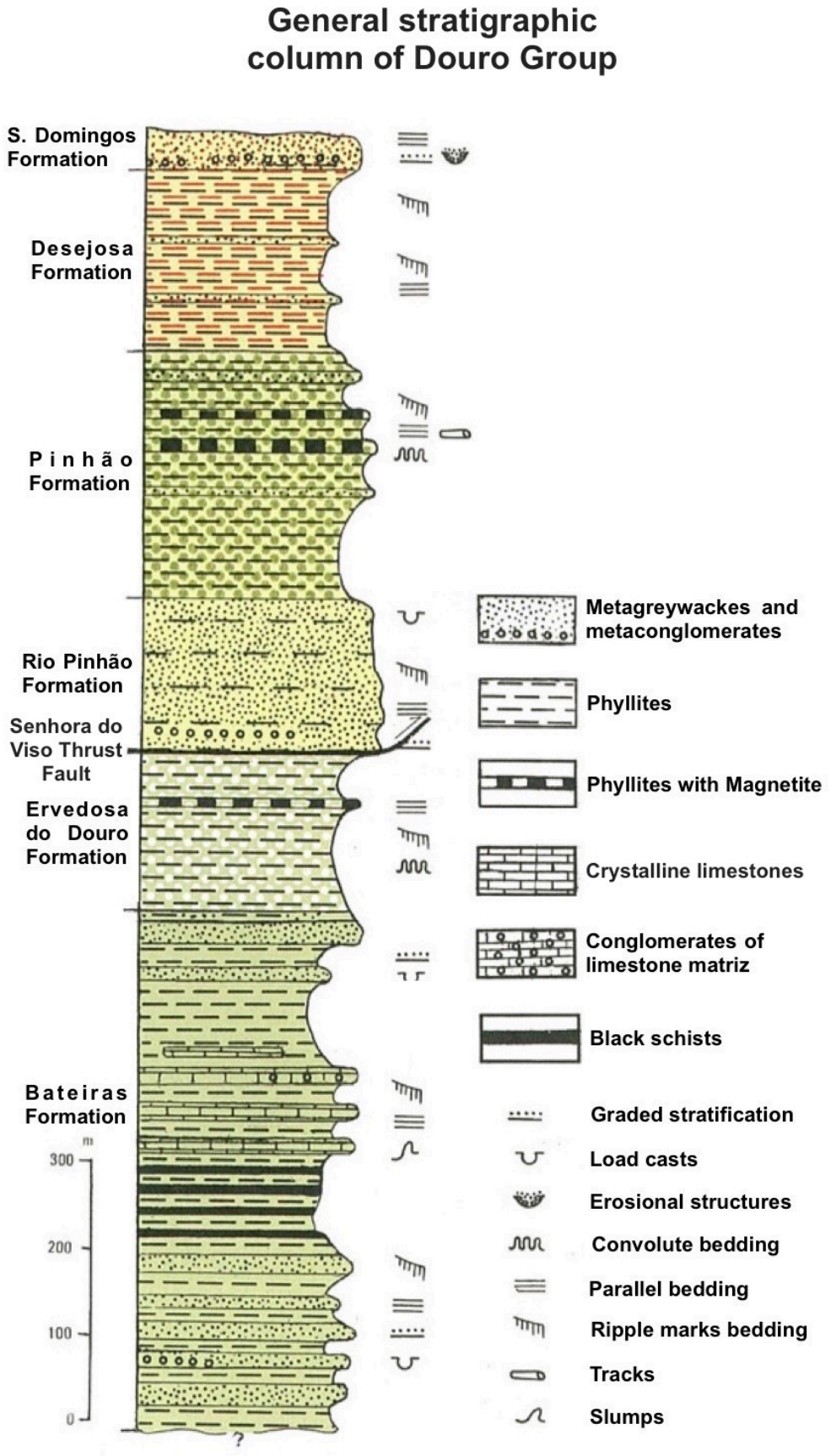

Figure 3.9 – Stratigraphic column of the Douro Group (adapted from Sousa and Sequeira, 1989).

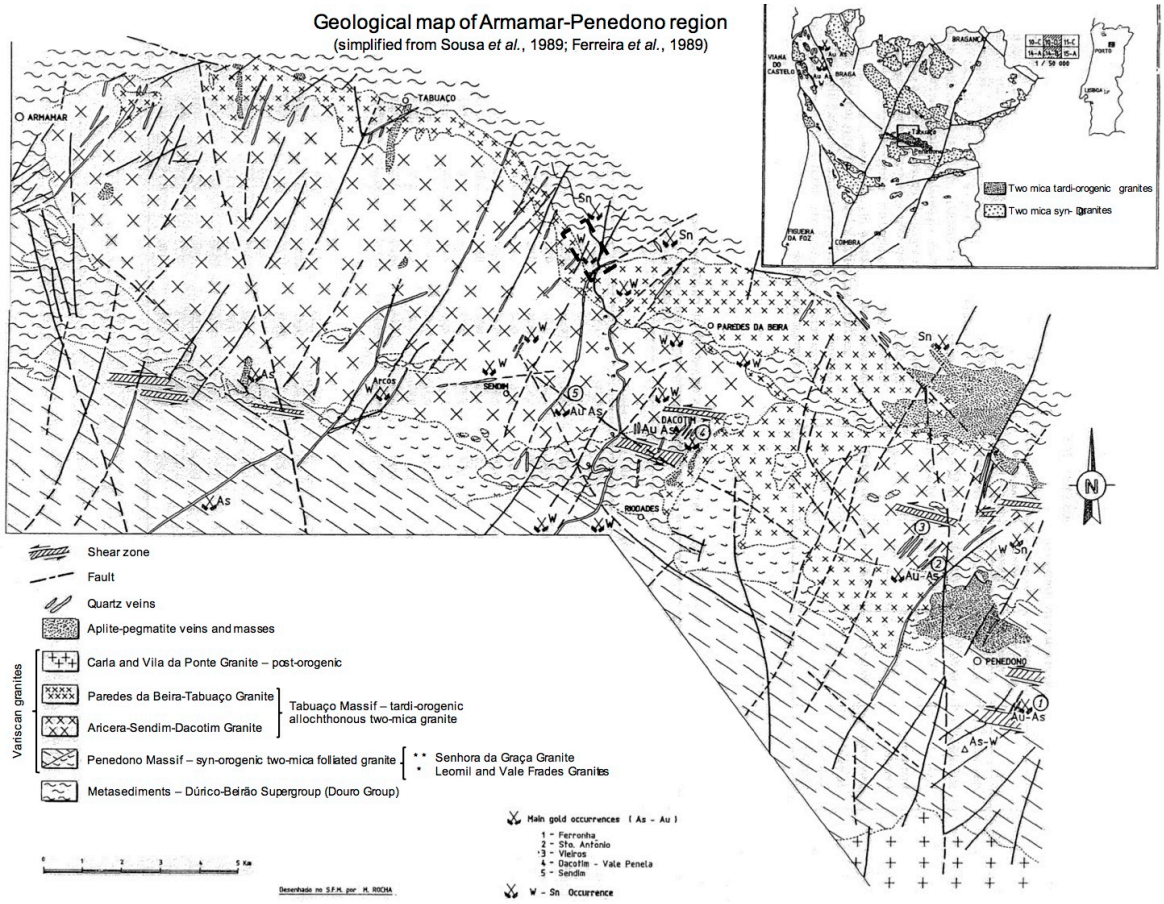

Figure 3.10 – Geological map of the Armamar-Penedono region; the dashed trapezium represents the approximated location of the São Pedro das Águias skarn deposit (adapted from Sousa and Ramos, 1991).

This autochthonous formation may also be divided into two members. The lower member encompasses black graphitic, grey phyllites, and metagreywackes; and the upper one comprises crystalline limestones, grey phyllites, and metagreywacke (Sousa, 1982, 1983; Sousa and Sequeira, 1989; Dias *et al.*, 2013). Near the village of Trevões, Sousa (1979b, 1982) verified that the crystalline limestones of the upper member pass laterally to conglomerates. The top of the Bateiras Formation is marked by black-stripped phyllites passing gradually to green thinly stratified phyllites, which serves as limit between this formation and the Ervedosa do Douro Formation (Sousa, 1982, 1983; Ferreira and Sousa, 1994).

The autochthonous Ervedosa do Douro Formation is characterized by being thinly stratified and green colored, composed by green chloritic phyllites, quartzo-phyllites, and metagreywackes, in which the coarser levels show cross-lamination structures (Sousa, 1979a, 1982, 1983; Dias *et al.*, 2013). The top of this formation is marked by the appearance of magnetite that passes to thicker bedded metagreywackes of the Pinhão Formation (Sousa, 1982, 1983; Sousa and Sequeira, 1989). The thickness of the Ervedosa do Douro Formation is about 250 m (Sousa, 1982, 1983;

Dias *et al.*, 2013). In this formation scarce skarns may also occur (Sousa, 1981).

The Rio Pinhão Formation is the basal formation of the Douro Group allochthonous formations, and is the equivalent to the Bateiras Formation owing to the Senhora do Viso Thrust Fault (Sousa, 1985; Sousa and Sequeira, 1989; Dias *et al.*, 2013). The thickness of Rio Pinhão Formation is about 250 m and it includes a succession of thick metagreywackes interbedded with thin and dark-grey phyllites, and some levels of microconglomerates. The metagreywake beds contain load casts, graded stratification, and cross-lamination (Sousa, 1979a, 1982, 1983; Sousa and Sequeira, 1989; Dias *et al.*, 2013). According to Sousa (1981), this formation contains skarns in metamorphic contacts, such as in Ervedosa do Douro. The Rio Pinhão Formation passes to the Pinhão Formation when the dark metagreywacke nature (Rio Pinhão Formation) is lost and starts a thinly green stratified series of phyllites and quartz beds (Pinhão Formation; Sousa, 1982, 1983).

The Pinhão Formation, the allochthonous formation similar and equivalent to the Ervedosa do Douro Formation (Sousa, 1985; Sousa and Sequeira, 1989; Dias *et al.*, 2013), includes a thinly green stratified sequence of quartz beds and green quartz phyllites (Sousa, 1979a, 1982, 1983; Sousa and Sequeira, 1989; Dias *et al.*, 2013). Its average thickness is 350 m. During all the sequence, there occur cross-lamination and convolute bedding; and the upper half of this succession is marked by the presence of magnetite (that gives a mottle effect to the phyllites) and pyrite cristals (Sousa, 1979a, 1982, 1983; Sousa and Sequeira, 1989; Dias *et al.*, 2013). The Pinhão Formation passes to the Desejosa Formation gradually, but suddenly by the disapearence of the typical succession of the Pinhão Formation, and the occurrence of a dark pelitic sequence with thin whitish quartz beds from the Desejosa Formation (Sousa, 1982, 1983). As in the Ervedosa do Douro Formation, in the Pinhão Formation scarce skarns can also occur (Sousa, 1981).

The Desejosa Formation has a average thickness of 250 m in the Tabuaço region (Sousa, 1982, 1983; Dias *et al.*, 2013), and in the Freixo de Espada à Cinta the thickness is about 1200 m (Silva and Ribeiro, 1994, *in* Dias *et al.*, 2013). This formation includes the alternation of dark phyllites with thin whitish quartz beds, and layers of coarse metagreywackes; and, at the top, comprises an intra-formed conglomerate in a metagreywacke bed. The sedimentary structures contained in the Desejosa Formation are graded stratification, load casts, scarce cross-lamination and convolute bedding, and parallel lamination in the metagreywackes (Sousa, 1979a, 1982, 1983; Sousa and Sequeira, 1989; Dias *et al.*, 2013). This formation may also contain some thin skarns, for instance in Barca d'Alva (Sousa, 1981). The top of the Desejosa Formation is marked by the presence of thin metagreywackes beds. These beds are thicker when they pass to conglomerates intercalated with metagreywackes layers of the S. Domingos Formation (Sousa, 1979a, 1982, 1983).

The upper and last formation of the Douro Group is the S. Domingos Formation, with an unknown top (Sousa, 1982, 1983; Dias *et al.*, 2013). The S. Domingos Formation contains thick conglomerates (with mainly quartz, limestone, phyllites, and metagreywacke pebbles) interlayered with massif metaquartzarenites, and has no pelitic materials. The formers include parallel

lamination at the base, and cross-lamination; while the latters comprise erosional figures at the base, and positive graded stratification. Its known thickness is about 50 m (Sousa, 1979a, 1982, 1983; Sousa and Sequera, 1989; Dias *et al.*, 2013). According to Dias *et al.* (2013), the Senhora do Viso Thrust Fault may have uplifted a region of the granitic basement, which the limestone pebbles of the Bateiras Formation could have fed these conglomerates.

The tectonic setting of this region is associated with the Malpica-Lamego Shear Zone. This is a mega-shear zone oriented northwest-southeast, and is parallel to the Varisca Belt for 275 km (Castro *et al.*, 2010). According to Sousa (1982), this region is defined by the existence of three main structures in the Dúrico-Beirão Supergroup, which line-up in the northwest-southeast direction with the Malpica-Lamego Shear Zone: (1) the Abaças-Custódias Anticline; (2) the Santa Leucádia-São Pedro das Águias Anticline; and (3) the Adorigo Anticline. The former has a subvertical axial plane in which the south flank is cut off by a fault, and could represent the continuation of the Marão Anticline. The second is situated next to the Tabuaço Massif in which in Santa Leucádia is tumbled, but in São Pedro das Águias is asymmetric with the south flank intruded by the massif. The latter has an axial plane tumbled 60-70° to north. All these anticlines mark the actuation of D_1 and the Bateiras Formation crops out in the inner part. The synclines between them are usually of larger range and have numerous undulations in the inner zone. The region is still conditioned to two major fracturation systems. One fracturation system northeast-southwest (10-20°), which is materialized by tardi-Variscan quartz veins; and another northwest-southeast that is connected with thrust faults.

The Tabuaço Massif is an elongated shaped massif, oriented northwest-southeast and aligned with the involving structures, the anticlines of the Dúrico-Beirão Supergroup metasediments and the Malpica-Lamego Shear Zone (Figure 3.10; Sousa and Macedo, 1985; Sousa *et al.*, 1987; Ferreira *et al.*, 1987a, 1987b, 1987c; Sousa and Sequeira, 1989; Ferreira and Sousa, 1994). This massif comprises the northern border of a regional granitic anticline that extends itself from Lamego to Figueira de Castelo Rodrigo (Ferreira *et al.*, 1987b; Sousa and Sequeira, 1989; Ferreira and Sousa, 1994). The massif is making contact in the northern part with the São Pedro das Águias Anticline, in which the border is made by small faults, and in the southern part with the Penedono and Vale Frades Massifs (Sousa *et al.*, 1987; Ferreira *et al.*, 1987a, 1987c; Sousa and Sequeira, 1989; Ferreira and Sousa, 1994).

The Tabuço Massif is divided in three granitic facies, which are from the external to the inner zone of the massif (Figure 3.10): (1) Paredes da Beira-Tabuaço Granite; (2) Laboreira Granite; and (3) Aricera-Sendim-Dacotim Granite (Sousa and Sequeira, 1989; Silva and Neiva, 1990; Ferreira and Sousa, 1994). These granites of the massif may have been intruded by continuous pulsations (Ferreira *et al.*, 1987c), and are considered two-mica, leucocratic, alkaline, slightly foliated, muscovite-biotite (with muscovite predominant), S-type peraluminous, syn- to tardi orogenic (310 to 316 Ma old) granites (Sousa, 1982; Ferreira *et al.*, 1987b, 1987c; Sousa and Sequeira, 1989; Silva and Neiva, 1990; Sousa and Ramos, 1991; Ferreira and Sousa, 1994; Neiva, 2002). The

Tabuaço Massif, namely the Paredes da Beira-Tabuaço Granite, is responsible by the metamorphic contact, and related metasomatism, which originated a metamorphic aureole in the Douro Group metasediments (Sousa, 1982, 1985).

The Paredes da Beira-Tabuaço Granite comprises the border facies of the Tabuaço Massif, and is making the northern and northeastern contact with the Douro Group metasediments (Figure 3.10). This granite is medium- to coarse grained, sometimes porphyritic, contains muscovite with scarce biotite, tourmaline, and some spread sulphides. The Laboreira Granite is the intermediate facies of the massif, passing gradually to the Paredes da Beira-Tabuaço Granite. The Laboreira Granite is medium- to coarse-grained, moscovitic-biotitic, and sheared. Finally, the Aricera-Sendim-Dacotim Granite (Figure 3.10) is located in the inner part of Tabuaço Massif, and is the bigger portion of the massif, with a well-defined limit between itself and the Laboreira Granite. It is also fine- to medium-coarse grained, muscovitic-biotitic, and sometimes porphyritic granite (Sousa, 1982; Sousa and Macedo, 1985; Ferreira *et al.*, 1987c; Sousa and Sequeira, 1989; Ferreira and Sousa, 1994).

Related to the Tabuaço Massif, smaller (of metric dimensions) intrusive bodies are frequent and usually fulfill the fractures in the pre-existent rocks (Silva and Neiva, 1990; Sousa and Ramos, 1991; Ferreira and Sousa 1994). These smaller intrusive bodies are frequent in all the granites of the Tabuaço Massif, however more abundant in the Douro Group metasediments near the contact with the Paredes da Beira-Tabuaço Granite. In the metasediments their orientation is according to the Dúrico-Beirão Supergroup structures and to the Tabuaço Massif (Sousa, 1982; Sousa and Macedo, 1985). They are of two types: (1) veins; and (2) aplites and pegmatites (Figure 3.10). The formers are quartz veins fulfilling fractures mostly oriented northeast-southwest. The main ones materialize bigger tardi-Variscan faults, such as the São Pedro das Águias-Monte Verde-Rua-Caria Vein. Whilst the latters are normally oriented northwest-southeast (parallel with the structure of the host rocks) and associated with the Tabuaço Massif. Their thicknesses are metric, and they include disseminated cassiterite, in which some of them were exploited (Ferreira and Sousa, 1994).

3.1.5. Local geology

The São Pedro das Águias skarn ore deposit is located in the western flank of the Távora River, namely in the São Pedro das Águias Anticline. It is materialized by the metasediments of the Bateiras Formation, near the contact of that formation with the Paredes da Beira-Tabuaço Granite (Sousa *et al.*, 1979; O'Donovan, 2012; Beare and MacDougal; 2013; Figure 3.11). The São Pedro das Águias Anticline, the most important structure in this area, comprises the southeastern part of a major one, the Santa Leucádia-São Pedro das Águias Anticline (Figure 3.11; Sousa *et al.*, 1987; Ferreira *et al.*, 1987a; Sousa and Sequeira, 1989; O'Donovan, 2012; Beare and MacDougal, 2013). The asymmetric São Pedro das Águias Anticline axial plane is striking to the norhtwest with the fold displaying a vergence to the southwest. The southern flank bedding is oriented northwest-

southeast and is intruded by the Tabuaço Massif. The Bateiras Formation is cropping out in its core (Sousa *et al.*, 1979; Sousa, 1982; Ferreira and Sousa, 1994).

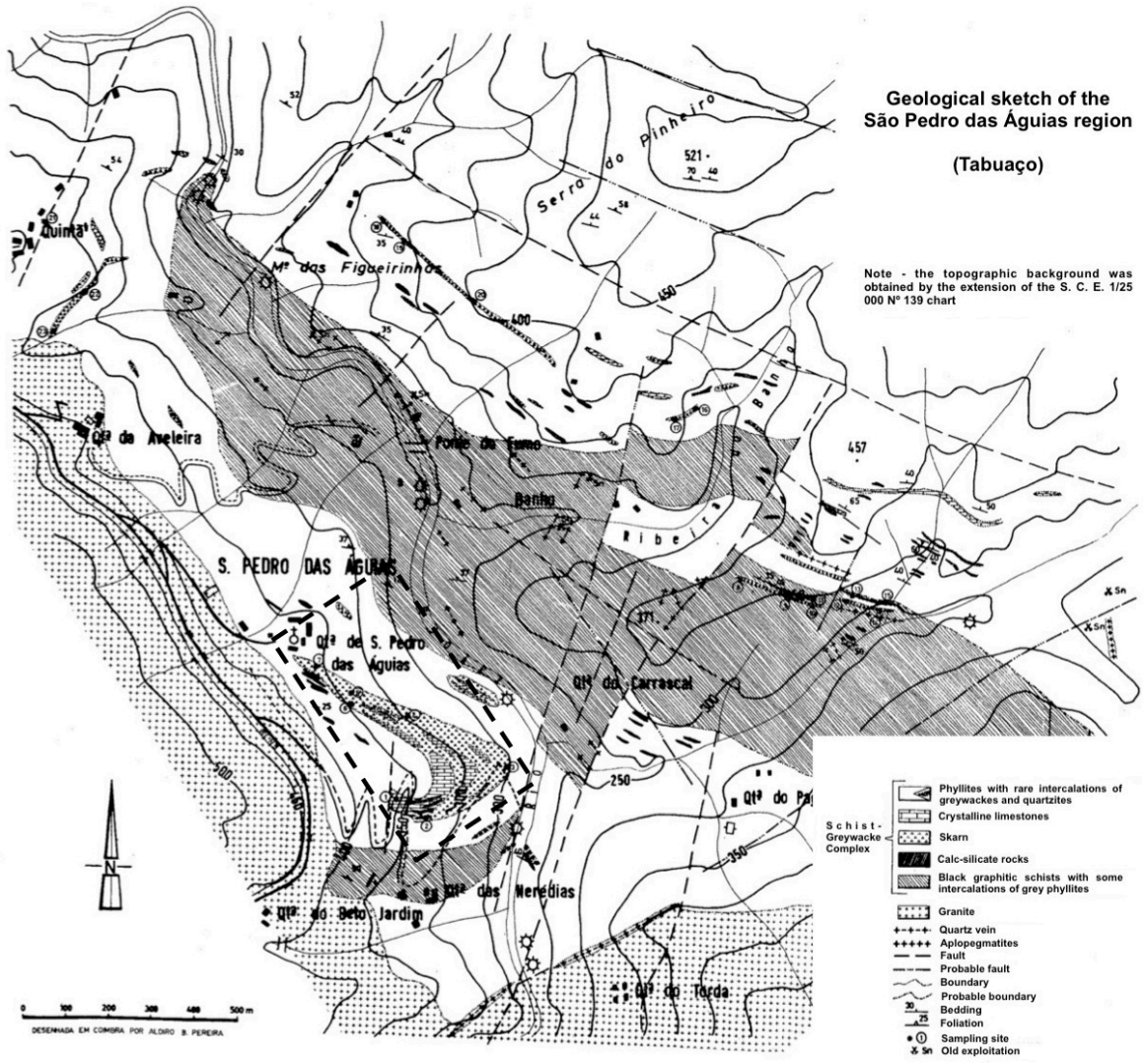

Figure 3.11 – Geological map of the São Pedro das Águias area; the dashed trapezium represents the approximated location where the skarns are cropping out (adapted from Sousa, 1979).

There are also fractures or brittle faults, which normally represent minor structures with some exceptions. Those structures are oriented north 60º to west, and north-south to north-northeast–south-southwest and some of them may be quartz veins, which are crosscutting the metasediments. One local brittle structure corresponds to the São Pedro das Águias Quartz Vein (with displacements in the order of a few meters) that marks the contact between the Tabuaço Massif and the Douro Group, (Figure 3.11; Sousa *et al.*, 1979; O'Donovan, 2012; Beare and MacDougal, 2013).

The metasedimentary rocks that host the skarn mineralization in the São Pedro das Águias area

are interpreted here as belonging to the Bateiras Formation. In this area both (1) lower, and (2) upper members of the Bateiras Formation are exposed (Figure 3.11; Sousa, 1982, 1983; O'Donovan, 2012; Beare and MacDougal, 2013). The lower member includes black schists with some intercalations of grey phyllites of lepido-granoblastic texture and a mineral association comprising graphite, quartz, muscovite, biotite, chlorite, pyrite (and other opaques), and no calc-silicate minerals. The lithologies of this member are unaffected by hydrothermal alteration (black graphitic schists with some intercalations of grey phyllites in Figure 3.11). The upper one (phyllites with scarce intercalations of greywackes and quartzites) corresponds to biotite and chloritic schists of lepido-granoblastic texture and a mineral assemblage composed by quartz, muscovite, biotite, chlorite, opaques, calc-silicate minerals (usually epidote), and minor calcite (Figure 3.11; O'Donovan, 2012; Beare and MacDougal, 2013; Cerejo, 2013; Cerejo *et al.*, 2014).

The Bateiras Formation upper member in the area also includes (1) carbonate rocks, (2) calc-silicate rocks, and (3) skarns (Sousa *et al.*, 1979; Sousa, 1982, 1983; O'Donovan, 2012; Beare and MacDougal, 2013; Cerejo, 2013; Cerejo *et al.*, 2014). All of these rock types are affected by thermal metamorphism, metasomatic replacements and hydrothermal alteration; and, according to José *et al.* (1990) are cropping out in narrow bands representing discontinuous lenticular- or lens-shaped bodies (Figure 3.11). The carbonate rocks are characterized by impure, un-mineralized marbles with a lepido-, nemate-, or granoblastic texture and with a mineral association composed by calcite, quartz, epidote, sphene, biotite, chlorite, muscovite, amphibole (tremolite-actinolite), apatite, and opaques. The calc-silicate rocks have a granoblastic texture with a mineral association that includes quartz, epidote, Ca-clinopiroxene, calcite, sphene, sericite, chlorite, plagioclase, biotite, apatite, and opaques (Cerejo, 2013; Cerejo *et al.*, 2014).

Finally, the skarns present a granoblastic and inequigranular texture (Cerejo *et al.*, 2014), showing a pale color between greyish and greenish bands, presenting a slight anisotropy and arched alignment (Fernandes *et al.*, 2015). This mineral preferred alignment is marked by large grains of vesuvianite forming a mineralogical band intercalated with an intergrowth of aluminosilicates (Fernandes *et al.*, 2015). The most common minerals are vesuvianite, and fluorite, associated with epidote (as smaller grains included in fluorite), clinozoisite, zoisite, fluorvesuvianite, scheelite (as smaller grains), titanite, cassiterite, albite plagioclase, grossular garnet, idiocrase, amphibole, diopside, sphene, quartz, muscovite and apatite (Sousa, 1982; O'Donovan, 2012; Beare and MacDougal, 2013; Cerejo *et al.*, 2014; Fernandes *et al.*, 2015). The aluminosilicates are difficult of identification, and their mineralogy reveals a total alteration suggesting the involvement of a metasomatic process (Fernandes *et al.*, 2015). As referred in the last subsection, these skarns are classified as W skarns (O'Donovan, 2012; Beare and MacDougal, 2013; Cerejo, 2013).

Two types of granitoids were emplaced in the host metasediments: (1) the Paredes da Beira-Tabuaço Granite; and (2) the aplites and pegmatites (Figure 3.11). The former is a medium-grained, equigranular, muscovitic granite with tourmaline, presenting an intrusive contact dipping to southwest (Figure 3.12). As major minerals, this granite presents quartz, albite plagioclase,

microcline and muscovite; and as minor ones, reports biotite, apatite, zircon, and opaques. The aplites are fine-grained, with quartz, microcline, Na-rich end-member (albite) plagioclase, and muscovite as main minerals; and tourmaline as minor mineral. The pegmatites are coarse-grained, with prevailing microcline (O'Donovan, 2012; Beare and MacDougal, 2013; Cerejo, 2013; Cerejo *et al.*, 2014). The granitoids of the area are all of the S-type, and have Rb-Sr ages of 311±7 Ma old (Cerejo, 2013; Cerejo *et al.*, 2014).

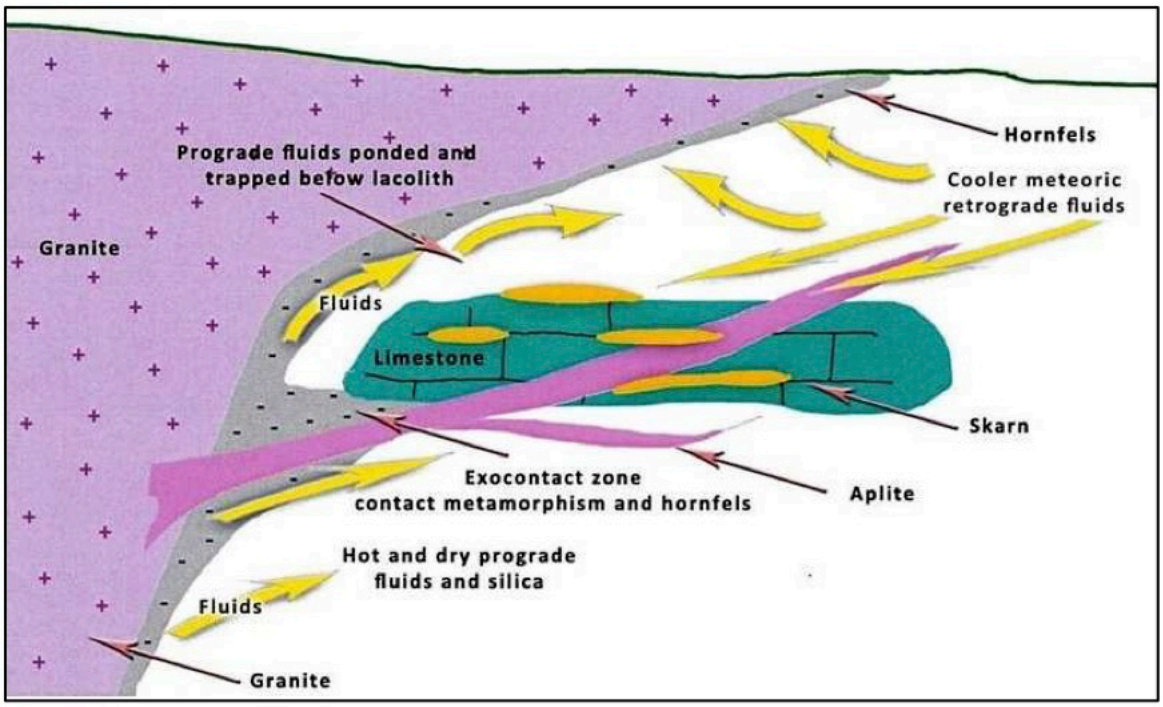

Figure 3.12 – Schematic cross-section showing a simplified paragenesis of the São Pedro das Águias skarn ore deposit (O'Donovan, 2012; Beare and MacDougal, 2013).

These ore deposit skarns contain both mineralizations of scheelite (W) and cassiterite (Sn) with no evidences of sulphides. The cassiterite mineralizations may also be included in the quartz veins, aplites and pegmatites (Sousa, 1982; Ferreira and Sousa, 1994; Neiva, 2001). The skarns and the calc-silicate rocks of the area are, as referred before, products of the metamorphism and related metasomatism in the limestones and carbonate metagreywackes of Bateiras Formation (Sousa, 1982), induced by the granitic emplacement and differentiation of the Tabuaço Massif (Neiva, 1979). Therefore, the mineralizations are practically restricted to the metamorphic aureole produced by those granites (Sousa, 1982). The skarn formation may have resulted by the successive pulses of magma and dykes recharges, which created a heat flow and a reflux effect in the cooler meteoric fluids that were replaced by hotter rising fluids (O'Donovan, 2012; Beare and MacDougal, 2013). The position and shape of Paredes da Beira-Tabuaço Granite also created a barrier that trapped the fluids and gave enough time for the actuation of the metamorphism and

metasomatism to the development of the mineralization (Figure 3.12; O'Donovan, 2012; Beare and MacDougal, 2013).

3.2. Available database

As mentioned before, the dataset that supports the present study was provided by Colt. The database comprises several tables and includes information about the drilling campaign carried out by the company until November of 2014. The information encompasses the location of the drill-holes, the intersected lithologies, mineralizations and alteration types, and the elements fingerprints. From this dataset, the used information comprised: (1) drill-holes initial and final easting, northing and elevation (X, Y and Z, respectively) coordinates; (2) drill-hole lengths; (3) intersected lithologies or lithological groups; (4) intersected hydrothermal alteration types; (5) W and Sn grades measures on the drill-holes; and (6) the remaining elements fingerprints.

A total of 163 drill-holes divided by 25 cross-sections spaced 25 m that are spread by the study area and lined northeast-southwest (namely north 30° to east; Figures 3.13 and 3.14) were used. The drill-holes were mostly realized doing a fan-shaped sharing approximately the same position at their mouths and drilled roughly north 30° to east with an average dip of about 74° as it is possible to verify in Figures 3.14 and 3.15. The total drilled is approximately 19,500 m of sampling cores, achieving a maximum depth of about 281 m and a mean depth of about 120 m. Concerning the metal grades, the W reaches a maximum grade of 2.14% and a mean of 0.11%; while the mean grade of Sn is 0.03 and the maximum is 0.24.

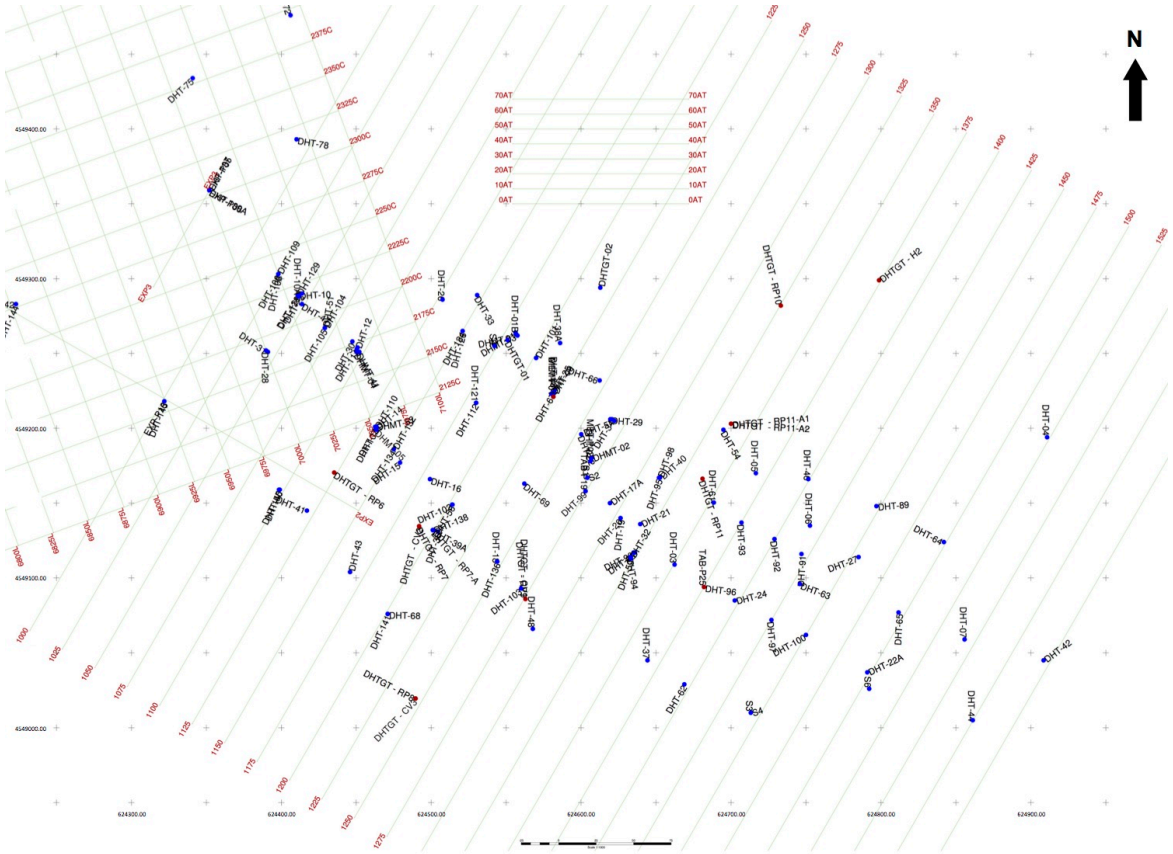

Figure 3.13 – Sketch showing the drill-holes distribution through the study area (adapted from Colt, 2014).

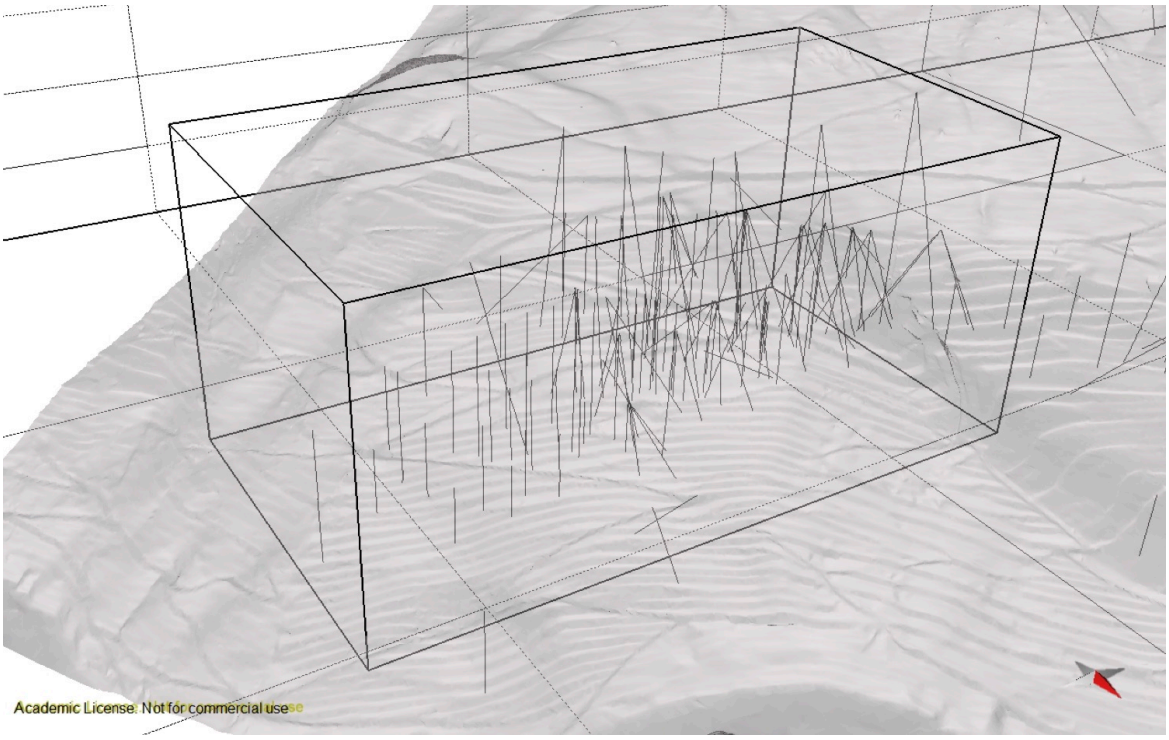

Figure 3.14 – Southeastern view of the study volume and drill-holes with a clockwise rotation of 30° constrained by the DTM.

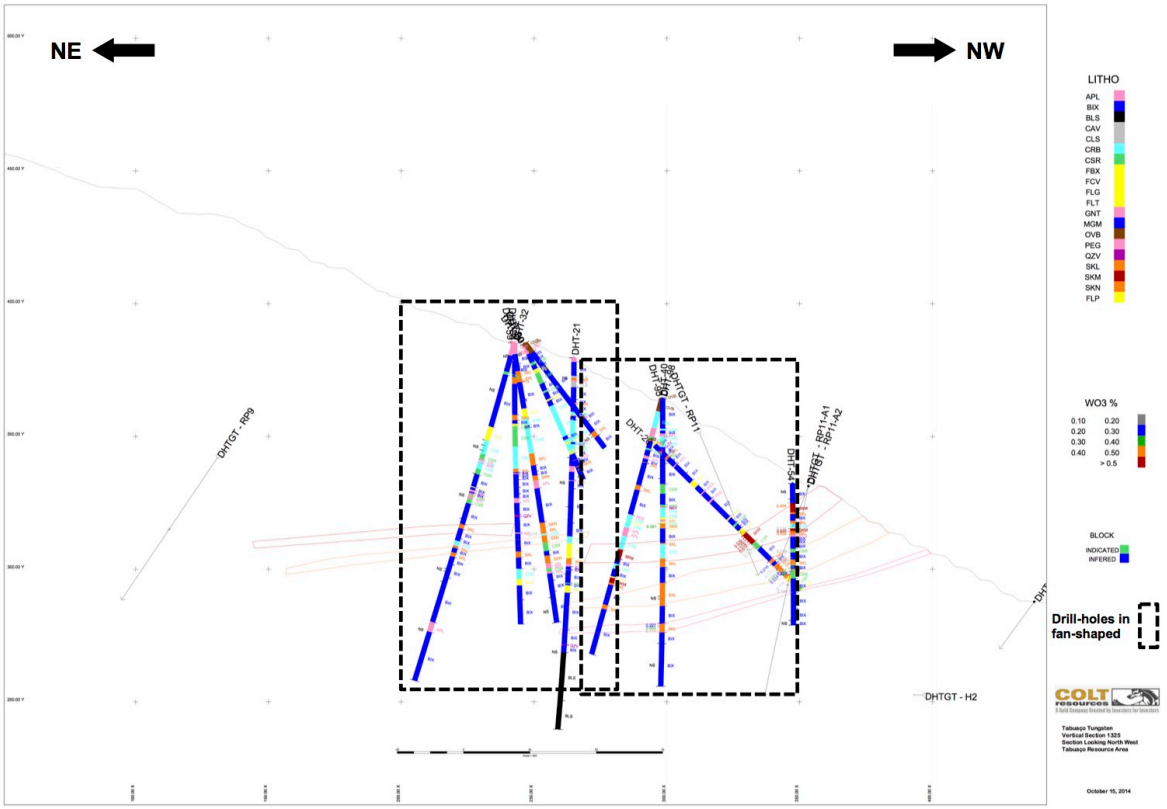

Figure 3.15 – Example of a geologists' hand drawn cross-section to demonstrate the drill-holes fan-shaped and their dip (adapted from Colt, 2014).

3.3. Multivariate analysis of correlations between elements fingerprints, lithologies and hydrothermal alteration types

This subsection tests the main associations between lithologies and hydrothermal alterations of the São Pedro das Águias skarn ore deposit with the goal of improving the knowledge about the deposit itself. In order to find these associations, a large dataset was used, and a multivariate tool was applied, the Principal Component Analysis (PCA) algorithm (Gomes *et al.*, 2015d).

3.3.1. Multivariate analysis by PCA

The multivariate statistics have risen up from the difficulty of the human mind, in understanding, analysing and finding relationships in simultaneous measurements on several variables, *i.e.*, in a huge dataset (Johnson and Wichern, 2002). Therefore, the multivariate statistics encompass a set of statistical methods and tools that enable simultaneous analysis of associations between multiple measurements of two or more variables (Reis, 1997). The main goals of these methods and tools include (Reis, 1997; Johnson and Wichern, 2002): (1) reduction or structural simplification of a dataset without losing important data or information; (2) sorting and grouping variables based on

the measured features; (3) examination of the dependence between variables; (4) compression of a dataset; (5) prediction of values of some variables based on the analysis of other ones; and (6) construction and testing of hypotheses.

Specifically, the PCA algorithm is a multivariate method of analysis. This method allows the transformation of a set of correlated variables in another set of uncorrelated ones, which results from linear combinations of the original set. The latter variables are called principal components or factors (PC or F, respectively; Reis, 1997). The main goals of the PCA algorithm are (Reis, 1997; Johnson and Wichern, 2002): (1) the reduction of the dimensionality of a dataset; (2) the compression of the dataset; and, finally, (3) the interpretation of a dataset. Therefore, the PCA method improves the interpretation of larger datasets, revealing relationships that would be difficult to understand without any transformation.

3.3.2. Preliminary data analysis

The dataset used for this study encompasses: (1) sample coordinates; (2) chemical elements fingerprints; (3) hydrothermal alteration types; and (4) lithologies or lithological groups. This data was observed and measured in the drill-hole cores realized in the São Pedro das Águias skarn deposit. The main objective of this sampling campaign was mainly the skarn lithologies, however all lithologies were also sampled.

The initial dataset included 5626 samples, distributed by 115 drill-holes, and 50 chemical elements, but some cores were not completely chemically analysed. Therefore, those ones were discarded and the complete dataset ended up having 2673 samples, distributed by 75 drill-holes, and 44 chemical elements. There were also many samples with contents under or above the limit of detection, thus, for those samples, their limit of detection was considered. Afterwards, the lithologies and the hydrothermal alteration types were joined to the dataset from the identification of the samples, because they were in different datasets of the database.

The 44 chemical elements used for the PCA were (Gomes *et al.*, 2015d): (1) Ag; (2) Al; (3) As; (4) Ba; (5) Be; (6) Bi; (7) Ca; (8) Cd; (9) Ce; (10) Co; (11) Cr; (12) Cu; (13) Fe; (14) Ga; (15) Ge; (16) K; (17) La; (18) Li; (19) Mg; (20) Mn; (21) Mo; (22) Na; (23) Nb; (24) Ni; (25) P; (26) Pb; (27) Rb; (28) S; (29) Sb; (30) Sc; (31) Se; (32) Sn; (33) Sr; (34) Ta; (35) Te; (36) Th; (37) Ti; (38) Tl; (39) U; (40) V; (41) W; (42) Y; (43) Zn; and (44) Zr.

The used variables included (Gomes *et al.*, 2015d): (1) the lithologies or lithological groups (which are groups of similar lithologies; Tables 3.1); and (2) the hydrothermal alteration types (Tables 3.2). The former are comprised by: (1) skarns layered to massive; (2) skarns layered; (3) skarns indifferentiated; (4) aplites; (5) granites; (6) pegmatites; (7) migmatites; (8) quartz veins; (9) carbonates, which is a lithological group composed by carbonate rocks (metalimestones), calcschists, calcsilicate rocks, and poorly developed skarns; (10) schists as another lithological group that includes biotite schists, and black/dark schists; (11) faults, which is also other

lithological group comprised by obvious faults, faults filled with gauge, breccia faults, and probable faults; and (12) core losses, or solution cavities. The hydrothermal alteration types encompassed: (1) silication or silicification; (2) chlorite alteration; (3) sericitic alteration; (4) carbonate alteration; (5) epidotite alteration; and (6) non classified samples.

According to Table 3.1, the schists are the most representative lithological group, representing 50.02% of the samples and 55.85% of the total meters sampled; while the least representative lithology is represented by the migmatites, with 0.07% of the samples and of the total meters sampled. In turn, Table 3.2 shows that silication or silicification is the most representative hydrothermal alteration type, representing 37.86% of the samples and 40.07% of the total meters sampled; whilst the carbonate and the epidotite are the least representative hydrothermal alteration types, each with 0.30% of the samples, but 0.25 and 0.35 of the total meters sampled, respectively.

Table 3.1 – Sampled lithologies and associated representativity.

Lithologies or lithological groups	Number of samples	Percentage of samples (%)	Meters sampled	Percentage of meters sampled (%)
Skarn layered to massive	265	9.91	283.76	7.60
Skarn layered	371	13.88	400.09	10.71
Skarn indifferentiated	123	4.60	130.55	3.50
Aplite	147	5.50	227.50	6.09
Granite	12	0.45	18.35	0.49
Pegmatite	3	0.11	4.45	0.12
Migmatite	2	0.07	2.45	0.07
Quartz vein	10	0.37	17.30	0.46
Carbonates	300	11.22	394.09	10.55
Schists	1337	50.02	2086.13	55.85
Faults	94	3.52	153.87	4.12
Core loss or solution cavity	9	0.34	16.65	0.45
Total	2673	100.00	3735.19	100.00

Table 3.2 – Sampled hydrothermal alteration types and associated representativity.

Hydrothermal alteration types	Number of samples	Percentage of samples (%)	Sampled meters	Percentage of sampled meters (%)
Silication or silicification	1012	37.86	1496.55	40.07
Chlorite	71	2.66	109.47	2.93
Sericitic	18	0.67	28.00	0.75
Carbonate	8	0.30	9.25	0.25
Epidote	8	0.30	13.20	0.35
Non classified	1556	58.21	2078.72	55.65
Total	2673	100.00	3735.19	100.00

3.3.3. Results

This dataset was analysed in the PCA. Table 3.3 presents the first five PC or F. The F1 and F2 represent 26.30% and 12.25 of global variance with eigenvalues of 11.57 and 5.39, respectively (Table 3.3), therefore the results are presented in scatter plots of individuals by F1 and F2 (Figures 3.17, 3.18 and 3.19). The Figure 3.16 demonstrates that the F2/F1 are overlapped with the chemical elements. When analysing this scatter plot it is possible to identify three sets of variables: (1) **set 1** is negatively correlated with F1, and comprises Fe-Co-Ni-Cu, K-Ba-Al-Sc-Zr-Th-V, and Ce; (2) **set 2** is positively correlated with F2, and is composed by Na-Rb-Nb-Ta, and Tl; and (3) **set 3** is positively correlated with F1 and negatively correlated with F2, and is composed by Sn-W-Sb, Be-Ca-Sr, and Bi. The chemical elements Ag-Zn-Cd-Ga-Ge-As-S-Se-Te-Mo-Pb, and Li-Mg-Y-La-Ti-P-Cr-U-Mn are not correlated with any of this two first components.

Table 3.3 – First five factors and respective eigenvalues and variances.

Factor	Eigenvalues	Variance (%)	Cumulative variance (%)
1	11.57	26.30	26.30
2	5.39	12.25	38.55
3	3.46	7.87	46.42
4	2.20	5.00	51.42
5	1.96	4.45	55.87

Both Figures 3.17 and 3.18 correspond to scatter plots where the individuals by each external variable, *i.e.*, the lithologies or lithological groups, and the hydrothermal alteration types, respectively, are projected. Figure 3.17 shows that faults are spread by the scatter plot. It is also possible to identify three sets of samples: (1) **set I** is projected in the negative axis of F1, and is encompassed by schists, migmatites, quartz veins, and a major portion of the faults; (2) **set ii** is projected in the positive axis of both F1 and F2, and comprises the aplites, and the granites; and (3) **set iii** is projected in the positive axis of F1, where the skarns and carbonates are individualized, and the skarns layered to massive are clearly isolated from the carbonates and the other skarns (Gomes *et al.*, 2015d).

The Figure 3.18 shows that silication or silicification, and chlorite alteration are widely spread by the scatter plot. Three sets of samples similar to the scatter plot of Figure 3.18 are also individualized: (1) **set a** is projected in the negative axis of F1, and is comprised by a higher quantity of silication or silicification, and fewer chlorite and sericitic alterations; (2) **set b** is projected in the positive axis of both F1 and F2, and includes silication or silicification, and chlorite and epidotite alterations; and (3) **set c** is projected in the positive axis of F1, and is composed by a small amount of chlorite, carbonate and epidotite alterations, and silication or silicification. A sample of sericitic alteration is situated near **set b**, and two of carbonate in **set c**, which are

probably misclassified (Gomes *et al.*, 2015d).

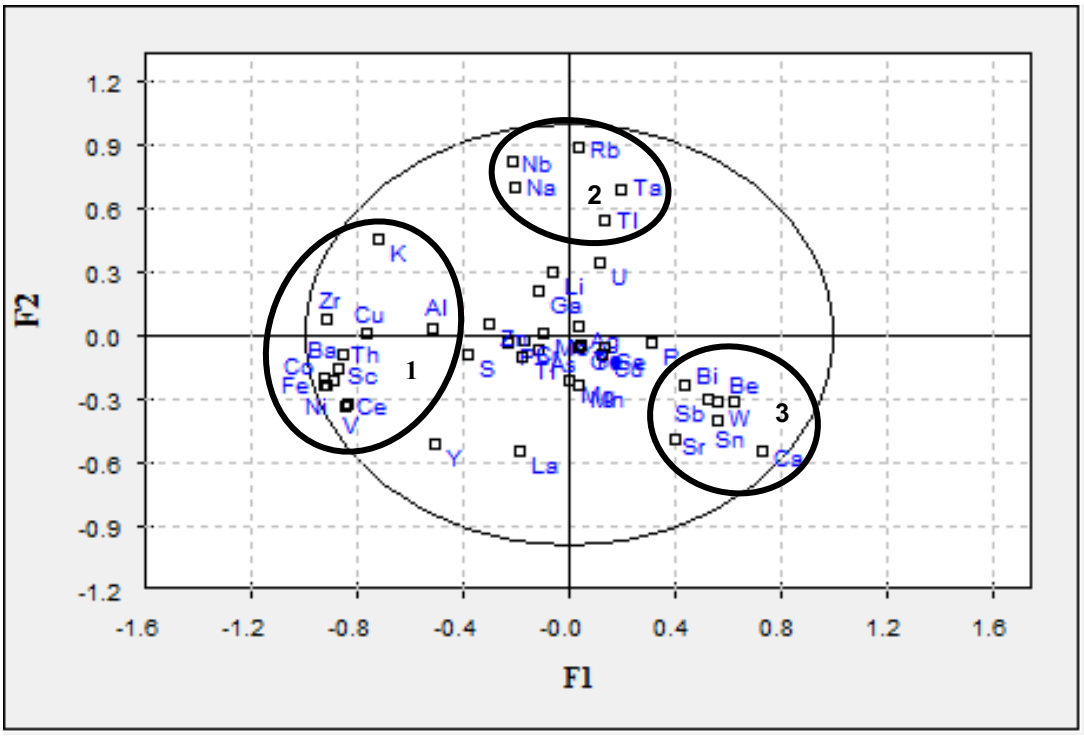

Figure 3.16 – Scatter plot of the F2/F1 overlapped with the chemical elements correlation.

Sets 1, **2**, and **3** of the scatter plot of Figure 3.16 are not similar, or in the same positions of **sets i** and **a**, **ii** and **b**, and **iii** and **c** of the scatter plots of Figures 3.17 and 3.18, respectively. However, in spite of this fact, the chemical elements of **set 1** of Figure 3.16 are associated, or can occur together with the lithologies (or lithological groups) and the hydrothermal alteration types of **sets i** and **a** of Figures 3.17 and 3.18, respectively; **sets 2** is associated, or can take place with **sets ii** and **b**; and **set 4** with **iii** and **c**. Comparing Figures 3.17 and 3.18, there is noticed that **sets ii** and **b**, and **sets iii** and **c** of both scatter plots, respectively, may take place together, or are associated, *i.e.*, the skarns and the carbonates are associated with the granites and aplites. Conversely, **sets i** and **a** cannot be associated with the last ones, that is schists are not associated with skarns and cabonates, and sericitic alteration are not associated, or do not occur with epidotite and carbonate alteration types (Gomes *et al.*, 2015d).

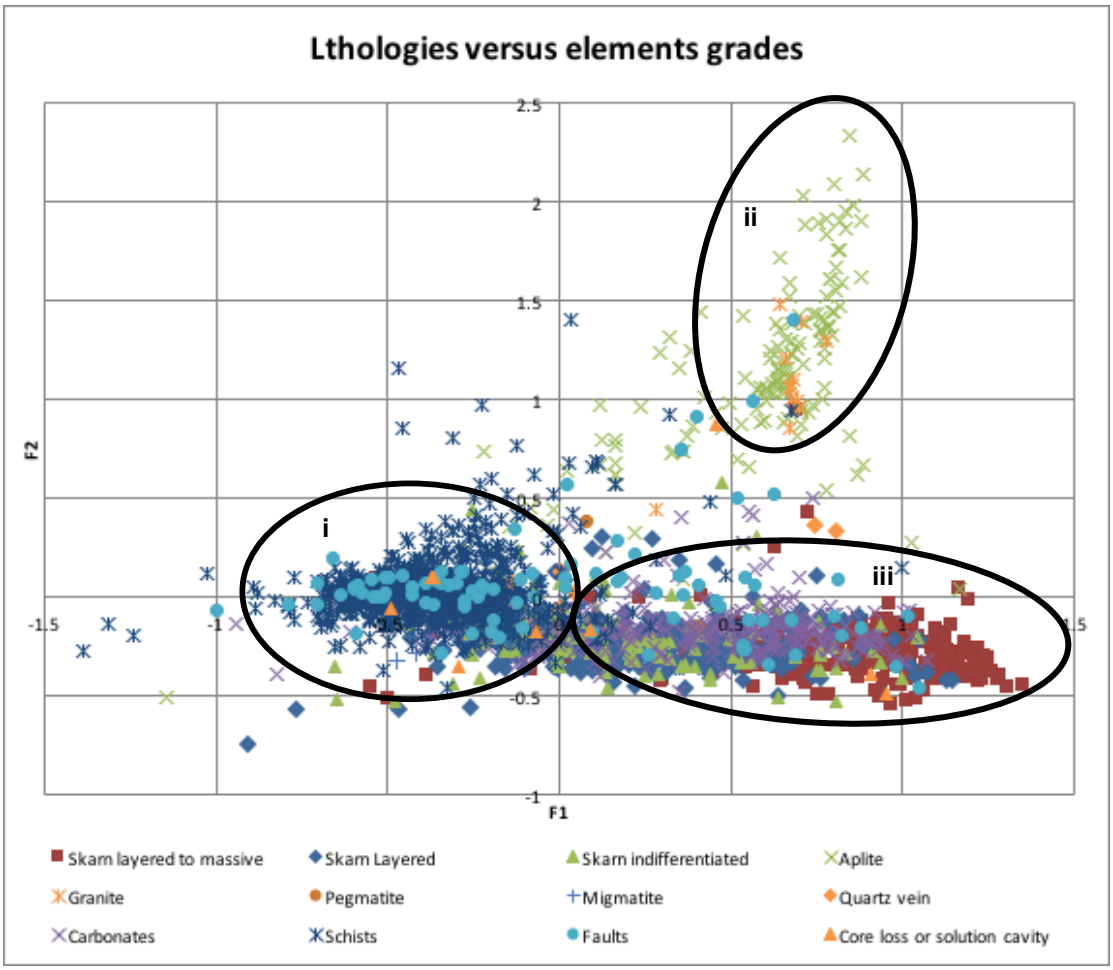

Figure 3.17 – Scatter plot of the F2/F1 overlapped with the lithologies, or lithological groups (adapted from Gomes *et al.*, 2015d).

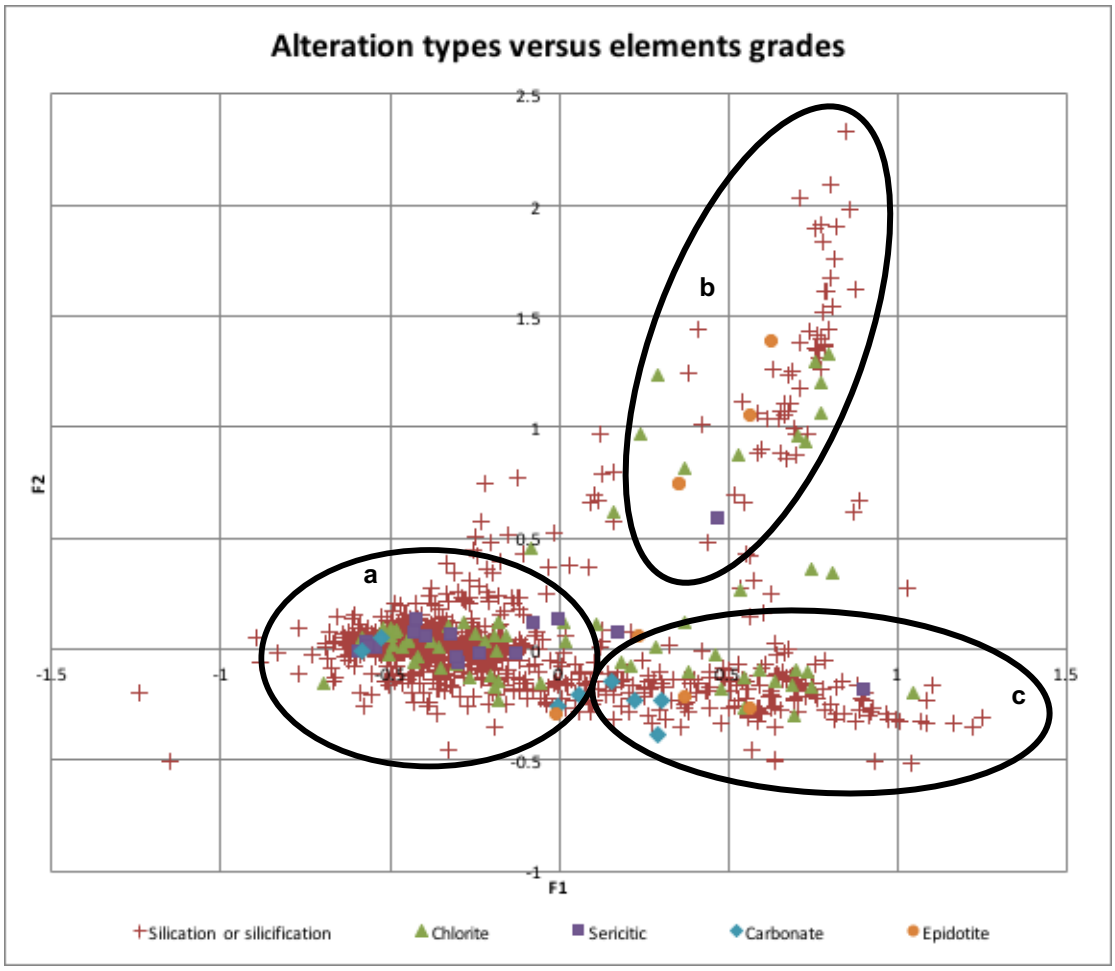

Figure 3.18 – Scatter plot of the F2/F1 overlapped with the hydrothermal alteration types (adapted from Gomes *et al.*, 2015d).

3.3.4. Discussion

The relationship of both silication or silicification, and chlorite alteration types is expected to be spread by the scatter plot, because they are probably associated with the hydrothermal alteration derived from the granitoids (mainly the granites and aplites; Pirajno, 1992) that are related with magmatic waters. Observing both Figures 3.17 and 3.18 it is possible to verify that the hydrothermal alteration types are associated, or related to the lithologies (or lithological groups), and, consequently, with their protoliths. Thus, the association of the silication or silicification with the sericitic and chlorite hydrothermal alterations has a natural speciation with the metasediments, which were initially pelites and greywackes. The association of the carbonate with the epidotite hydrothermal alterations might have a speciation with the skarns and carbonates, which initially represented the Ca carbonate bedding typically of the Lower Cambrian sequences of the Douro Group (Gomes *et al.*, 2015d).

The association between the granitoids (mostly granites and aplites) with the skarns, namely with

the skarnization process, is also expected. The clear separation between the skarns layered to massive and the other skarns (layered, and indifferentiated) may be explained by a possible involvement of local metasomatic processes on the ore massive generation in the former. Therefore, it is possible to classify the skarns layered to massive in metasomatic or ore skarns; and the skarns layered, and indifferentiated in metamorphic skarns (Kwak, 1987). The association of the Ca, W and Sn with the skarns and carbonates is also expected, because the mineralizations of W and Sn are contained in the skarns, and the skarns certainly derived from the Ca carbonate bedding, as referred above.

4. Methodology and theoretical background

This section presents the proposed methodology and all the theoretical background behind it. It is divided in three subsections: (1) state-of-the-art; (2) theoretical background; and (3) methodology. The former presents the setting of the methodology in geostatistics. In the second the theoretical background behind the case study is discussed, passing by the spatial continuity evaluation, the used algorithms and functions (kriging, object-based model, DSS, CoDSS and PFS), to the evaluation of the uncertainty of the model. Finally, the last subsection has the aim of presenting the methodology applied in the case study in three main stages: (1) a low-resolution geological model; (2) a high-resolution morphological model; and (3) a 3D W and Sn grades model.

4.1. State-of-the-art

The problem (challenge) around this study is a modelling Earth sciences one, and encompasses a set of techniques, methods and tools provided by the statistics. Therefore, and according to Caers (2011), the statistics are used to recombine and rearrange collections of data in interpretable images using a rigorous set of mathematical techniques, methods and tools. In spite of statistics traditionally neglecting both space and time, conversely the Earth sciences does not do that at all. These aspects in the Earth Sciences are always explicit in order to better understand the spatial or space-time distribution of an established natural phenomenon. Thus, the field of statistics applied to the Earth sciences is called geostatistics.

According to Soares (2006), the geostatistics is a set of statistics techniques, methods and tools with the aim of characterizing and quantifying spatial or space-time natural phenomena in models of spatial interpolation (with structural variability) and models of stochastic simulation (for uncertainty quantification). This field of statistics has risen up from the inherent difficulty of modelling geological resources, namely to understand the spatial dispersion of metal properties in the formation. The natural phenomena have two common features that have the purpose of using probabilistic models and random functions. The two features of these phenomena are: (1) they are entities with spatial distribution in a non-random way (with a certain structure); and (2) their available information, both samples and observations, is mainly parcelled, discrete and scarce (with all the associated uncertainty).

Nowadays, the geostatistics are applied to model several domains of the environment and Earth sciences (Soares, 2006). It may be applied, for instance, in the resolution of the following cases: (1) to model the morphology and/or grades of a metal or mineral deposit (Almeida *et al.*, 1993; Dimitrakopoulos, 1998; Srivastava, 2005; Charifo and Almeida, 2010; Matias, 2010; Baldé, 2012; Rodirigues, 2013; Charifo *et al.*, 2013, 2014a, b; Rodrigues and Almeida, 2014; Simões, 2014; Gomes *et al.*, 2015b, d; Matias *et al.*, 2015; Silva and Almeida, 2015a, b; Zuo *et al.*, 2015); (2) to define both an aquifer system and the maximum size of ornamental stone blocks of a quarry in

fractured massifs (Barbosa, 2012; Barbosa *et al.*, 2014; Flório, 2014, Flório and Almeida, 2015); (3) to define the hydrogeological and flux models of an aquifer (Quental, 2011; Quental *et al.*, 2012); (4) to characterize and model the dispersion of contaminants in soils or waters of a contaminated site (Carvalho, 2011; Roxo, 2011; Gomes *et al.*, 2015a); and (5) to define the morphology of oil and gas reservoirs (Almeida, 2010; Horta *et al.*, 2010; McHargue *et al.*, 2011; Kuznetsova, 2012; Quininha, 2015; Quininha, *et al.*, 2015; Marques *et al.*, 2015).

In order to quantify the characteristics of a spatial or space-time natural phenomenon it is necessary first to build models of it. These models allow us to deduce quantities of those phenomenon in unsampled or undersampled regions from the available information (Soares, 2006), and they can be of two types: (1) deterministic models that are produced by deterministic or estimation methods; and (2) stochastic models that are originated by stochastic or simulation methods. The first models have the aim of showing the complete characterization of a phenomenon through its variables and parameters (Soares, 2006), honouring locally the data and being locally more accurate. They build a single average (smooth) solution, overestimating the smaller values and underestimating the higher values, which intend to be physically realistic (Caers, 2011). Thus, as an advantage, they are unbiased with minimal quadratic error (Rossi and Deutsch, 2014), being the BLUE (Caers, 2011). However, the deterministic models and tools present the following disadvantages: (1) the models are generated only with geometric criteria, which can be contradictory with the spatial structure of the estimated quantity (Soares, 2006); (2) the models do not give uncertainty quantities related to the phenomenon because, as deterministic, they have only one solution (Soares, 2006); and (3) the estimation methods, such as the kriging tools This tools produce unrealistic smooth solutions and provide an indicator of uncertainty (kriging variance), however this measure of uncertainty is only dependent of the sample geometry and variograms, thus it is an non-complete measure and do not allow the propagation of the uncertainty (Heuvelink, 1998, *in* Goovaerts, 2002). Whilst the stochastic models may have numerous alternative solutions because the sampled data is handled as originated from a random process or as uncertain (Soares, 2006; Caers, 2011). They also honour the local data, but reproduce the histogram and the spatial variability of the phenomenon without smoothing effects, *i.e.*, preserving the extreme values. Despite the data being considered as originated from a random process it does not mean that the phenomenon itself results from a random process. It provides a method for spatial inference or quantities estimation in unsampled or undersampled areas and for the uncertainty quantification (Soares, 2006). Hence, the stochastic methods may generate several solutions with the same probability of occurrence, allowing an evaluation of the uncertainty (Goovaerts, 2002; Rossi and Deutsch, 2014). Therefore, and according to all these aspects, António Brotas (Soares, 2006) has said that "(…) a «good model» is a model that starts «by not being bad» and then gives good results".

The generation of a 3D model of any ore deposit traditionally involves the construction of two submodels (Baldé, 2012; Charifo *et al.*, 2013; Simões, 2014; Gomes *et al.*, 2015b): (1) a morphological model; and (2) a model of interest properties. The morphological model does not

only intend to characterize the shape and boundaries of the deposit (contacts between the ore bodies and the host rock), but also the geological units and/or the ore types. This model usually began with a model of lower resolution to define and characterize the shape of the boundaries of the deposit, and may pass to a model of higher resolution to provide a better base for the model of properties. In turn, the model of properties contains more detailed information about the morphology, such as the grades included in the geology.

The construction of the morphological model and, consequently, the selection of the geostatistical tool are realized according to the expert information about the deposit itself, namely its type (Simões, 2014). Therefore, if the deposit is tabular and thick it is necessary to build two surfaces (the hanging wall and the footwall) by estimation, which may use interpolation tools, such as kriging, triangulation, inverse square distance, *etc.* (Baldé, 2012; Charifo *et al.*, 2013, 2014a, b; Rodrigues, 2013), or simulation. If the shape of the deposit is more irregular and massif its boundaries are digitalized successively in several cross-sections, and all the digitalized boundaries in cross-sections are interpolated in order to produce the 3D solid model (Almeida *et al.*, 1993). Both last cases are usually of higher resolution than the size of the grid blocks of the deposit. However, for disseminated and pretty complex deposits in which their geological features, namely the ore bodies, have much lower thicknesses, modelling their grades can be done without building any detailed geological model (Simões, 2014; Gomes *et al.*, 2015b, c), only for the global boundary.

Modelling ore deposits always have errors and uncertainty associated. These errors and uncertainty may come from various sources, such as (*ex. gr.*, Singer, 2010, *in* Zuo *et al.*, 2015; Caers, 2011; Rossi and Deutsch, 2014): (1) the incomplete knowledge about the geological processes, objects (in this case ore bodies) and inherent natural variability involved; (2) the samples because of an intrinsic heterogeneity of the sampled material; (3) the sampling process, collection and preparation, the chemical analysis, and all data managing; (4) the geological model, namely the conceptual model and the model of uncertainty, has the major impact in the resources/reserves evaluation; and (5) the chosen modelling processes, methods, or even tools, for instance variogram model, simulation algorithm, *etc.*. Hence, in order to minimize as much as possible all these associated errors and uncertainty when modelling an ore deposit it is important to add geological information, not only from the drill-holes, but also from the geologists' expert information, such as their hand-drawn cross-sections, or even information contained in them (Srivastava, 2005; Simões, 2014; Gomes *et al.*, 2015b, c). As a consequence, the main goals of the addition of geological information consist in constraining the behaviour of the model not to lead to a higher underestimation (Srivastava, 2005), and to reduce the uncertainty in unsampled or undersampled zones.

The São Pedro das Águias ore deposit, as referred in **2.2.5. Local geology**, is a lens-shaped skarn type, thus comprises a good example of an ore deposit that is complex and its ore bodies have lower resolution than the grid blocks of the model (José *et al.*, 1990; O'Donovan, 2012; Bear

and MacDougal, 2013; Gomes *et al.*, 2015b, c). Therefore, the generation of a morphological model of the present case study is a challenging task, because the lens-shaped skarns are: (1) numerous; (2) thin; (3) conditional to the geological structure (shape and orientation); and (4) recognized only in the drill-holes with unknown interconnections between them (Gomes *et al.*, 2015b, c). One possible method to create a morphological model of this kind of ore deposits is by the digitalization of their limits in cross-sections according to the intersections identified in the drill-holes and some geological assumptions. However, as referred above, this process is more indicated for larger masses than for smaller ones, and, in addition, it becomes an arduous and subjective task owing to indeterminate possibilities of interconnections between drill-holes (Simões, 2014; Gomes *et al.*, 2015b, c).

In this study a multistep methodology is proposed in order to overcome and try to solve all these problems. Therefore, an adaptation of the automatic simulation algorithm proposed by Simões (2014) was used to generate a morphological model of this deposit. Then, the morphological model is constrained by PFS to a W and Sn co-simulated grades model. The Simões (2014) algorithm was built in order to create a morphological model of the Panasqueira ore deposit (northern Portugal), whose ore bodies are also of smaller resolution than the grid blocks of the mining model. More detailed information about this methodology will be given in **4.3. Methodology**.

4.2. Theoretical background

4.2.1. Spatial continuity

The characteristics of a mineral deposit, namely its morphology and grades, demonstrate spatial continuity that is important to calculate in order to proceed to the resources evaluation and mine planning (Rossi and Deutsch, 2014). Thus, the quantification of the spatial continuity of certain ore deposit allows a better knowledge about it and enhances the prediction of the structure and grades in under or unsampled locations (Caers, 2011; Rossi and Deutsch, 2014).

The spatial continuity analysis uses structural elements to measure it, such as the two-point, circle, or line segment. For geostatistics, the two-point is the privileged structural element, owing to the understanding about some resource that comes from a set of samples or observations that are usually discrete, limited and scarce (Soares, 2006). Considering a variable $Z(x)$, the scatter-plots representing the measurements at locations x and $x+h$ ($Z(x)$ and $Z(x+h)$, respectively) where h means a vector distance are named h-scattergrams. These scattergrams are a tool to evaluate the spatial continuity of the variable $Z(x)$ (Soares, 2006), however they are not straightforward.

The spatial continuity of a variable $Z(x)$ may be quantified by different estimators, for example, the variogram, covariance, or the correlogram (Soares, 2006). The estimator that is usually used is the variogram. The variogram is considered a statistical metric and is estimated by the squared

difference between two separated values by a distance vector h (Soares, 2006; Caers, 2011; Rossi and Deutsch, 2014):

$$\gamma(h) = \frac{1}{2N(h)} \sum_{\alpha=1}^{N(h)} [Z(x_\alpha) - Z(x_\alpha + h)]$$

$N(h)$ is the number of pairs of points separated by h. This analysis may be realized for several directions of h, making an evaluation by direction.

After the calculation of the variogram, it is necessary to fit a representative function, in order to synthetize the structural features of the deposit in a unique and coherent variogram model. Therefore, the adjustment of the variogram by a theoretical model is normally conditional to the expert knowledge about the deposit itself. The theoretical models are always positively defined functions, and the most commonly used are: (1) spherical; (2) exponential; or (3) Gaussian (Soares, 2006). These theoretical models are also defined by the following parameters (Figure 4.1; Soares, 2006; Caers, 2011; Rossi and Deutsch, 2014): (1) the sill is the upper limit where the variogram $\gamma(h)$ tend to, with the increase of the values of h; (2) range a is the distance where h the values of the variogram $\gamma(h)$ stop increasing, and are equal to a sill that is usually coincident with the variance; and (3) the nugget effect C_0 is the value of the variogram $\gamma(h)$ at $h = 0$ is exactly zero, but for a small h a sudden jump in the variogram $\gamma(h)$ is observed, owing to the variability at a small scale uncovered by samples, and at the scale of the sample induced by unsystematic errors of sampling and motorization (adding a random noise to the structure).

The spherical model is presented by the following theoretical model:

$$\gamma(h) = \begin{cases} C\left[\frac{3h}{2a} - \frac{1}{2}\left(\frac{h}{a}\right)^3\right], h \leq a \\ C, h > a \end{cases}$$

Certain phenomena, such as the lens-shaped skarns, may demonstrate to be more continuous in a particular direction (Soares, 2006). The lens-shaped skarns have a greater continuity in the direction parallel with their axis of higher expression, in contrast with the perpendicular direction. This kind of structure is named anisotropic, but when the variogram presents the same behaviour in all directions of the space it is called isotropic.

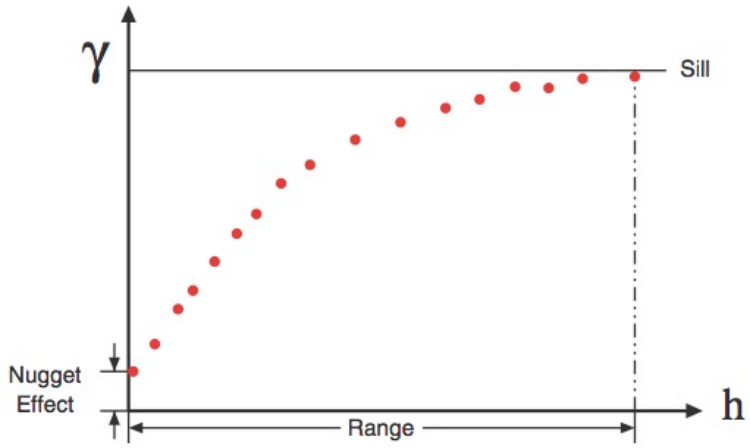

Figure 4.1 – Overview of a variogram and respective parameters (Rossi and Deutsch, 2014).

4.2.2. Kriging tools

Matheron (1965, *in* Soares, 2006) was the first author who denominated kriging to the geostatistical estimator, in memory to the first works of Krige (1951, *in* Soares, 2006). The kriging is a deterministic set of methods that provide a unique solution without measures of uncertainty and ignore the measures of structural continuity, for instance the variogram of a natural resource (Soares, 2006). As referred in **4.1. State-of-the-art**, they are the BLUE owing to (Caers, 2011): (1) B of best estimator (E), because the aim is the estimation of the unknown values at the unsampled places; (2) L of linear estimator, owing to the average squared error between the true and the estimated value is as small as possible; and (3) U of unbiased estimator, because if the kriging is repeated as many times as possible, on average, the errors that are made will be close to zero.

The kriging system of equations is solved in order to extract the weights that minimize both the error and the variance of the error (Rossi and Deutsch, 2014). These weights λ_α synthetize two important extreme effects of the spatial inference process (Soares, 2006; Rossi and Deutsch, 2014): (1) to reflect the highest or smallest structural proximity of the samples $Z(x_\alpha)$ in relation to point $Z(x_0)$ that will be estimated; and, simultaneously, (2) to have the divisive effect of eventual clusters of samples, in order to avoid skewing. There are many kriging variants of estimators that are possible to use according to the goal of the work, for instance OK, SK, KED, IK, *etc.* (Soares, 2006; Caers, 2011; Rossi and Deutsch, 2014). The SK, OK and KED (applied with OK) were used.

The SK algorithm was used to estimate the means and the variances of the W grades distribution laws within the DSS algorithm to model the grades. The application of the SK algorithm implies the knowledge of the local means (as a constant) of the random variables (Soares, 2006; Rossi and Deutsch, 2014). This kriging algorithm also minimizes the error variance with no constraints to the weights (Rossi and Deutsch, 2014). The SK estimator is the following (Soares, 2006):

$$[Z(x_0)]^* - m(x_0) = \sum_{\alpha=1}^{N} \lambda_\alpha [Z(x_\alpha) - m(x_\alpha)]$$

The value $Z(x_0) - m(x_0)$ is estimated based on those of the samples $Z(x_\alpha) - m(x_\alpha)$, $\alpha = 1, \dots, N$, being N the neighbouring variables. The error variance $\varepsilon(x_0) = [Z(x_0)]^* - Z(x_0)$ may be expressed in function of covariances as:

$$Var\{\varepsilon(x_0)\} = C(0) + \sum_\alpha \sum_\beta \lambda_\alpha \lambda_\beta C(x_\alpha, x_\beta) - 2\sum_\alpha \lambda_\alpha C(x_\alpha, x_0)$$

Finally, the stationary version of the SK equation, if the mean is stationary $m(x_\alpha) = m$, $\alpha = 1, \dots, N$, is the following:

$$[Z(x_0)]^* = \sum_\alpha \lambda_\alpha Z(x_\alpha) + \left[1 - \sum_{\alpha=1}^{N} \lambda_\alpha\right] m$$

Passing to the OK, it was used in order to quantify the equivalent resources of the São Pedro das Águias ore deposit to compare with the resources resulted from the application of the methodology. The OK concerns about the minimum error linear variance estimated at a location where the true values are unknown, *i.e.*, in contrast with SK the local means are not known, because it constrains the sum of the weights to be 1. The OK estimator is given by (Soares, 2006):

$$[Z(x_0)]^* = \sum_{\alpha=1}^{N} \lambda_\alpha \, Z(x_\alpha)$$

This estimator is a linear combination of the set of N of $x_0 - Z(x_\alpha)$, $\alpha = 1, \dots, N$, is unbiased ($E\{\varepsilon(x_0\} = 0$) and the estimation variance is minimal ($min\{Var[\varepsilon(x_0)]\}$), both in relation to the error $\varepsilon(x_0) = [Z(x_0)]^* - Z(x_0)$. The OK variance stays:

$$Var\{\varepsilon(x_0)\} = C(0) + \sum_\alpha \sum_\beta \lambda_\alpha \lambda_\beta C(x_\alpha, x_\beta) - 2\sum_\alpha \lambda_\alpha C(x_\alpha, x_0) + 2\mu\left[\sum_\alpha \lambda_\alpha - 1\right]$$

Being $2\mu[\sum_\alpha \lambda_\alpha - 1] = 0$. Thus, the OK system of $N + 1$ equations, in which its solution gives N weights λ_α, is the following:

$$\begin{cases} \sum_\beta \lambda_\beta C(x_\alpha, x_\beta) + \mu = C(x_\alpha, x_0) \\ \sum_\alpha \lambda_\alpha = 1 \end{cases}, \alpha = 1, \dots, N$$

Finally, KED was used in the automatic algorithm proposed by Simões (2014) to estimate the local intensity of the lens-shaped skarns. KED uses an external or secondary variable that defines at each location a linear function (Rossi and Deutsch, 2014). In other words, according to Marechal (1984, *in* Soares, 2006) it is considered an external drift $m(x)$ as a linear function of an auxiliary external variable $Y(x)$:

$$m(x) = a_0 + a_1 Y(x)$$

Both a_0 and a_1 are also estimated with $Z(x)$, but $m(x_0)$ is known in any point of x_0 through the external drift $Y(x)$. Therefore, its estimator conditioned to $\sum_\alpha \lambda_\alpha m(x_\alpha) = m(x_0)$ stays:

$$[Z(x_0)]^* = \sum_{\alpha=1}^{N} \lambda_\alpha Z(x_\alpha)$$

Then, the weights λ_α have the following constraints:

$$[Z(x_0)]^* = \sum_{\alpha=1}^{N} \lambda_\alpha Z(x_\alpha)$$
$$\sum_{\alpha} \lambda_\alpha = 1$$

The estimation variance may be written in function of the covariances $C_R(h)$ of the residuals $R(x)$:

$$E\{[[R(x_0)]^* - R(x_0)]^2\} + 2\mu_0[\sum_\alpha \lambda_\alpha - 1] + 2\mu_1[\sum_\alpha \lambda_\alpha Y(x_\alpha) - Y(x_0)]$$

Hence, the weights λ_α are obtained by the following system of $N + 2$ linear equations:

$$\begin{cases} \sum_{\beta=1}^{N} \lambda_\beta C_R(x_\alpha, x_\beta) + \mu_0 + \mu_1 Y(x_\alpha) = C_R(x_\alpha, x_0), \alpha = 1, \dots, N \\ \sum_{\beta}^{N} \lambda_\beta = 1 \\ \sum_{\beta}^{N} \lambda_\beta Y(x_\beta) = Y(x_0) \end{cases}$$

The collocated SCoK was used to estimate the local mean and the local variance within the CoDSS algorithm. In the co-kriging system of equations, the values of the secondary variable are added to the neighborhood selected data to estimate the value in each location of the primary variable taking into account a second variable. In the case of the collocated co-kriging the secondary variable is used only in the exact location to estimate (Soares, 2001; Rossi and Deutsch, 2014). It is important to remark that the co-kriging approaches are useful when, beyond the primary variable, a secondary variable correlated with the primary variable exists, and it is sampled in more detail and in different locations than the primary variable.

According to Soares (2001), if two variables are considered in a case study and a secondary variable $Z_2(x)$ is known in all locations to estimate x_0, the collocated SCoK estimator of a primary $Z_1(x_0)$ in an unsampled point x_0 is:

$$[Z_1(x_0)]^* - m_1 = \sum_{\alpha=1}^{N} \lambda_\alpha(x_0)[Z_1(x_\alpha) - m_1] + \lambda_\beta(x_0)[Z_2(x_0) - m_2]$$

In the present case study the intention is to simulate two correlated variables W and Sn grades. Thus, the proposed approach simulates first by DSS the W grades, and, in a second step, the Sn grades are co-simulated using CoDSS constrained to the previous simulated W grades. This process ensures that pairs of simulated images of W and Sn are generated with an observed correlation.

4.2.3. DSS and CoDSS algorithms

The DSS method is a simulation algorithm that allows obtaining sets of equiprobable or equally

representative images of a studied phenomenon without any transformation of the original variable. This is a clear advantage when comparing with the SGS algorithms, because it avoids any transformation of the original variable. The SGS algorithm needs to transform it in a Gaussian variable that, when the histogram is asymmetrical, makes the variograms of the original variable having difficult reproduction (Soares, 2006).

This particularity of the DSS turns it in the most common and popular stochastic algorithm used in the Earth sciences to reproduce the spatial distribution and to evaluate the uncertainty of resources (Soares, 2001). Therefore, according with Rossi and Deutsch (2014), the use of this algorithm includes the following advantages: (1) reproduction of the variogram in original units; (2) dealing with variables that do not average linearly after the normal score transformation; and (3) the maximum entropy characteristic of the Gaussian distribution. The DSS algorithm was used to simulate the W grades of the deposit as primary variable.

According to Soares (2001, 2006), the goal of the DSS is to reproduce the global CDF $F_Z(z) = P\{Z(x) < z\}$ and the stationary variogram $\gamma(h)$ of the continuous variable $Z(x)$ in the simulated images. It is based on the assumption that the local distribution laws of $Z(x)$ are centred in the SK estimator:

$$[Z(x_0)]^* - m(x_0) = \sum_{\alpha=1}^{N} \lambda_\alpha [Z(x_\alpha) - m(x_\alpha)]$$

The conditional local variance is equal to the kriging variance $\sigma^2(x_0)$, hence the spatial co-variances or variogram are necessarily reproduced in the simulated images (Journel, 1994, *in* Soares, 2006). However, this assumption only ensures the variogram reproduction of the original variable. To ensure the histogram as well, Soares (2001) used the local means and variances to re-sample the global distribution laws, instead of defining the local distribution laws with the SGS. So, there are chosen intervals of $Z(x)$ of the global distribution law $F_Z(z)$ to create a function $F'_Z(z)$ and the simulated values $Z^s(x_0)$ are sampled from $F'_Z(z)$.

The local mean estimated by the SK estimator centres the intervals of the function $F'_Z(z)$. The intervals also have proportional amplitude to the conditional variance of the SK variance estimation. These intervals may be defined by the selection of a subset of n adjacent values $z(x_i)$ of the global experimental histogram. The mean and variance of the selected subset need to be equal to the SK estimator of the local mean $[Z(x_0)]^*$ and to the estimation variance, respectively:

$$\frac{1}{n}\sum_{i=1}^{n} [z(x_i) - [z(x_i)]^*]^2 = \sigma^2(x_0)$$

$$\frac{1}{n}\sum_{i=1}^{n} z(x_i) = [z(x_i)]^*$$

In turn, the CoDSS algorithm is an extension of the principle of sequential simulation applied to the full random fields. It is used when there are two or more variables spatially dependent or correlated. Consequently, the simulation should reproduce not only the distributions and the individual variograms, but also the correlation between the variables. In particular, the values of

the variables should be generated from a joint simulation or co-simulation (Soares, 2006). Therefore, the CoDSS was used in this study to co-simulate the Sn grades, as a secondary variable, constrained to the previously simulated W grades.

The process of co-simulation may be performed with SGS, SIS or DSS. However, the main advantage of the CoDSS algorithm is that it enables the realization of a joint simulation handling directly with the original variable (Soares, 2001, 2006). So, each variable is simulated conditioned to the previously simulated one, in place of simulating N_v variables simultaneously (Goovaerts, 1997, *in* Soares, 2001). Consequently, according to Soares (2006), admitting N_v variables $Z_1(x), \dots, Z_{N_v}(x)$ intended to be co-simulated, the relation of the simulation of joint distribution processes stays:

$$F\left(Z_1, Z_2, \dots, Z_{N_v}\right) = F(Z_1)F(Z_2|Z_1)\cdots F(Z_{N_v}|Z_1, \dots, Z_{N_{v-1}})$$

$Z_1^s(x_i)$ are previous simulated values of $Z_1(x)$, and $Z_1(x_\alpha)$ the experimental values and the values eventually already simulated of $Z_2(x)$ in turn of x_0. After the use of the DSS algorithm and the acquisition of the images of $Z_1(x)$, the same algorithm is applied to $Z_2(x)$ assuming an image of $Z_1(x)$ as a secondary one with spatial correlation between $Z_1(x)$ and $Z_2(x)$ characterized by the correlogram $\rho_{1,2}(h)$. Then, the $Z_2(x)$ values are computed from the CDF in any spatial location of x_0 to the values $Z_2(x)$ and $Z_1(x)$ simulated before. The CDF are created to any x_0 location from the means and local variances that are calculated by co-estimation of $Z_2(x_0)$ based on the values of $Z_2(x_\alpha)$, $Z_1^s(x_i)$, $i = 1, \dots, N$, and stays:

$$F_z[Z_2(x_0)|Z_2(x_\alpha)] = z_2(x_\alpha),\ Z_1(x) = z_1^s(x_i), i = 1, \dots, N$$

Finally, attending the initially simulated variables $Z_1(x)$, the mean $[Z_2(x_0)]^*$ and the local variances are computed using a version of the estimator of the co-located simple co-kriging, in which there is a linear combination of the selected values $z_2(x_\alpha)$ in turn of x_0 and the known value $z_1^s(x_i)$:

$$[z_2(x_0)]^* - m_2 = \sum_{\alpha=1}^{N} \lambda_\alpha [z_2(x_\alpha) - m_2] + \lambda_\beta [z_1^s(x_0) - m_1]$$

4.2.4. PFS algorithm

The PFS algorithm is a simulation technique that generates equiprobable realizations of both categorical and continuous variables, matching both the available data, and the distribution and spatial continuity of the property being modelled (Froidevaux, 1992; Srivastava, 1992, *in* Almeida, 2010). This method is often used when local distribution functions of the variable are available (Froidevaux, 1992).

But the PFS algorithm has disadvantages: (1) it does not guarantee a fair reproduction of the target statistics (histogram and variogram; Goovaerts, 2002); (2) the production of larger spaces of uncertainty (Goovaerts, 1999, *in* Goovaerts, 2002); and (3) the creation of artificial discontinuities

around the data by the use of non-conditional p-fields (Srivastava, 1992, *in* Goovaerts, 2002). Its advantages are: (1) the use of CCDFs may lead to a better reproduction of the histogram and variogram and a more precise distribution of the response values (Goovaerts, 2002); (2) a method that allows a simple integration of scarce data with exhaustive soft data (Froidevaux, 1992); (3) flexibility to incorporate dense secondary data, such as external geological information (Almeida, 2010); (4) theoretically it is a simple tool (Froidevaux, 1992; Almeida, 2010); and (5) it is faster generating a large number of conditional realizations than SIS owing to the CCDFs that only have to be simulated once (Goovaerts, 2002).

According to Almeida (2010), in order to use the PFS algorithm first is necessary to build the (know) local probability distribution of the variable under study $F_Z(x_0)$. Afterwards, for each realization it is necessary to construct a simulated probability field $P(x)$, assuming that the variogram γ_{Z_k} is representative of the $F_Z(x_0)$ continuity within each class c. Finally, the simulated value $Z_s(x_0)$ is generated by Monte Carlo simulation, being equal to:

$$Z_s = F_Z^{-1}(x_0, \rho)$$

In which $p = P(x_0)$. As a consequence, attending to Froidevaux (1992), the PFS algorithm has the following issues: (1) the local PDFs are available and, when built, are realistic; and (2) the univariate and bivariate characteristics of $P(x)$ may be inferred.

4.2.5. Object-based model algorithm

According to Caers (2011), an object-based model intends to represent the shape of objects as realistically as possible. In other words and still regarding the same author, the objective of an algorithm that produces such models is to create several ones of the natural objects that are being modelled in a way that they are in agreement with the data.

As referred in **4.1. State-of-the-art**, the generation of a morphological model of the São Pedro das Águias skarn deposit is a challenging task, because the lens-shaped skarns are: (1) numerous; (2) thin; (3) conditional to the geological structure (shape and orientation); and (4) recognized only in the drill-holes with unknown interconnections (Gomes *et al.*, 2015b, c). Therefore, in order to overtake these issues, an improved version of the 2D object-based model algorithm of automatic simulation proposed by Simões (2014) was used. The author's algorithm was initially written in Visual Basic language, however for the present study it was written in C language, in order to make a faster calculation (Simões, 2014).

This algorithm runs in several 2D cross-sections, and uses the local intensity of the lens-shaped skarns for the entire model also previously evaluated, which is calculated by the number of intersections found in each block of a low-resolution auxiliary grid (Figure 4.2 a; Simões, 2014). These steps will be better explained in this section.

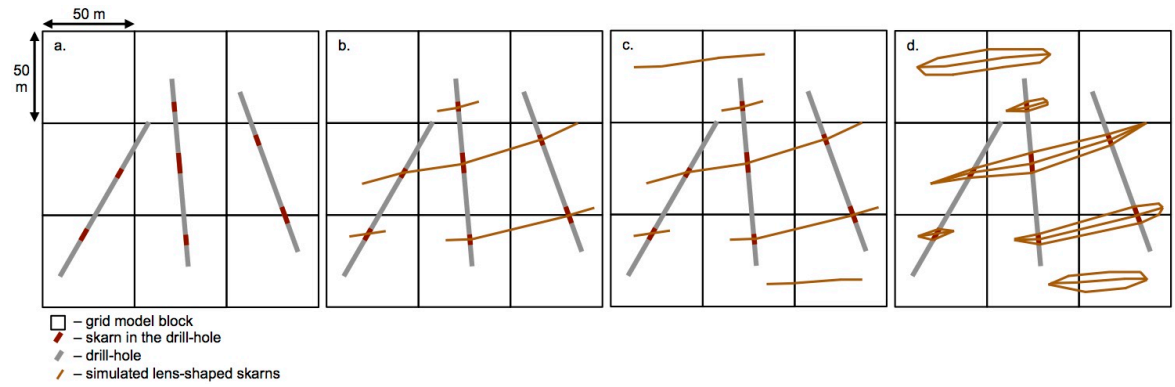

Figure 4.2 – Schematic cross-section view plan of the object-based model algorithm steps: (a) identification of the skarn lithologies in the drill-holes; (b) generation of the lens-shaped skarns in form of polylines; (c) addition of hypothetical lens-shaped skarns regarding the local and global target intensities; and (d) addition of local thicknesses (adapted from Simões, 2014, *in* Gomes *et al.*, 2015b, c).

To generate the lens-shaped skarns, the 2D object-based model algorithm utilized involves the following steps for each cross-section (Figure 4.2; Simões, 2014; Gomes *et al.*, 2015b, c):

(1) Detection of the drill-holes associated with the cross-section. The drill-holes are splited in skarn ρ_{SK} (lens-shaped skarns) and no-skarn ρ_{NSK} lithologies (Figure 4.2 a), and the lens-shaped skarn centre of gravity recognized in the drill-holes is computive:

$$x_{SK}; y_{SK}; z_{SK}$$

(2) Identification of all possible connections between the lens-shaped skarn centres of gravity, so long as they are according with the geological structure. The geologists' hand-drawn cross-sections are used to take the measures and are divided at most into two regions by each one, according to the predominant inclination of the lens-shaped skarns (Figure 4.3). Afterwards, the dip angles between the drill-holes and the geologists' delineated lens-shaped skarns are measured with the horizontal (Figure 4.3). The main dip angle of each region is then generated by a Monte Carlo simulation in a distribution law, regarding its measures. Consequently, the inclination of the polylines is constrained by this geological structure statement;

(3) Random selection of successive admissible connections followed by generation of the lens-shaped skarns as polylines. In the cases that the polylines have no drill-hole to connect, the length and the inclination of the polyline are randomly generated according with a chosen distance and the last geological structure statement (Figure 4.2 b);

(4) Evaluation of both global intensity of skarns $I_{SK_{ijk}}^{Model}$ (number of polylines of the entire model) and local intensity of skarns $I_{SK_{ijk}}^{KED}$ (number of polylines of each block) estimated by KED to compute both the local D_{ijk} and global D_G deviations between the simulated scenario and the target intensity:

$$D_{ijk} = I_{SK_{ijk}}^{Model} - I_{SK_{ijk}}^{KED}$$

$$D_G = \sum_i \sum_j \sum_k D_{ijk}$$

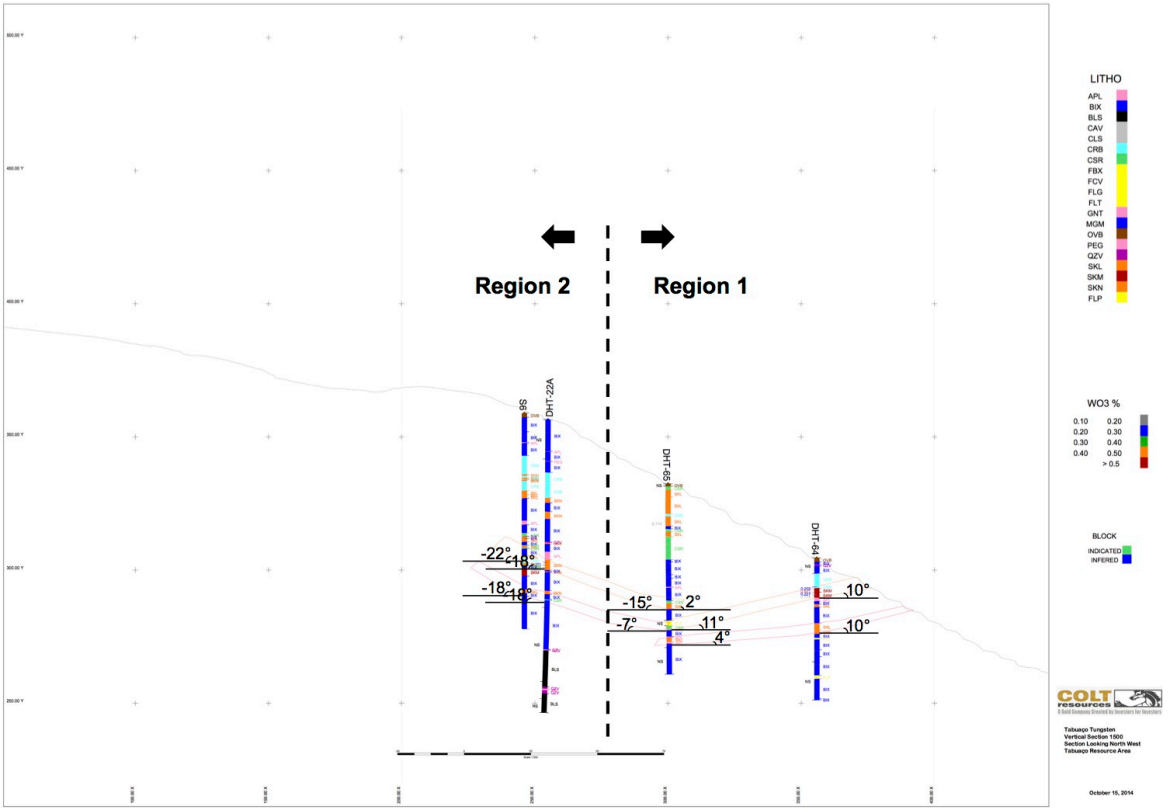

Figure 4.3 – Example of a geologists' hand drawn cross-section divided in two regions, and insterpreted dip angles of the structure (adapted from Colt, 2014).

(5) If the deviations are positive is because the model intensity of skarns is superior to the target intensity, and that does not occur if the simulation of the polylines uses only the intersections of drill-holes. if they are negative, which is usual for the first iteration, it is necessary to simulate more hypothetical polylines not recognized in the drill-holes. Thus, this process is realized iteration by iteration until an acceptable deviation of the intensity of skarns is achieved (Figure 4.2 c);

(6) Finally, thicknesses are assigned to the polylines in order to define the skarn geobodies, that are, the lens-shaped skarns (Figure 4.2 d). If the polylines are intersected with the drill-holes, they get the true values of the lens-shaped skarns; however, if not, *i.e.*, if they are simulated, the thicknesses are generated by Monte Carlo simulation from the thicknesses global CCDF.

4.2.6. Uncertainty evaluation

When modelling any phenomenon, including ore deposits (the case study itself), it has associated

errors and uncertainty that may come from various sources, as referred in **3.1. State-of-the-art**. These errors and uncertainty will constrain the behaviour of the variables being modelled (Soares, 2006), and, consequently, of the model itself. Therefore, Caers (2011) referred that the uncertainty is considered the incomplete knowledge about a phenomenon that is intended to quantify. The same author also noted that there is no true uncertainty, and that there are only models of it, because it is not possible to know exactly if a quantification of uncertainty is either correct or the best as possible. As a consequence and also stated in **3.1. State-of-the-art**, the best way of obtaining and quantifying the uncertainty is by the use of the stochastic simulation tools, in order to produce a set of images equally representative (Soares, 2006; Rossi and Deutsch, 2014).

4.3. Methodology

The suggested methodology is displayed in the fluxogram of Figure 4.4, and, as referred before, comprises three main stages (Gomes *et al.*, 2015b): (1) building of a low-resolution geological model; (2) building of a high-resolution morphological model; and (3) building of a W and Sn grades model.

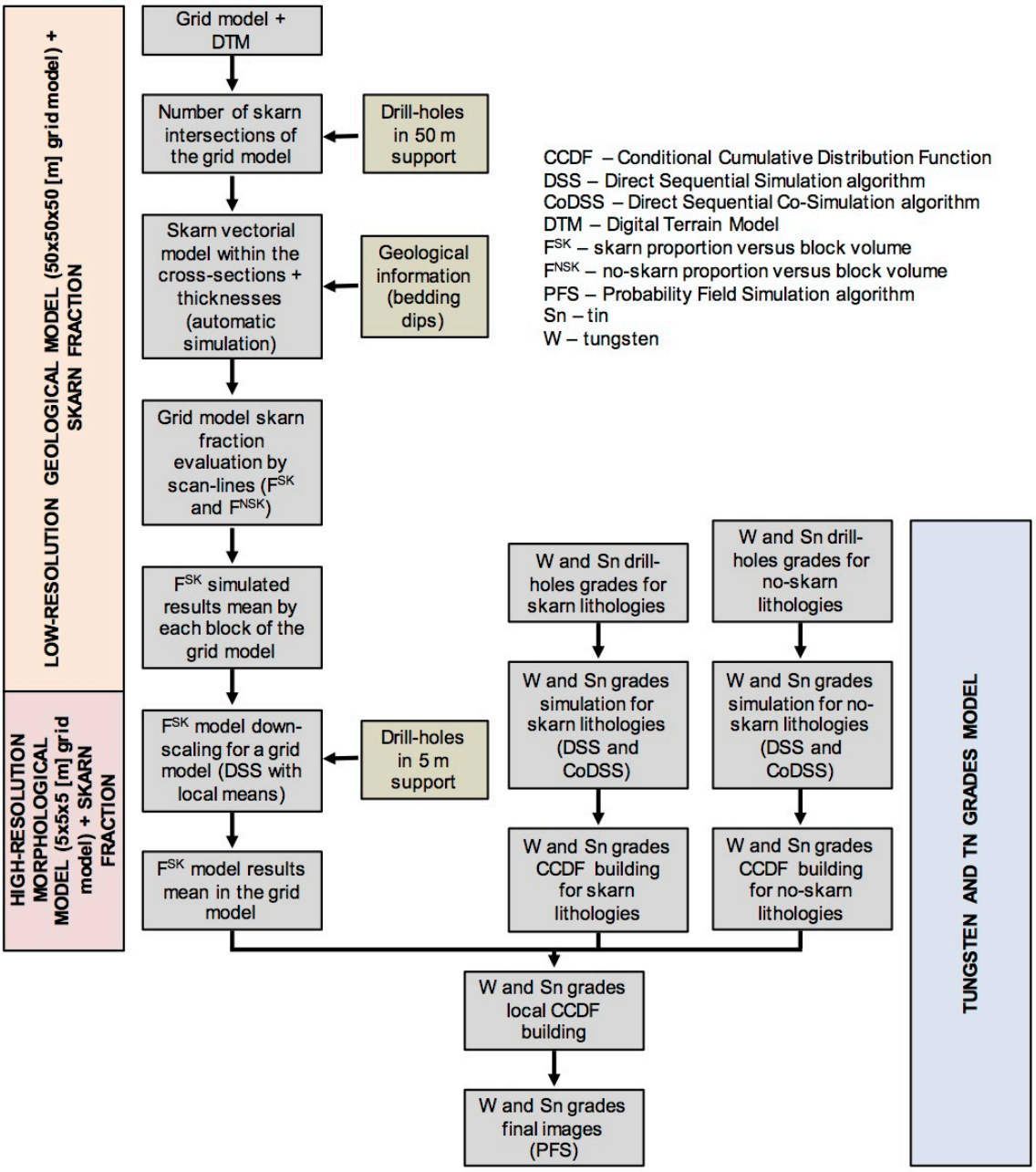

Figure 4.4 – Fluxogram representing the methodology applied on the study (Gomes *et al.*, 2015b).

4.3.1. Low-resolution geological model

The first stage starts with the construction of a low-resolution grid, covering the entire volume of the deposit. The dimensions of the blocks should be large enough to ensure that most of them include drill-holes and only for a few is necessary to estimate the number of lens-shaped skarns intersections. Hence, this low-resolution mesh of blocks has two objectives: (1) to localize the cross-sections where the skarn geobodies will be generated; and (2) to impose locally the lens-shaped skarns intensity, that is, the number of lens-shaped skarns intersected by the drill-holes. After this preliminary step, the number of intersections of the lens-shaped skarns is calculated, and

then their local intensity is evaluated for the entire model.

The following step consists in the application of the 2D object-based model algorithm proposed by Simões (2014) in order to generate the lens-shaped skarns as geobodies by each cross-section. The operation of the 2D object-based model algorithm is presented in the last subsection, more exactly in **3.2.3. Object-based model algorithm**. Finally, this step is finished with the evaluation of the skarn and no-skarn relative proportion as variables (F^{SK} and F^{NSK}, respectively). The F^{SK} and F^{NSK} are calculated by sampling lines or scan-lines in each block of the mesh and for each geological scenario resulted from the 2D object-based model algorithm. The F^{SK} local partial results are then averaged to pass to the next stage.

4.3.2. High-resolution morphological model

The second stage of this methodology is characterized by the creation of a morphological model of higher resolution by mapping the F^{SK} variable for the high-resolution grid of the mine. The high-resolution morphological model is generated by a downscalling procedure using a conditional simulation process between the drill-hole data and the low-resolution geological model. For that, the DSS algorithm with local means, which generates the simulated values at 3D between the cross-sections, is used. Finally, the simulated realizations of the F^{SK} are then averaged in order to move to the next and last stage.

4.3.3. W and Sn grades model

Finally, the final stage includes the generation of a W and Sn grades model, that is, an ore properties model, conditional to the morphological model previously created. This stage is developed into two different branches that are simulated separately: (1) one for the skarn lithologies; and (2) another for the remaining lithologies, *i.e.*, no-skarn ones. The former contains: (1) skarns layered to massive; (2) skarns layered; and (3) skarns indifferentiated. The latter includes: (1) aplites; (2) granites; (3) pegmatites; (3) migmatites; (4) quartz veins; (5) biotite schists; (6) black/dark-grey schists; (7) carbonates or calcschists; (8) calcsilicate lithologies or poorly developed skarns; (9) calcite veins; (10) faults breccia; (11) faults filled with gauge; (12) probable faults; (13) obvious faults; (14) overburden; (15) solution cavities; and (16) core losses. On the other hand, each branch is divided into two sets of data: (1) the W grades; and (2) the Sn grades. The W grades are simulated and the Sn ones co-generated according to the first results of W grades.

To develop this stage, it is necessary to separate the drill-hole data in four different sets, that is, skarn and no-skarn lithologies (Figure 4.5), and W and Sn grades. Supposedly, only the skarn lithologies should contain metal grades, however some cores of the remaining ones also report grades. This fact probably happens owing to human error when observing and measuring

geological features, or collecting, interpreting and working the data. Therefore, it is for this reason that the no-skarn lithologies are also simulated in a different branch of this stage of the methodology. As the W and Sn elements have moderate linear correlation, they may be simulated by a co-simulation procedure. Thus, for both skarn and no-skarn lithologies, the W grades are simulated first using the DSS algorithm (because it is the most important element, economically speaking), and then, the Sn grades are co-simulated with the CoDSS algorithm conditional to the previously simulated W grades.

Figure 4.5 shows how the drill-hole cores were divided in skarn and no-skarn lithologies, independently of the existent grades, in order to produce both branches of the W and Sn grades model. After splitting the drill-hole lithologies in skarn and no-skarn lithologies, the W or Sn grades are calculated according to with the following equation:

$$gr_{DH}^{W/Sn} = \frac{gr_1^{SK/NSK} l_1 F_1^{SK/NSK} + gr_2^{SK/NSK} l_{n_2} F_2^{SK/NSK} + \cdots + gr_n^{SK/NSK} l_n F_n^{SK/NSK}}{l_1 F_1^{SK/NSK} + l_2 F_2^{SK/NSK} + \cdots + l_n F_n^{SK/NSK}}$$

$$gr_{DH}^{W/Sn} = \frac{gr_1^{SK/NSK} l_1 F_1^{SK/NSK} + gr_2^{SK/NSK} l_2 F_2^{SK/NSK} + \cdots + gr_n^{SK/NSK} l_n F_n^{SK/NSK}}{l_1 F_1^{SK/NSK} + l_2 F_2^{SK/NSK} + \cdots + l_n F_n^{SK/NSK}}$$

l_n corresponds to the length of n part of a drill-hole, and $F_n^{SK/NSK}$ to the skarn or no-skarn relative proportions of n part of a drill-hole.

Afterwards, also for both branches, the CCDFs of the W and Sn grades are built for each block of the grid and the W and Sn simulated results are taken in order to move to the final step of the methodology. Then, W and Sn CCDFs are newly created for each grid block of the mesh, but conditional to the grades images of the previously simulated morphological model, *i.e.*, to the F^{SK} results. Finally, the PFS algorithm is applied to both W and Sn CCDFs to generate the final realizations.

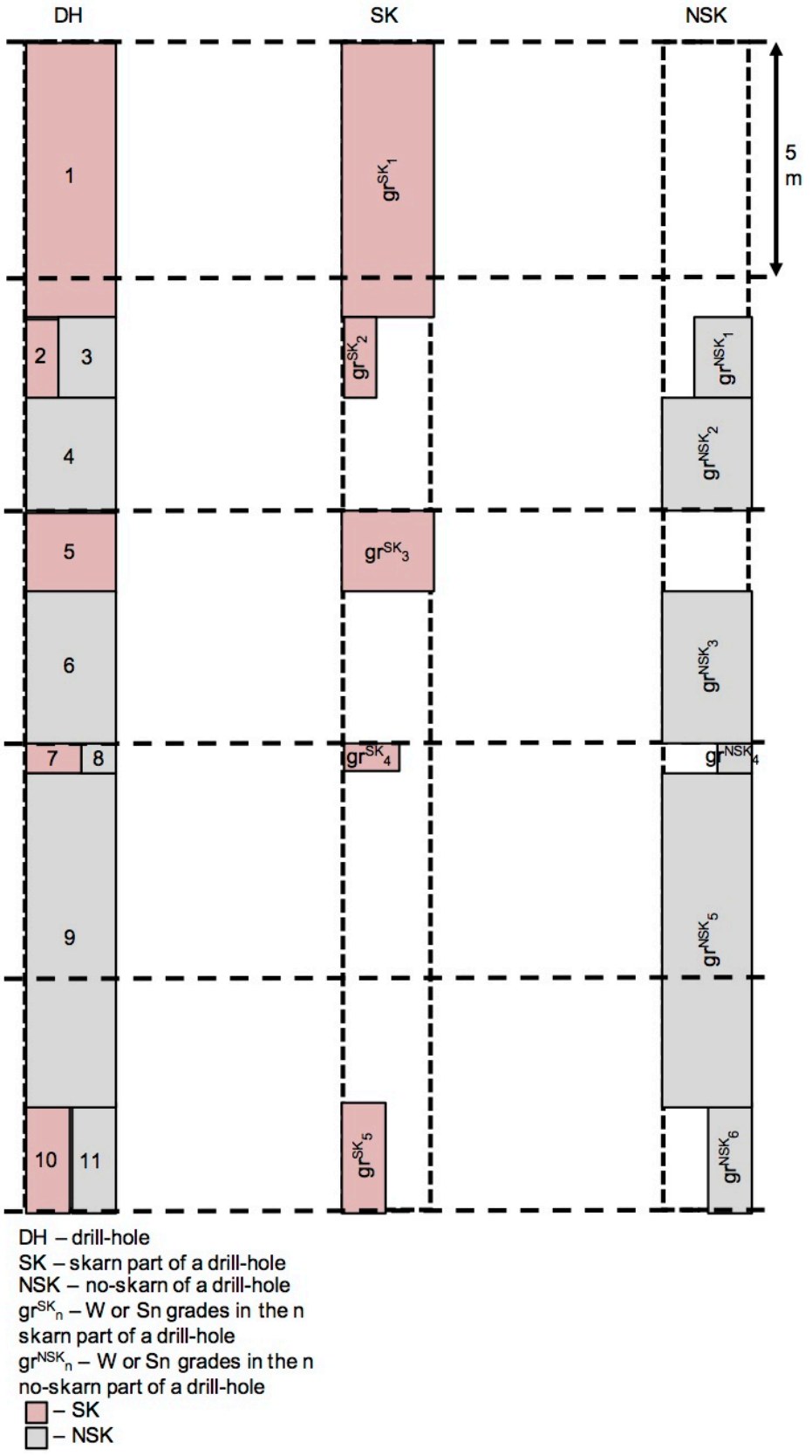

Figure 4.5 – Scheme exemplifying the split of a drill-hole in skarn and no-skarn lithologies, independently of the existent grades.

5. Case study

This chapter presents the case study encompassing the preparation of information, the statistical analysis, and the construction of the low-resolution geological model and the high-resolution morphological model, followed by the construction of the W and Sn grades numerical models. Global resources of ore and metals and the parameter curves are also presented and discussed.

5.1. Data processing

First, the X and Y coordinates of the drill-holes were rotated 30° clockwise in order to align the principal direction of the structure with a coordinate axes, and to facilitate the interpretation of variograms. Secondly, the lithologies found in the drill-holes were classified into two groups: (1) skarns lithologies; and (2) no-skarn lithologies. Thus, the skarns layered to massive, the skarns layered and the indifferentiated skarns were merged into a general group of skarn lithologies; whilst the remaining lithologies, aplites, granites, pegmatites, migmatites, quartz and calcite veins, biotite and black/dark grey schists, carbonates or calcschists, calcsilicate lithologies or poorly developed skarns, faults breccia and filled with gauge, probable and obvious faults, overburden, solution cavities, and core losses, were merged into a complementary group of no-skarn lithologies.

Also, to apply the proposed methodology presented in the previous section, two block models were initiated within a volume of 650 m by 350 m in the horizontal and 300 m in depth (Figure 3.15): (1) one of lower resolution with a block size of 50 m to condition locally the intensity of the generated skarns with the vector algorithm model; and (2) another of higher resolution with a block size of 5 m to generate the W and Sn grades numerical model. The first grid has a mesh of 13 by 7 by 6 blocks (a total of 546 blocks) and the second grid has 130 by 70 blocks in the horizontal and 60 blocks in the vertical (a total of 546000 blocks). It is important to remark that the data available in the drill-holes were resampled in compliance with those two sizes of blocks (50 m and 5 m, respectively) using proportions for lithologies and mobile averages for grades, respectively. As this mineral deposit occurs near the surface and is cropping out in some places, the digital elevation model (DEM) was used to constrain both block models (Figure 3.15).

5.2. Univariate and bivariate statistical analysis

The most relevant univariate and bivariate statistical results for W and Sn grades are presented in Figures 5.1 and 5.2, and Tables 5.1, 5.2 and 5.3. Figures 5.1 a and b show the conditional cumulative histograms of W and Sn grades, respectively. These conditional cumulative histograms demonstrate the dependence or zoning effect between the W and Sn grades and the skarn and no-skarn lithologies, in which both W and Sn grades are higher in skarns as expected. However,

due to misidentification of lithologies, transition depths between lithologies, or other unidentified errors, about 10-20% of the samples of no-skarn lithologies exhibit higher W and Sn grades than what was expected. The average values shown in Table 5.1 confirm this zoning effect, which is still more evident for W grades than for Sn grades. As mentioned in section **4.3.3. W and Sn grades model**, the proposed methodology can handle this mixture of populations, however the uncertainty of the final results will be higher because the individual conditional histograms have a higher variance or dispersion.

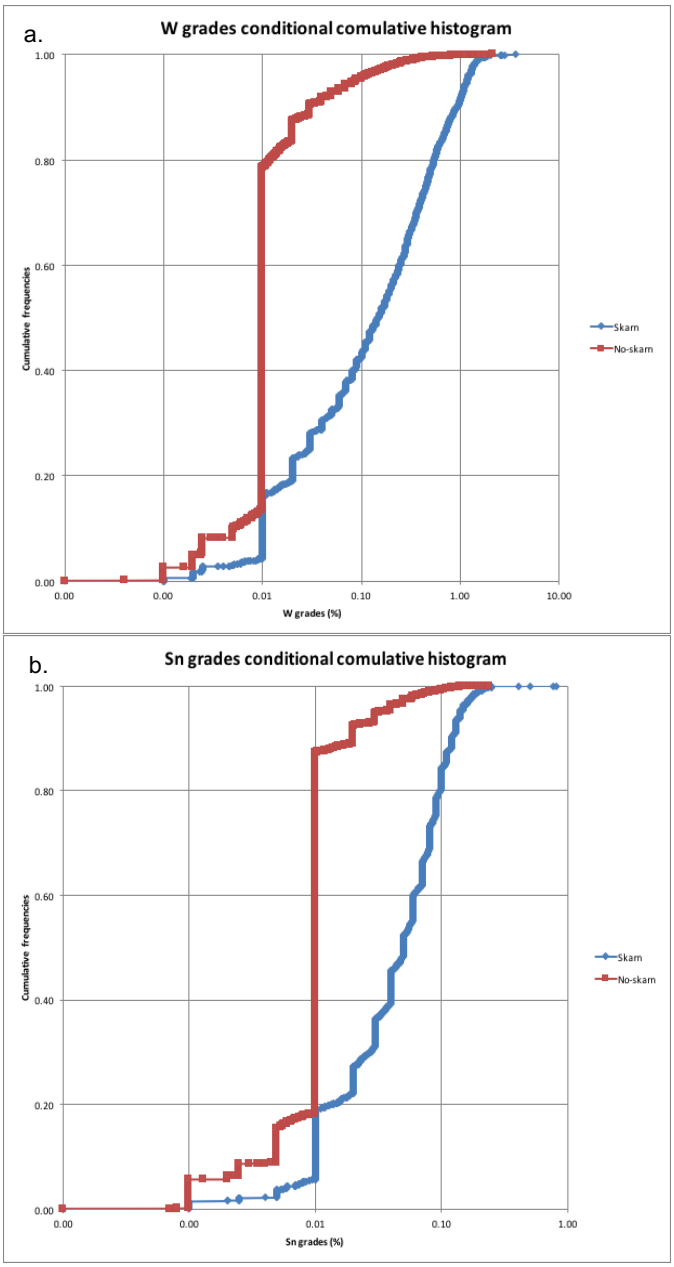

Figure 5.1 – Conditional cumulative histograms of W (1) and Sn (b) grades by proportion of length of the sampled drill-hole.

Table 5.1 – Conditional univariate statistics of W and Sn grades by skarn and no-skarn sets of lithologies.

	Groups	Number of samples	Average (%)	Variance ($\%^2$)
W	**Skarn**	1893	0.27	0.1407
	No-skarn	5416	0.04	0.0157
Sn	**Skarn**	1893	0.06	0.0030
	No-skarn	5416	0.02	0.0005

In order to validate and quantify the dependence between grades and lithologies, a one factor ANOVA test was performed (table 5.2). Basically, the one factor ANOVA utilizes the Fisher-Snedecor distribution to quantify the probability of the hypothesis of a variable to belong or not to the same population. Analysing the results of Table 5.2, it is possible to verify that the probability of both W and Sn grades belonging to the same population is close to 0, meaning that the W and Sn grades measured within skarn and no-skarn lithologies constitute two distinct statistical populations.

Table 5.2 – Results of the one factor ANOVA test for for both W and Sn grades within skarn and no-skarn lithologies.

	Source of variation	Sum of squares	Degrees of freedom	Mean square	F-ratio	Probability	F critical
W	**Between groups**	73.45	1.00	73.45	1527.35	0.00	3.84
	Within groups	351.38	7307.00	0.05			
	Total	424.83	7308.00				
Sn	**Between groups**	2.25	1.00	2.25	2050.41	0.00	3.84
	Within groups	8.03	7307.00	0.00			
	Total	10.28	7308.00				

Lastly, Figure 5.2 shows the scatter plot between W and Sn grades, where a Pearson correlation coefficient of 0.63 is found. Therefore, the simulation of both W and Sn variables must follow a simulation plus a co-simulation procedure, that is, first to apply the DSS algorithm for the generation of simulated images of the W grades, and afterwards to apply the CoDSS algorithm for the simulation of Sn grades images constrained to the previously simulated images of W grades.

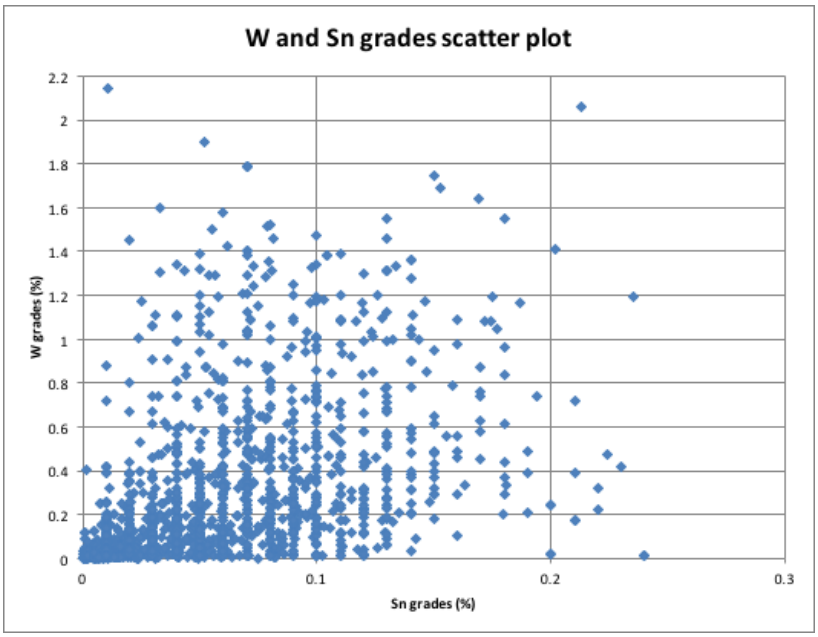

Figure 5.2 – Scatter plot of W and Sn grades.

5.3. Spatial continuity evaluation

The experimental variograms and fitting theoretical models were made for the studied variables: (1) proportion of skarn lithologies; (2) W grades; and (3) Sn grades. The results are presented in Figure 5.3 and a synthesis of parameters in Table 5.3.

Table 5.3 – Skarn lithologies proportion and W and Sn grades parameters of variograms theoretical models (Gomes *et al.*, 2015b).

	Direction (Azimuth; Dip)	Tolerance (°)	Lag distance (m)	Cut distance (m)	Model type	Relative sill	Range (m)
Skarn amount	**(0; 20)**	30	10	2500	Exponential	0,056	35
	(0; -70)	30	10	2500			18
	(90; 0)	30	5	2500			15
W	**(0; 20)**	30	10	2500	Spherical	1	40
	(0; -70)	30	10	2500			30
	(90; 0)	30	5	2500			22
Sn	**(0; 20)**	50	10	2500	Spherical	1	40
	(0; -70)	45	10	2500			25
	(90; 0)	30	10	2500			30

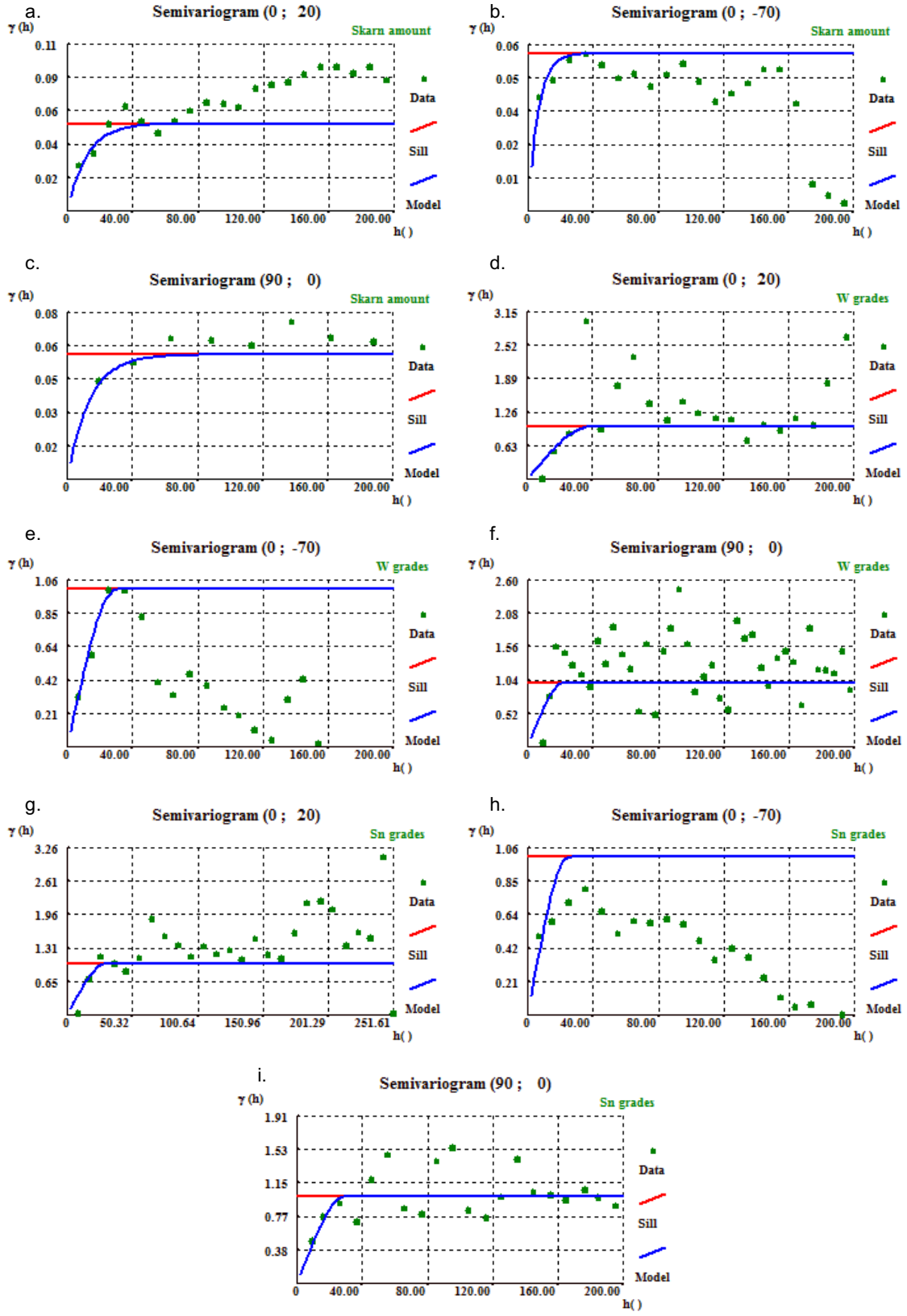

Figure 5.3 – Skarn lithologies proportion and grades variograms, and theoretical models adjusted: (a) skarn proportion (Azimuth: 0°; Dip: 20°) direction; (b) skarn proportion (Azimuth: 0°; Dip: -70°) direction; (c) skarn proportion (Azimuth: 90°; Dip: 0°) direction (d) W grades (Azimuth: 0°; Dip: 20°) direction; (e) W grades (Azimuth: 0°; Dip: -70°) direction; (f) W grades (Azimuth: 90°; Dip: 0°) direction; (g) Sn grades (Azimuth: 0°;

Dip: 20°) direction; (h) Sn grades (Azimuth: 0°; Dip: -70°) direction; and (i) Sn grades (Azimuth: 90°; Dip: 0°) direction (adapted from Gomes *et al.*, 2015b).

For calculation of the experimental variograms, three perpendicular directions were chosen according to the orientation of the structure of the ore deposit, *i.e.*, lens-shaped skarns main direction and dip, which dips roughly 10° to southwest: (1) the main direction of the structure (azimuth: 0°; dip: 20°); (2) the perpendicular direction of the structure (azimuth: 0°; dip: -70°); and (3) the perpendicular direction of the previous ones (azimuth: 90°; dip: 0°). Analysing both Figure 5.3 and Table 5.4, the theoretical model type that better fits the variable proportion of skarn lithologies was the exponential function, while for the W and Sn grades was the spherical model. All three variables exhibit similar anisotropy and variograms ranges.

5.4. Morphological model

The construction of the morphological model encompasses two steps, the construction of a low-resolution vector (geological) model, followed by a high-resolution (morphological) model of skarn proportions conditional to the first low-resolution geological model.

The low-resolution vector (geological) model uses a 50 m size block model to constrain locally the intensity or number of intersections with the skarn lithologies. This grid contains 546 blocks (13 by 7 in the horizontal and 6 in the vertical). Then, the number of intersections was evaluated for the entire block model, first by merging the drill-holes with the 50 m blocks, and after by estimating the number of intersections with the skarn lithologies for the blocks that have no skarn intersections with the drill-holes. The drill-holes have 676 intersections with lens-shaped skarns.

Afterwards, an improved version of the 2D object-based simulation algorithm proposed by Simões (2014) to generate the lens-shaped skarn geobodies was used to build the skarn vector polygons conditioned to local orientation angles. This object-based simulation algorithm runs for each of the 13 cross-sections in the “new” (30° clockwise rotation) OX direction spaced 50 m, and imposes local dip angles into two regions, left and right of each cross-section (Figure 5.4). Figure 5.4 a and b shows the cumulative distribution laws of the dip angles measured on the geologists’ hand-drawn cross-sections for both regions 1 and 2 (left and right, respectively). Region 2 has two cross-sections less because the cross-sections 12 and 13 have only one region (region 1). The histograms of region 1 demonstrate that this region has higher dip angles (varying from -20° to 55°), than region 2 (ranging from -30° to 40°).

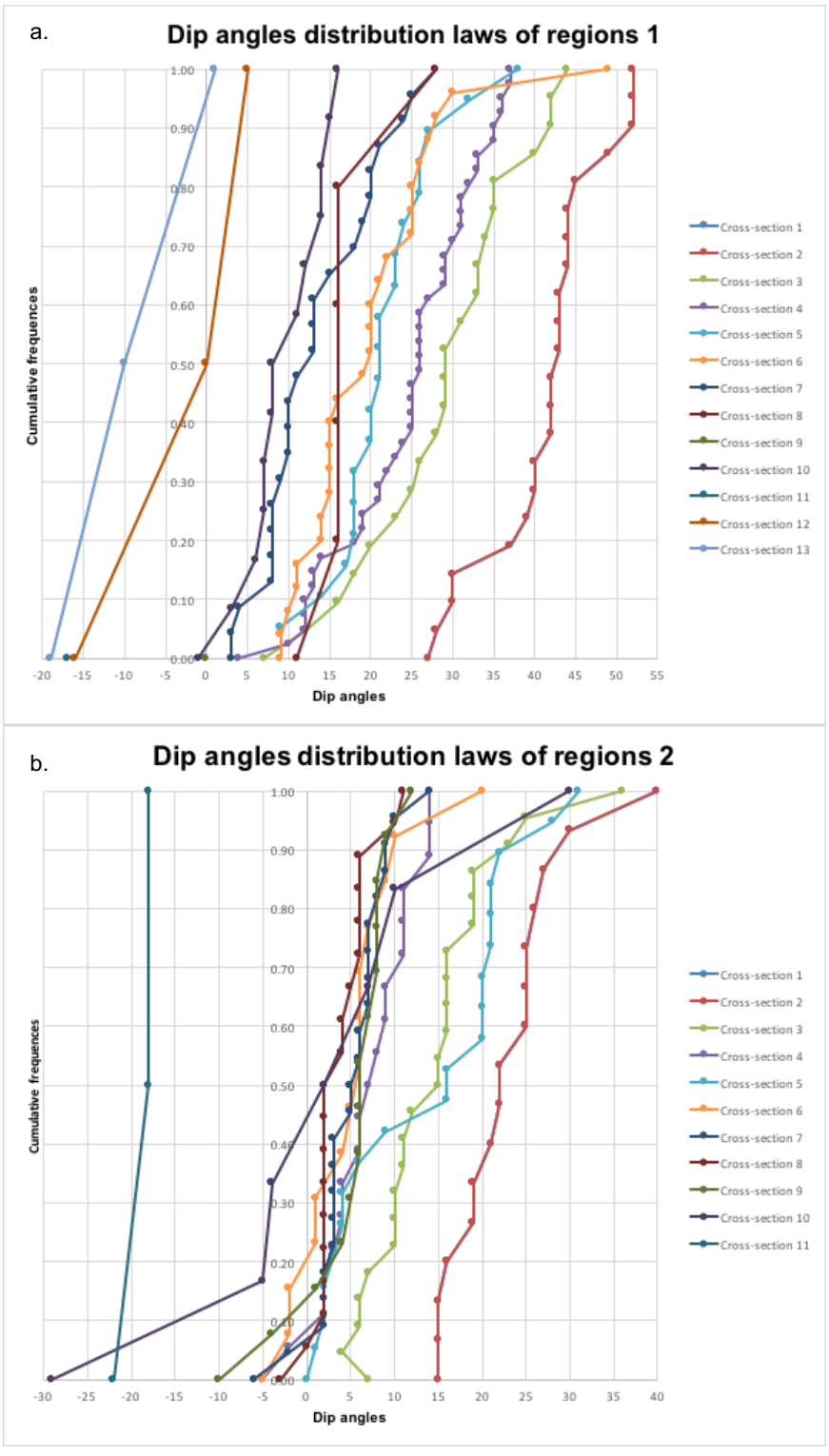

Figure 5.4 – Dip angles distribution laws for each cross-section: (a) region 1; and (b) region 2.

As the geologists' cross-sections are 25 (Figure 3.14), they were considered pairwise (with exception of the westernmost that was considered alone) to impose the angle measures in the object-based model algorithm. To create the hypothetical links between skarns intersections, this

algorithm was programmed to query for intersections at a maximum distance of 100 m. It was also programmed to generate lateral segments until to a maximum of 100 m in the case of it does not find another drill-hole to connect. 100 realizations of the lens-shaped skarn geobodies were generated. Figure 5.5 shows an example of the simulated skarns as closed polygons, where the orientation of the structure and the position of the drill-holes is clearly visible.

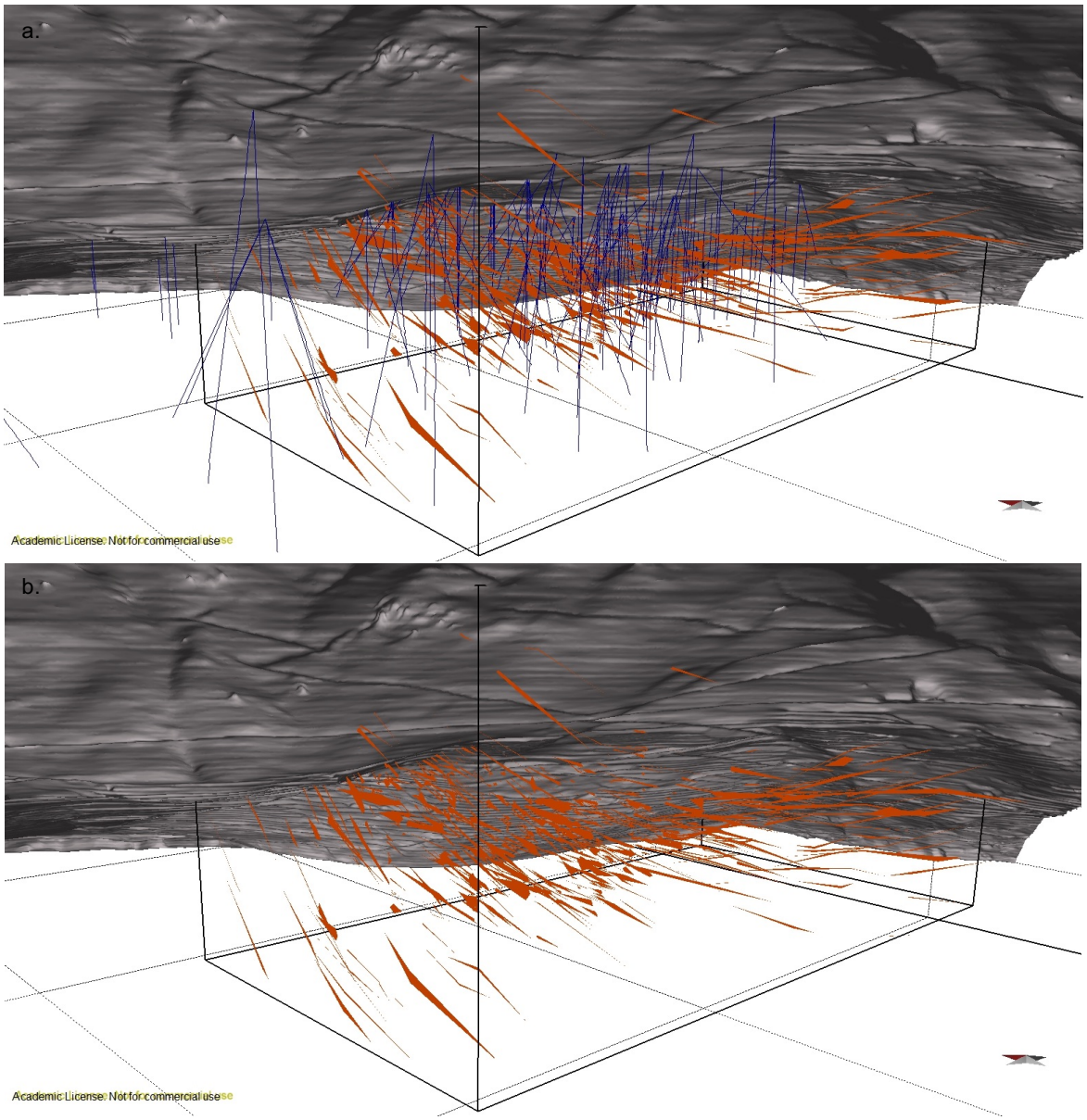

Figure 5.5 – Western under DTM view of the cross-sections with a realization of the lens-shaped skarns object-based model: (a) with drill-holes; and (b) without drill-holes.

Then, the proportion of skarn and no-skarn (F^{SK} and F^{NSK}) was calculated for each large block and simulation by scan-line sampling, and 100 results were averaged to a most probable value per

block (Figure 5.6). The F^{SK} and F^{NSK} sum up not only the information of drill-holes, namely the intersections and thicknesses, but also the information of the overall structure (the lens-shaped skarn intensity and orientation).

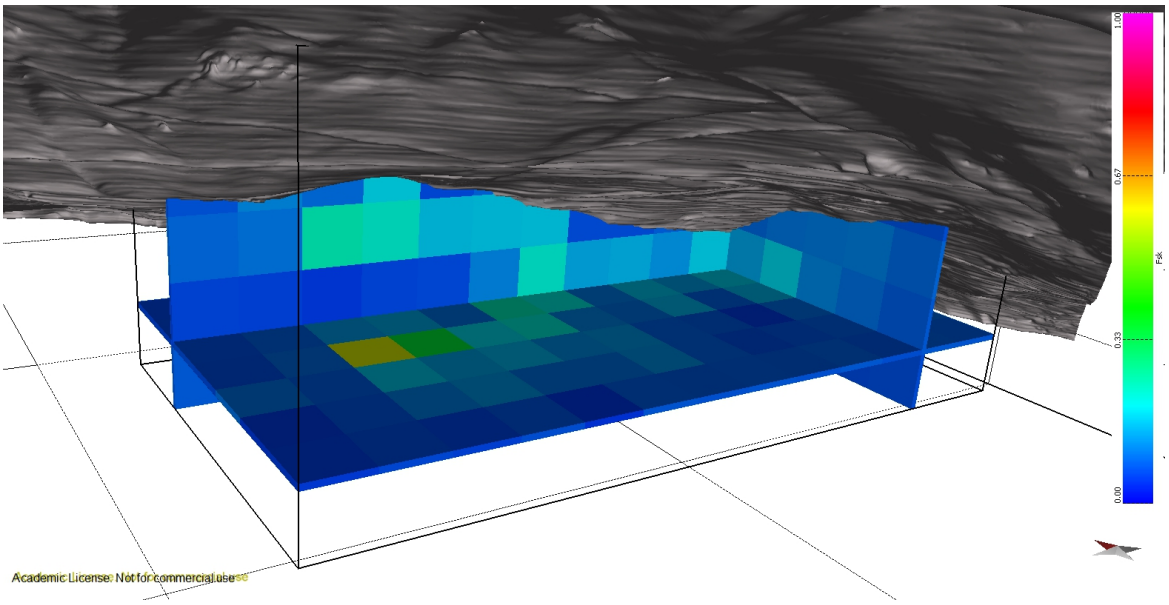

Figure 5.6 – Western under DTM view of the low-resolution geological model mean results of F^{SK}.

Afterwards, the low-resolution geological model at a resolution of 50 m was downscaled to a higher resolution of 5 m, being the high-resolution morphological model. The objective of this stage is to start working in the mine mesh of blocks using the DSS algorithm with local means. More 100 realizations were performed again, and then averaged to a single image of the F^{SK} and F^{NSK} (complementary to one).

Figures 5.6 and 5.7 represent the partial and final results of the morphological model for a selected intermediate cross-section. It is possible to observe that the F^{SK} is higher in the inner part of the deposit, where there are more drill-holes (Figure 5.5). Figure 5.5 shows the orientation of the overall structure of the São Pedro das Águias skarn ore deposit. The structure is in flexure in which the lens-shaped skarns are more inclined to southwest in the westernmost part of the deposit, and to the eastern part they flatten until a slight change of dip to northeast exists. This fact can be verified in all geologists' hand-drawn cross-sections, and is supported by the dip angles distribution laws for each cross-section (Figure 5.4).

Figure 5.7 presents the results of the sixth cross-section of both geological model and morphological model in order to compare the results between the models. The results between the first and fiftieth simulations of Figures 5.7 a and b, and e and f are similar, thus there did not exist a high discrepancy between the simulations. Observing the Figures 5.7 a, c, d and e, and b, c, d and f, it is possible to verify that the F^{SK} is higher in the regions with more lens-shaped skarns

generated. Hence, the results were well created and are coincident in these two stages of the methodology.

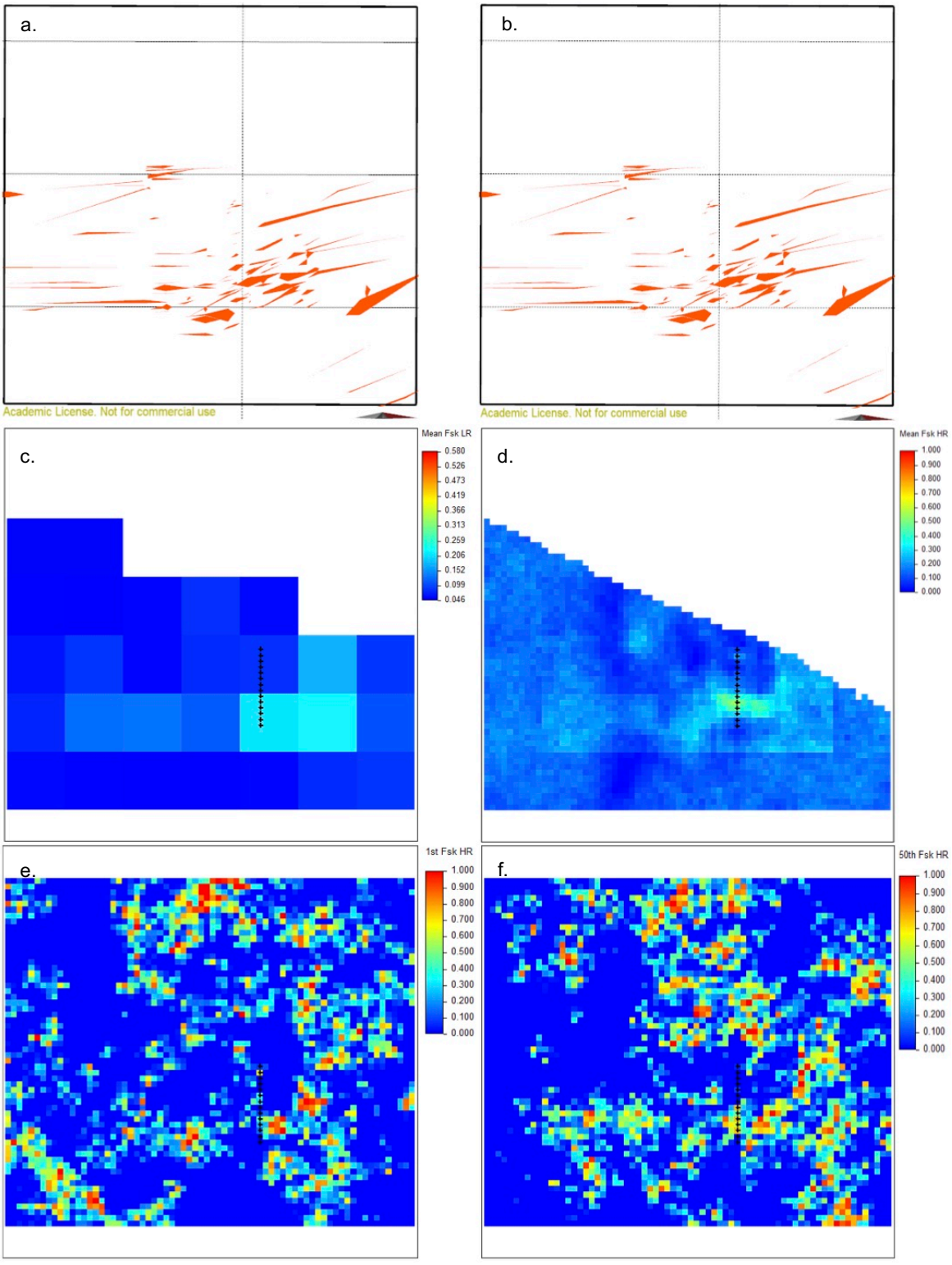

Figure 5.7 – Results of the sixth cross-section of both low-resolution geological model and high-resolution morphological model: (a) low-resolution geological model first realization of the lens-shaped skarns; (b) low-

resolution geological model of the fiftieth realization of the lens-shaped skarns; (c) low-resolution geological model mean results of F^{SK}; (d) high-resolution morphological model mean results of F^{SK} down-scalling; (e) high-resolution morphological model of the fiftieth realization of the F^{SK} down-scalling; and (f) high-resolution morphological model of the fiftieth realization of the F^{SK} down-scalling.

5.5. W and Sn grades model

The global drill-hole dataset of W and Sn grades was separated in four sets, skarn and no-skarn lithologies, and W and Sn grades. For each set of lithologies (skarn and no-skarn) 100 realizations of W grades were simulated, and then 100 images for the Sn grades were co-simulated (using DSS and CoDSS, respectively). Figures 5.8 and 5.9 display for the sixth cross-section two simulated images of W and Sn grades (a and b, and c and d, respectively) for skarn and no-skarn lithologies, respectively.

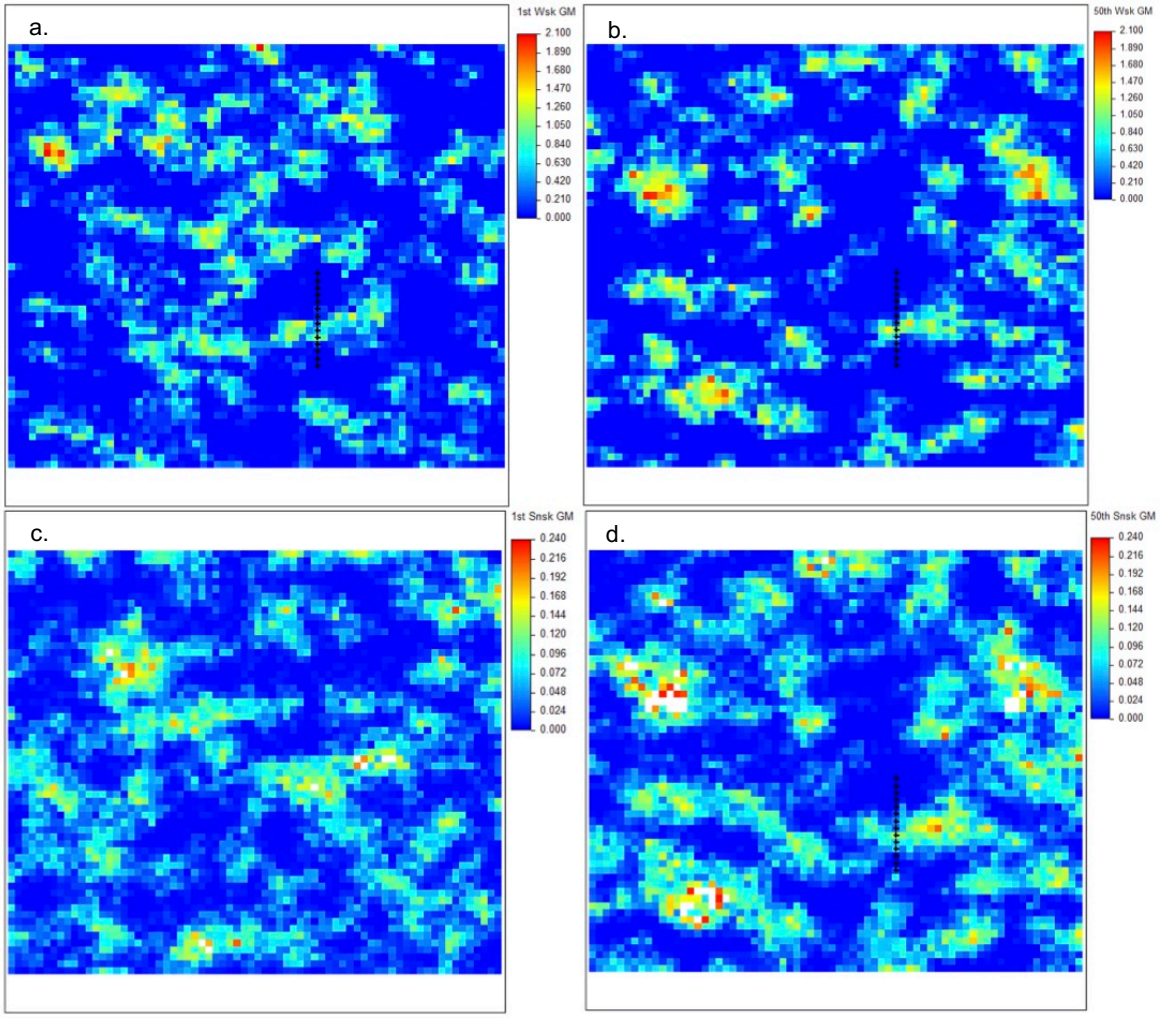

Figure 5.8 – Results of the sixth cross-section of the W and Sn grades model for skarn lithologies: (a) first realization of W; (b) fiftieth realization of W; (c) first realization of Sn; (d) fiftieth realization of Sn.

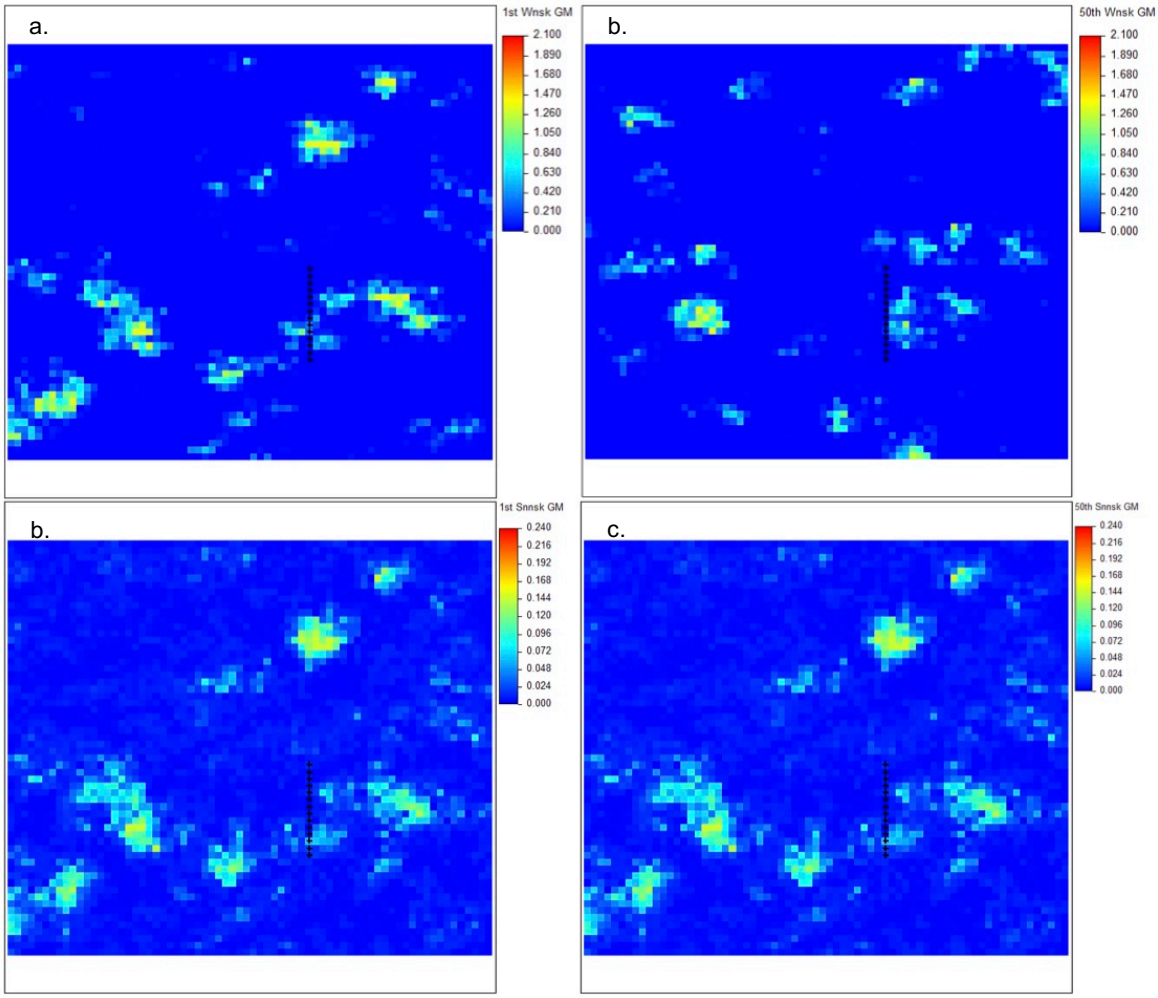

Figure 5.9 – Results of the sixth cross-section for the W and Sn grades model for no-skarn lithologies: (a) first realization of W; (b) fiftieth realization of W; (c) first realization of Sn; (d) fiftieth realization of Sn.

Making use of the previous estimated proportion of skarn lithologies within each block (F^{SK}) and the W and Sn simulated grades, W and Sn grades local conditional cumulative distribution functions for each 5 m grid block were created by applying a proportional mixture of histograms. Finally, simulated images of W and Sn grades were generated by the PFS algorithm making use of the local conditional cumulative distribution functions for W and Sn grades. A total of 100 images for each variable (W and Sn grades) were generated.

Figures 5.10 and 5.11 show in 3D two simulated images for W and Sn grades, respectively. Figure 5.12 shows a cross-section of two final simulated images of W and Sn grades, respectively. Figure 5.13 shows the mean and the variance of the 100 simulated W and Sn grades, respectively. Finally, Figure 5.14 shows in 3D the 10% of blocks with lower uncertainty in what concerns W grades.

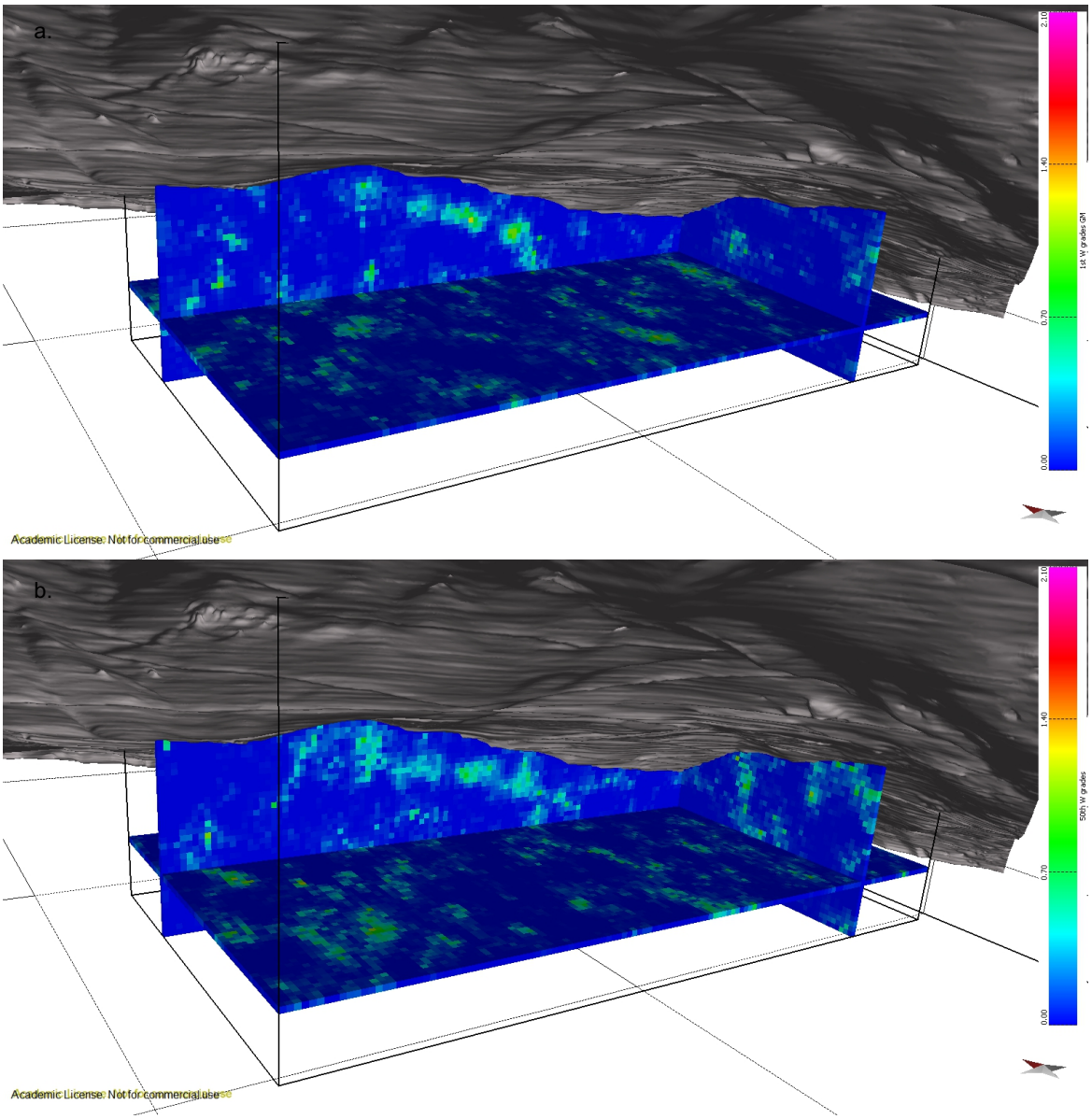

Figure 5.10 – Western under DTM view of the final images of W grades model: (a) first realization; (b) fiftieth realization.

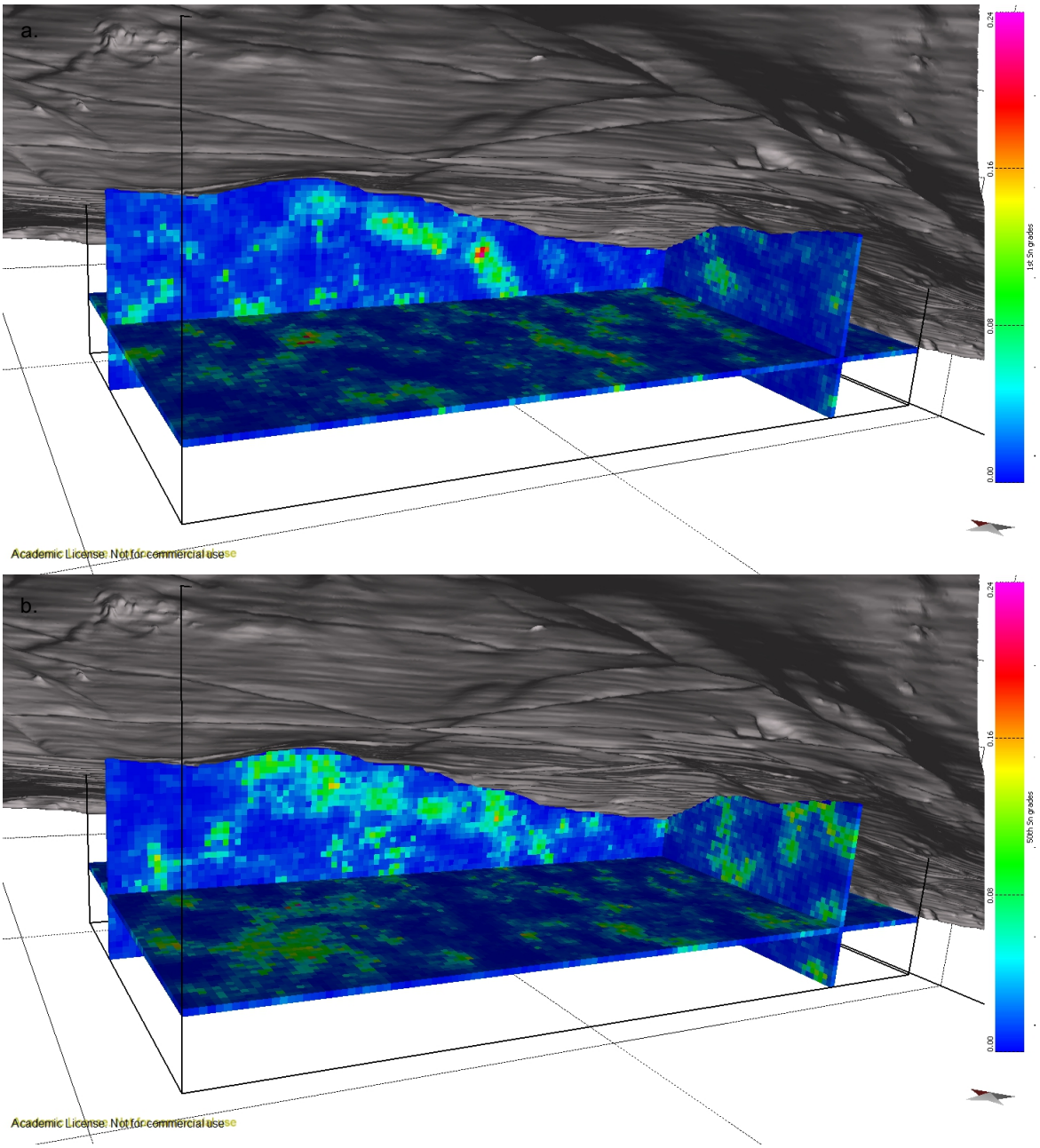

Figure 5.11 – Western under DTM view of the final images of Sn grades model: (a) first realization; (b) fiftieth realization.

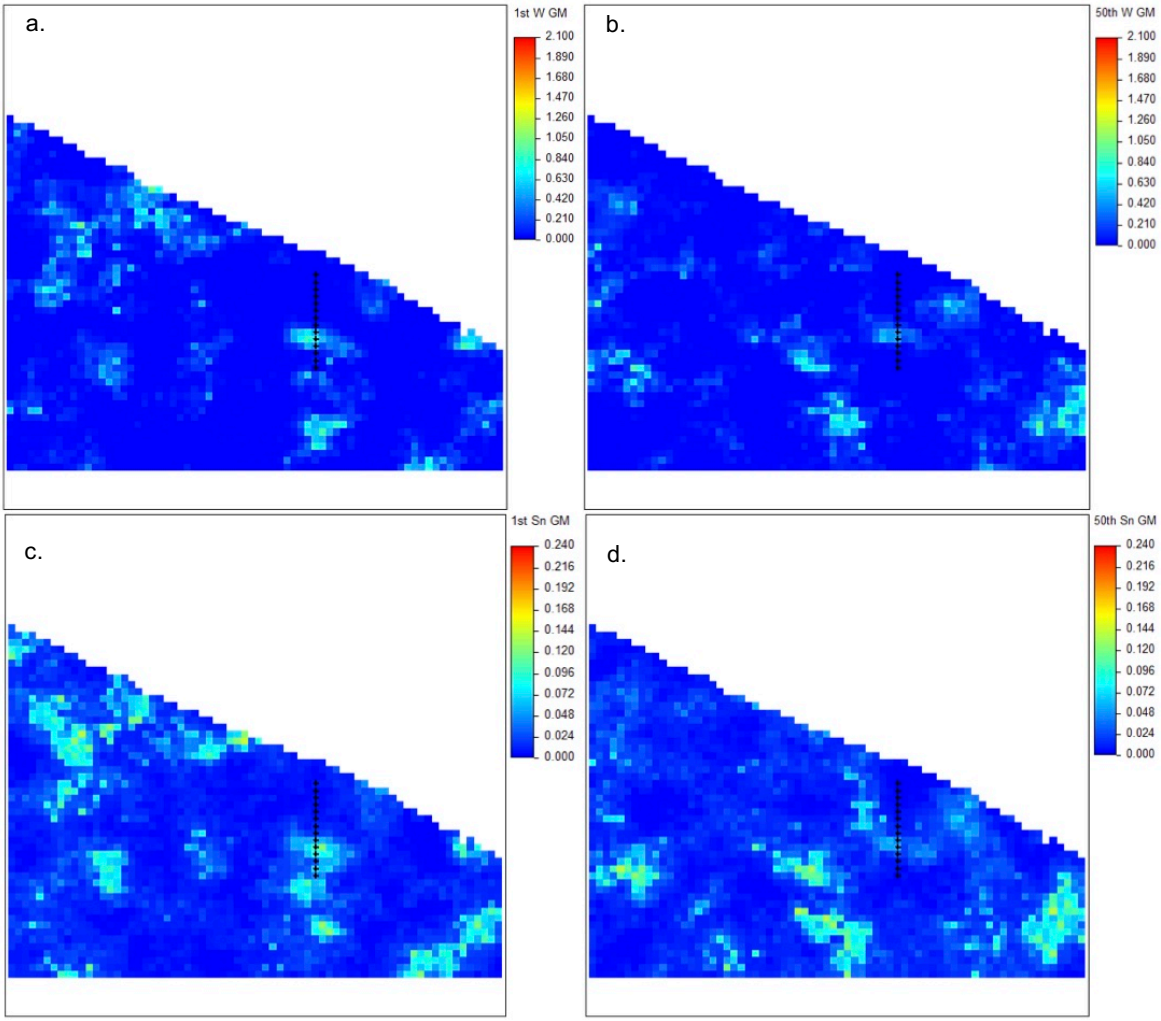

Figure 5.12 – Results of the sixth cross-section of the final images of W and Sn grades model: (a) first realization of W; (b) fiftieth realization of W; (c) first realization of Sn; (d) fiftieth realization of Sn.

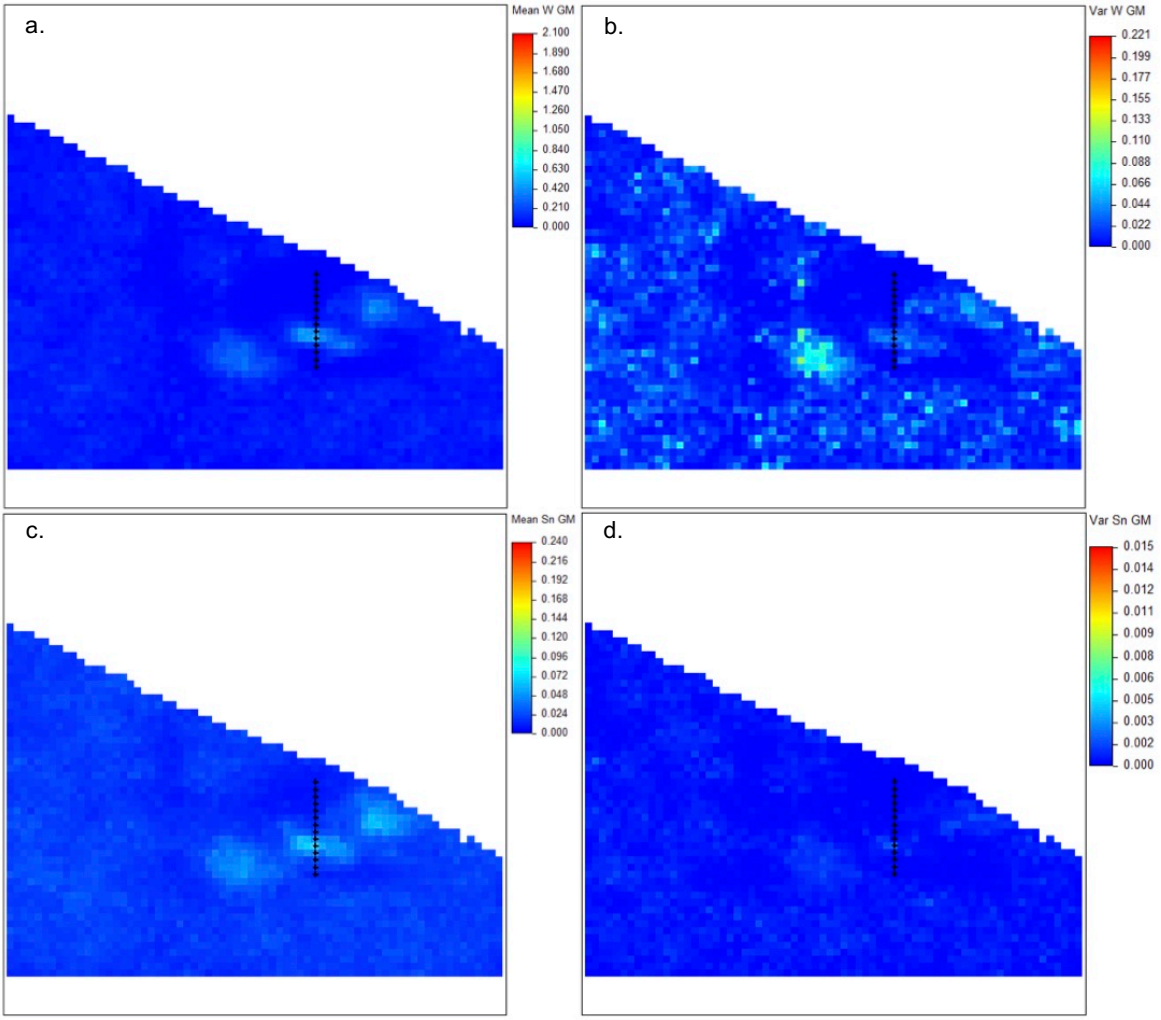

Figure 5.13 – Results of the sixth cross-section of the mean and uncertainty final images of W and Sn grades model: (a) mean of W; (b) uncertainty of W; (c) mean of Sn; (d) variance of Sn.

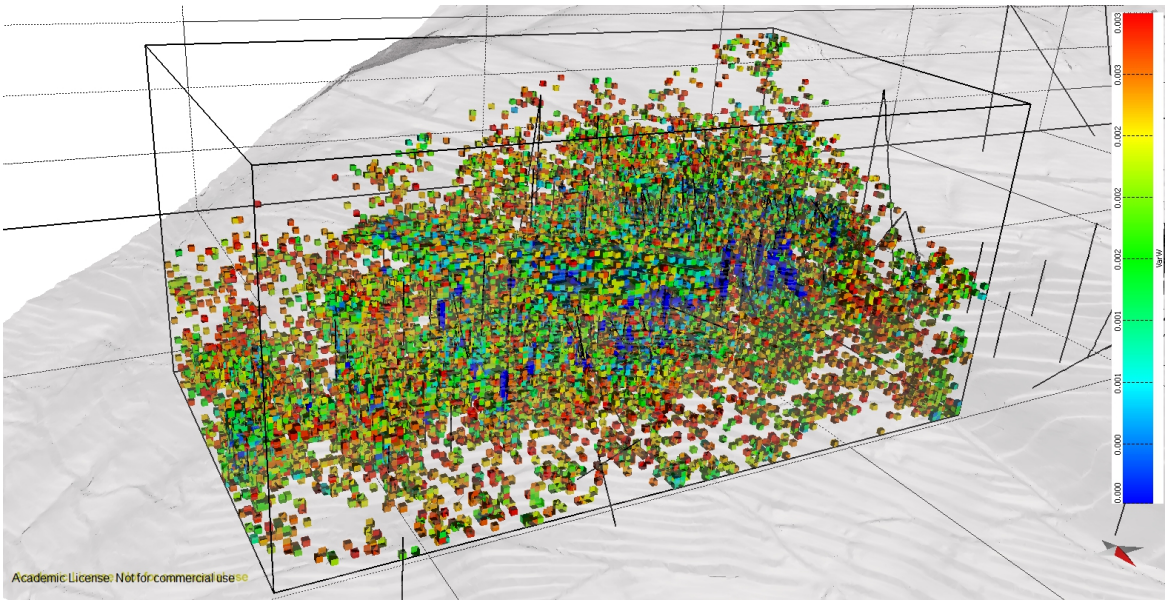

Figure 5.14 – Eastern view of the mean results of W grades model with blocks of 10% certainty.

The results of Figures 5.10 a and 5.11 a, and 5.10 a and 5.11 b are correlated, because the highest grades are located in similar places of the images. Comparing the first with the fiftieth realizations of both figures (5.10 and 5.11 a and b, respectively), it is possible to verify that in the location of the drill-holes the results are similar without discrepancies between realizations. Comparing Figure 5.5 with Figure 5.10 and 5.11, it is verified that the disposition of the grades stains is according to the disposition of the automatic simulated lens-shaped skarns, validating that the W and Sn grades model were built constraining to the geological model and the morphological model.

The results of the sixth cross-section of both the W and Sn grades model for skarn lithologies first (a) and fiftieth (b) realizations are presented in Figure 5.8, and for no-skarn lithologies in Figure 5.9. These realizations also do not have a high discrepancy between them, so both W and Sn grades are well correlated.

Figure 5.12 reports the results of the sixth cross-section of the final images of W and Sn grades first (a) and fiftieth (b) realizations. The figure demonstrates that the higher grades for both W and Sn are mostly around the drill-holes.

Figure 5.13 shows the results of the sixth cross-section of the mean and variance (uncertainty) final images of W and Sn grades model. Figures 5.13 a and c display that the W and Sn grades are also higher around the drill-holes than in the remainder regions, being in according to the results of W and Sn grades of Figure 5.12. Analysing Figures 5.13 b and d, the uncertainty is higher in the regions there are no drill-holes and lower around them, as expected.

Finally, Figure 5.14 demonstrates the 3D view of uncertainty. It reports a lower uncertainty in the central region of the deposit, coincident with a higher number of drill-holes, and probably a lower

discrepancy between the measured grades (being according to the results of Figure 5.13 b).

5.6. Resources summary

This section presents a summary of ore and metal quantities as result of the applied methodology, and as a comparison with the indicated resources calculated by Colt in October 2012 (O'Donovan *et al.*, 2012; Beare and MacDougal, 2013). The resources are reported in charts containing the minimum, mean and maximum resources. The factor % WO_3 is calculated multiplying a factor of 1.2611 by the % W.

Figures 4.15 a and b present the curves of ore and metal quantities, respectively, for WO_3 as function of W grades obtained in the present methodology. Figures 5.16 a and b shows the curves of WO_3 and Sn average grades, respectively, as function of W grades also as obtained in the present methodology. Figure 5.17 reports the curves of WO_3 metal and grades as indicated resources evaluated by Colt in October of 2012. Finally, Table 5.5 demonstrates the resources calculated using the applied methodology and calculated by Colt. The curves of minimum, mean and maximum resources of Figures 5.15 a and b, and 5.16 a show small variability between them. This happens because the simulations are conditional to the experimental histogram of the simulated variable and the values are presented aggregated to the entire grid of blocks.

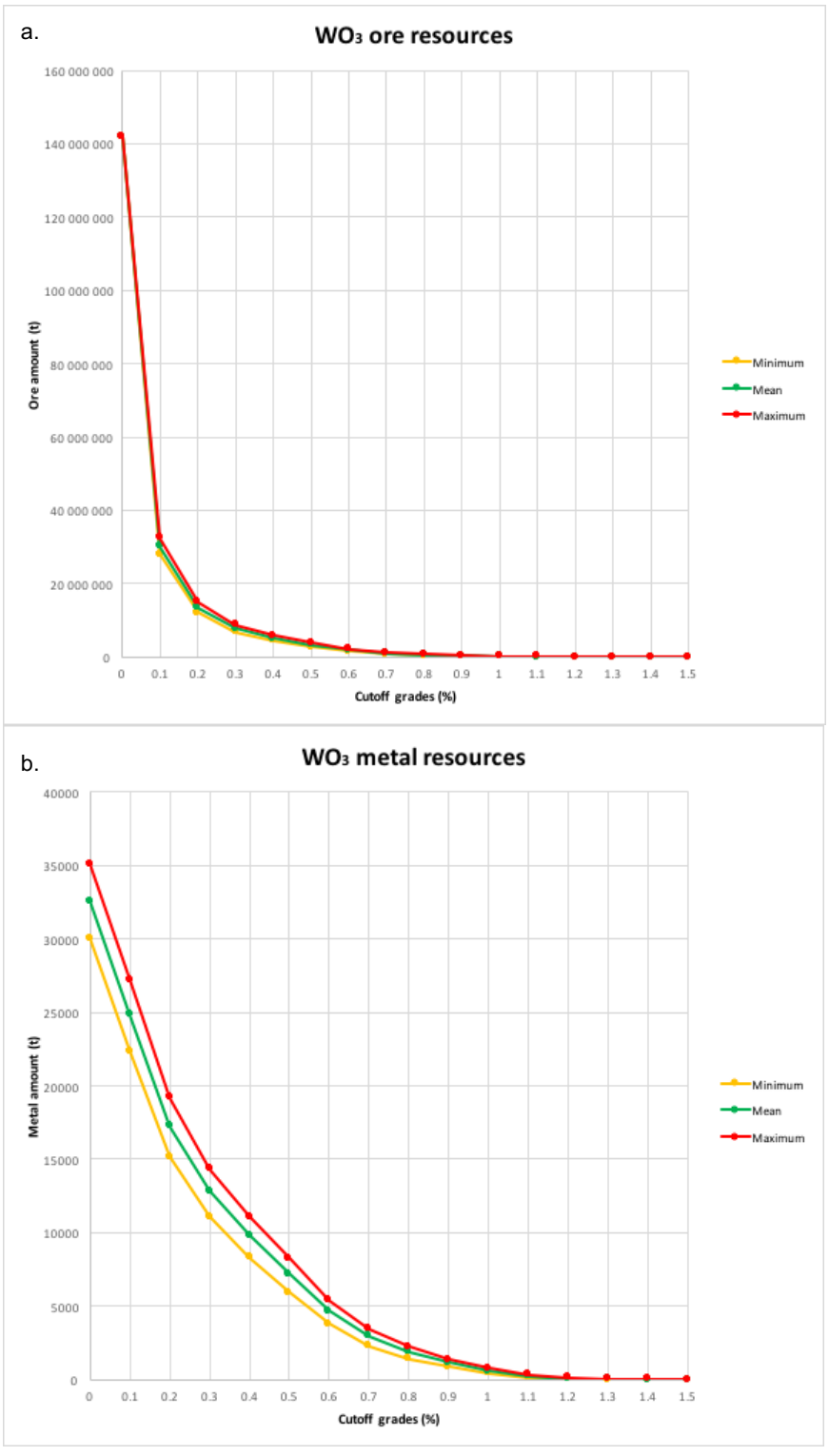

Figure 5.15 – Curves of WO_3 ore (a) and metal (b) resources.

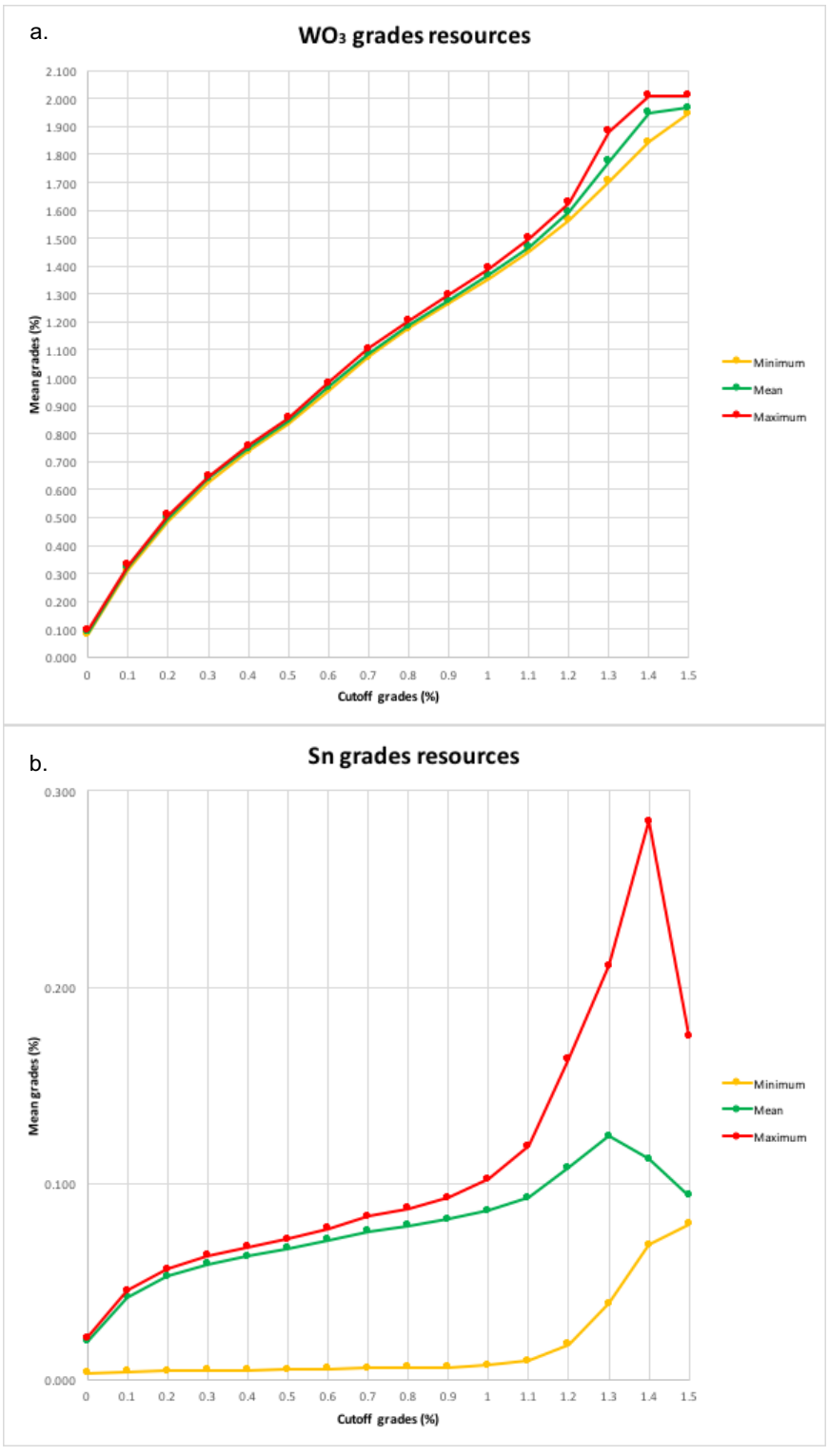

Figure 5.16 – Curves of grades resources: (a) WO_3 grades; and (b) Sn grades.

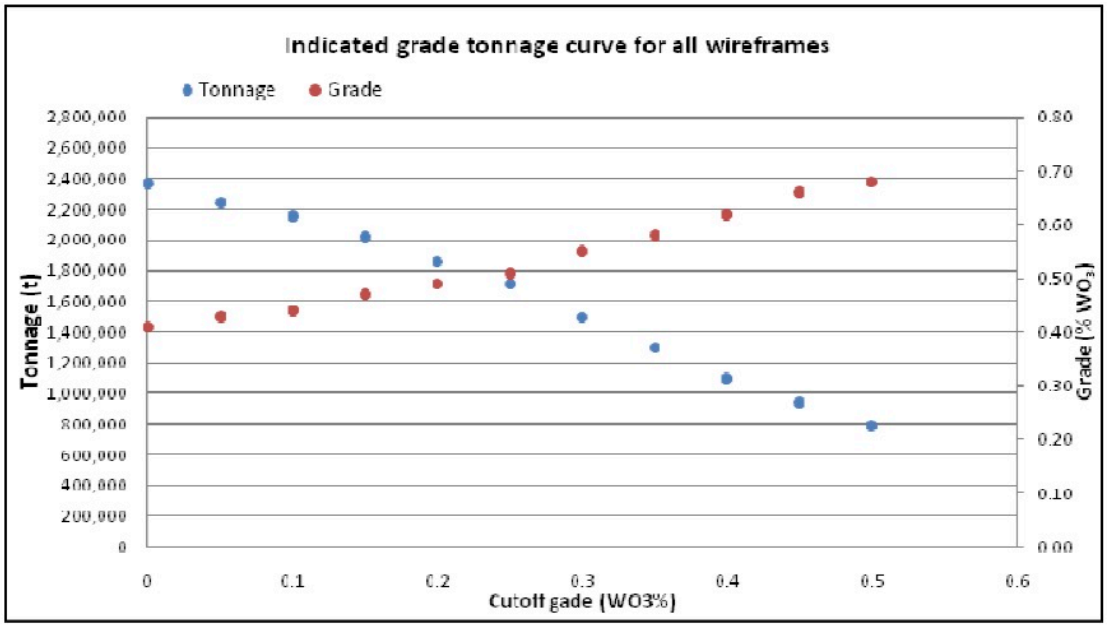

Figure 5.17 – Curves of WO_3 metal and grades indicated resources evaluated by Colt in October of 2012 (O'Donovan *et al.*, 2012; Beare and MacDougall, 2013).

Table 5.4 – Resources evaluated using the applied methodology and indicated resources calculated by Colt in October 2012.

		Cutoff grade (% WO_3)	Ore amount (t)	Grades (% WO_3)	Metal amount (t WO_3)	Volume (m^3)
Methodology resources	**Minimum**	**0**	141,848,328	0.08	30,070	45,757,525
	Mean		141,848,328	0.09	32,579	45,757,525
	Maximum		141,848,328	0.10	35,112	45,757,525
Colt indicated resources			2,365,000	0.41	9,650	765,000

Analysing Table 5.5, the resources evaluated using the applied methodology, for a cutoff grade of 0.00% WO_3, are: (1) the ore amount is about 141,848,300 t; (2) the minimum grade is 0.08% WO_3 and the maximum of 0.10%; and (3) the minimum metal amount of about 30,000 t WO_3 and a maximum of 35.112 t WO_3. While, the Colt indicated resources, for a cutoff grade of 0.00% WO_3, are: (1) the ore amount is 2,365,000 t; (2) the grade is 0.41 % WO_3; and (3) the metal amount is 9,659 t WO_3 (O'Donovan *et al.*, 2012; Beare and MacDougal, 2013). The methodology resources and Colt's indicated resources (Figures 5.15 and 5.17, respectively, and Table 5.5) are not comparable owing to this huge discrepancy between them.

This discrepancy is explained because the applied methodology calculates the resources for the entire model, contrarily to Colt that evaluated the resources using an influence area around the drill-holes in the cross-sections (O'Donovan *et al.*, 2012; Beare and MacDougal, 2013). However, this discrepancy is much higher for both ore amount and volume than for the metal amount. Both

ore amount and volume evaluated by the applied methodology are 60 times greater than Colt's; but the metal amount calculated by the applied methodology is only 3.5 times greater than Colt's. This happens because both ore amount and volume are determined based on the number of blocks (namely their volume); in contrast, the metal amount reflects the results of the simulations. Therefore, as the drill-holes are not equally distributed by the entire volume, the results of the simulations are different from the inner to the external part of the volume.

6. Final remarks

The main intention of the present study was to propose and test a stochastic methodology to generate simulated images of W and Sn grades of the São Pedro das Águias skarn ore deposit (Tabuaço, northern Portugal). This methodology encompasses three main stages: (1) construction of a low-resolution geological model of the morphology; (2) building of a high-resolution morphological model; and (3) generation of the W and Sn grades model. The first stage allowed the incorporation of geological information in the construction of a lens-shaped skarns object-based model using an improved version of the algorithm proposed by Simões (2014). The objective of the second stage was to build a higher resolution model of the morphology, namely introducing and simulating a morphological variable named proportion of skarns F^{SK} and the complementary variable proportion of no-skarns F^{NSK}. Finally, the last step concerns the generation of simulated images of W and Sn grades simultaneously conditional to the morphological model and pairwise correlated. This procedure intends to add geological coherence into the grades model and better characterize its uncertainty.

The use of an automatic vector object-based algorithm to generate possible skarn boundaries conditional to the drill-holes intersections is a faster way than the traditional digitalization process, and enables the generation of several equiprobable scenarios. Constructing a vector object-based model of skarns prior to a more detailed morphological model of proportions has advantages, such as it enables to add more geological control for instance by imposing local orientation ranges of the structure (Gomes *et al.*, 2015b). For example, in the present case study the local angles change according a structure in flexure in which its westernmost lens-shaped skarns have greater dips to southwest than the central and easternmost ones that are flattened and even change the dips to northeast.

Concerning the grades model, the generation of images of W and Sn grades conditional to skarns and no-skarns lithologies, the construction of local histograms mixing the simulations according to the fraction of skarn and no-skarn and the final simulation of the grades images enables to quantify locally the uncertainty of those grades variables, taking into account all the available information at different scales, namely the orientation of the geological structure, the lithologies intersected by the drill-holes (grouped into skarn and no-skarn lithologies), and the W and Sn grades including their bivariate relationship.

About the grades uncertainty, the low-range variograms fitted in all studied variables, and also in grades, makes the uncertainty to be only lower in the vicinity of the drill-holes, and for that reason it is possible only to present confident resources for only a restricted volume. This is more evident in the comparison of quantities presented by Cold and this study, where Colt's results are much lower than the ones presented now. Thus, for better characterization of the resources many more drill-holes are needed, especially in the outer regions of the deposit.

The object-based algorithm used in this case study is in essence the 2D version proposed by

Simões (2014), but the code was translated to C language and local orientation angles were introduced to constrain the shape of the skarns. Several improvements can be made to this algorithm, such as to move to a full 3D geobodies generator and to assign of thicknesses with a continuity model.

This study proves the potentiality of the presented methodology to be applied to similar deposits where the morphology is in form of lenses or stockwork. For instance, in Portugal there is a potentiality to test in the Panasqueira Mines or Neves-Corvo Mines. This methodology is also designed to be used in the early stages of a mining project, namely for the classification of indicated, inferred, or measured resources.

7. References

Aguado, B. V., Azevedo, M. R., Schaltegger, U., Catálan, J. R. M., Nolan, J., 2005. U–Pb zircon and monazite geochronology of Variscan magmatism related to syn-convergence extension in Central Northern Portugal. *Lithos*, 82: 169-184.

Almeida, J., Soares, A., Reynaud, R., 1993. Modeling the shape of several marble types in a quarry. *International Symposium on the Application of Computers and Operations Research in the Mineral Industries*, Montreal, 1993, Proceedings, 452-459.

Almeida, 2010. Stochastic simulation methods for characterization of lithoclasses on carbonate reservoirs. *Earth-Sciences Reviews*, 101: 250-270.

Amaral, F., Dias, R., Coke, C., Romão, J., Ribeiro, A., 2014. A fase de deformação sarda na Zona Centro-Ibérica. *Comunicações Geológicas* 101, Especial I: 239-242.

Arango, C., Fernández, R. D., Arenas, R., 2013. Large-scale flat-lying isoclinal folding in extending lithosphere: Santa María de la Alameda dome (Central Iberian Massif, Spain).

Azevedo, M., Aguado, B., 2006. Origem e Instalação de Granitóides Variscos na Zona Centro-Ibérica. *In*: Dias, R., Araújo, A., Terrinha, P., Kullberg, J. (Ed.), *Geologia de Portugal no contexto da Ibéria*, University of Évora, Évora, pp. 107-121.

Azevedo, M., Aguado, B., 2013. II.1.7. Origem e instalação de Granitóides Variscos da Zona Centro-Ibérica. *In*: Dias, R., Araújo, A., Terrinha, P., Kullberg, J. C. (Ed.), *Geologia de Portugal: Volume I – Geologia Pré-mesozóica de Portugal*, Escolar Editora, Lisbon, pp. 377-401.

Balda, M. A. D., Vegas, R., Lodeiro, F. G., 1990. 2.2 Structure. *In*: Dallmeyer, R. D., Garcia, E. M. (Ed.), *Pre-Mesozoic Geology of Iberia*, Springer-Verlag, Berlin-Heidelberg-New York-London-Paris-Tokyo-Hong Kong-Barcelona, pp. 172-188.

Baldé, G. F. M. C., 2012. *Modelação de depósitos minerais amostrados por suportes irregulares. O caso de estudo do depósito de Farim-Saliquinhé na Guiné-Bissau*. Unpublished Ph.D. thesis. NOVA University of Lisbon, Lisbon, 135 pp.

Barbosa, S. V. T., 2012. *Modelação de atributos hidrogeológicos do maciço envolvente à antiga área mineira da Quinta do Bispo*. Unpublished Ph.D. thesis. NOVA University of Lisbon, Lisbon, 168 pp.

Barbosa, S., Almeida, J. A., Chambel, A., 2014. Modelação 3D da transmissividade do maciço granítico envolvente à antiga mina da Quinta do Bispo. *Comunicações Geológicas* 101, Especial II: 959-963.

Beare, M, MacDougal, C, 2013. *A Preliminary Economic Assessment on the Tabuaço Tungsten Project, Portugal*. Unpublished technical report. SRK Consulting (UK) Limited, Cardiff, 145 pp.

Burt, D. M., 1977. Mineralogy and Petrology of Skarn Deposits. *RENDICONTI Società Italiana di Mineralogia e Petrologia*, 33 (2): 859-873.

Caers, J., 2011. *Modeling Uncertainty in the Earth Sciences*. Wiley-Blackwell, Oxford, 229 pp.

Carvalho, D. L., 2011. *Monitorização de áreas mineiras abandonadas: Metodologias de amostragem*. Unpublished M.Sc. thesis. University of Minho, Minho, 114 pp.

Castro, P., Coke, C., Ferreira, N., Llana-Fúnez, S., Pamplona, J., Pereira, E., Pimenta, P., Rodrigues, B. C., Rodrigues, J., 2010. *Evolução e estrutura da Zona de Cizalhamento Dúctil Malpica-Lamego: Livro guia da excursão pós-congresso*. Unpublished field excursion guide. VIII Congresso Nacional de Geologia, Braga, 63 pp.

Catalán, J. R. M., Arenas, R., García, F. D., Cuadra, P. G., Gómez-Barreiro, J., Abati, J., Castañeiras, P., Fernández-Suárez, J., Martínez, S. S., Andonaegui, P., Clavijo, E. G., Montes, A. D., Pascual, F. J. R., Aguado, B. V., 2007. Space and time in the tectonic evolution of the northwestern Iberian Massif: Implications for the Variscan belt. *In*: Hatcher, R. D., Carlson, M. P., McBride, J. H., Catalán, J. R. M. (Ed.), *4-D Framework of Continental Crust*, Geological Society of America Memoir 200, pp. 403-423.

Catalán, J. R. M., 2011. The Central Iberian arc, and orocline centered in the Iberian Massif and some implications for the Variscan belt. *International Journal of Earth Sciences*, doi: 10.1007/s00531-011-0715-6, 16 pp.

Cerejo, T. A., 2013. *Geoquímica da Área de São Pedro das Águias – Concessão de Tabuaço*. Unpublished M.Sc. thesis. University of Aveiro, Aveiro, 122 pp.

Cerejo, T., Santos, J. F., Sousa, J. C., Castanho, N., Sérgio, G., 2014. Geocronologia e geoquímica isotópica de granitóides e metassedimentos da área de São Pedro das Águias (concessão para a prospecção de W de Tabuaço). *Comunicações Geológicas* 101, Especial I: 61-64.

Charifo, G., Almeida, J. A., Ferreira, A., 2013. Managing borehole samples of unequal lengths to construct a high-resolution mining model of mineral grades zoned by geological units. *Journal of Geochemical Exploration*, 132: 209-223.

Charifo, G., Ferreira, A. M., Almeida, J. A., Prian, J., 2014a. Geochemical and statistical characterization of the phosphate facies of the Farim-Saliquinhé phosphate mineralization (Guinea-Bissau). *Resource Geology*, 64(1): 58-75.

Charifo, G., Almeida, J. A., Ferreira, A., 2014b. Modelação geológica do depósito mineral de Farim-Saliquinhé amostrado por sondagens de comprimento variável. *Comunicações Geológicas* 101, Especial III, 63(3): 1409-1413.

Dallmeyer, R. D., García, E. M., 1990. Introduction to the Pre-Mesozoic Geology of Iberia. *In*: Dallmeyer, R. D., Garcia, E. M. (Ed.), *Pre-Mesozoic Geology of Iberia*, Springer-Verlag, Berlin-Heidelberg-New York-London-Paris-Tokyo-Hong Kong-Barcelona, pp. 3-4.

DG-ENTR, 2010. *Report on critical raw materials for the EU: Report of the Ad-hoc Working Group on defining critical raw materials*. Unpublished technical report. European Comission Entreprise and Industry, Etterbeek, 85 pp.

DG-ENTR, 2014. *Report on critical raw materials for the EU: Report of the Ad-hoc Working Group on defining critical raw materials*. Unpublished technical report. Directorate-General Entreprise and Industry, Etterbeek, 41 pp.

Dias, R., Ribeiro, A., 2013. II.1. O Varisco do sector norte de Portugal. *In*: Dias, R., Araújo, A., Terrinha, P., Kullberg, J. C. (Ed.), *Geologia de Portugal: Volume I – Geologia Pré-mesozóica de Portugal*, Escolar Editora, Lisbon, pp. 59-71.

Dias, R., Ribeiro, A., Coke, C, Pereira, E., Rodrigues, J., Castro, P., Moreira, N., Rebelo, J., 2013. II.1.1. Evolução estrutural dos sectores setentrionais do Autóctone da Zona Centro-Ibérica. *In*: Dias, R., Araújo, A., Terrinha, P., Kullberg, J. C. (Ed.), *Geologia de Portugal: Volume I – Geologia Pré-mesozóica de Portugal*, Escolar Editora, Lisbon, pp. 73-147.

Dias, R., Ribeiro, A., Coke, C., Moreira, N., Romão, J., 2014. Arco ibero-Armoricano: indentação *versus* auto-subducção. *Comunicações Geológicas* 101, Especial I: 261-264.

Dill, H. G., 2010. The "chessboard" classification scheme of mineral deposits: Mineralogy and geology from aluminum to zirconium. *Earth-Science Reviews*, 100: 1-420.

Dimitrakopoulos, R., 1998. Conditional Simulation Algorithms for Modelling Orebody Uncertainty in Open Pit Optimisation. *International Journal of Surface Mining*, 12(4):173-178.

Fernandes, A., Ribeiro, M. A., Lima, A., 2015. Petrography of "skarns" with scheelite. Two examples from northern Portugal. *V Congresso de Jovens Investigadores em Geociências, LEG 2015*, Estremoz, 2015, Scientific Programme and Abstracts, 87-90.

Ferreira, N., Sousa, M. B., Romão, J. C., Francisco, A. S., Santos, A. J., 1987a. *Carta Geológica de Portugal na escala 1/50 000 Folha 14-B Moimenta da Beira*. Direcção Geral de Geologia e Minas, Lisbon.

Ferreira, N., Iglesias, M., Noronha, F., Pereira, E., Ribeiro, A., Ribeiro, M. L., 1987b. Granitóides da Zona Centro Ibérica e seu enquadramento geodinâmico. *In*: Bea, F., Carniceiro, A., Gonzalo, J. C., Plaza, M. L., Alonzo, M. D. R. (Ed.), *Geologia de los Granitoides y Rocas Asociadas del Macizo Hespérico*. Ed. Rueda, Madrid, pp. 37-51.

Ferreira, N. M. R., Macedo, C. A. R., Sousa, M. B., 1987c. Cronostratigrafia dos granitos da região de Moimenta da Beira – Tabuaço – Penedono. *Universidade do Porto – Faculdade de Ciências Museu e Laboratório Mineralógico e Geológico Memórias*, 1: 287-301.

Ferreira, N., Sousa, M. B., 1994. *Notícia Explicativa da Folha 14-B Moimenta da Beira da Carta Geológica de Portugal na escala 1/50 000*. Instituto Geológico e Mineiro, Lisbon, 53 pp.

Flório, R. C. S., 2014. *Estimação da permeabilidade em reservatórios fracturados – Comparação*

entre o método do tensor e o método de upscaling. Unpublished M.Sc. thesis. NOVA University of Lisbon, Lisbon, 72 pp.

Flório, R., Almeida, J., 2015. Comparative study of the tensor and upscaling methods for evaluation permeability in fractured reservoirs. *IAMG 2015*, Freiberg, 2015, Abstracts, 465-474.

Froidevaux, R., 1992. Probability field simulation. *In*: Soares, A. (Ed.), *Geostatistics Tróia '92 – Volume 1*, Kluwer Academic Publishers, Norwell, pp. 73-83.

Gomes, A. R., Barbosa, S. V. T., Brito, M. G., 2015a. Avaliação do risco para a saúde humana de águas subterrâneas contaminadas por hidrocarbonetos – duas abordagens. *X Congresso Ibérico de Geoquímica|XVIII Semana de Geoquímica*, Lisbon, 2015, Abstracts, 340-343.

Gomes, G, Almeida, J., Chichorro, M., Matias, F., 2015b. The simulation of W-Sn grades of the São Pedro das Águias skarn ore deposit (Tabuaço, northern Portugal). *IAMG 2015*, Freiberg, 2015, Abstracts, 1065-1074.

Gomes, G, Almeida, J., Chichorro, M., Matias, F., 2015c. A 2D object-based model of the lens-shaped skarns of São Pedro das Águias deposit (Tabuaço, northern Portugal). *V Congresso de Jovens Investigadores em Geociências, LEG 2015*, Estremoz, 2015, Scientific Programme and Abstracts, 31-34.

Gomes, G, Chichorro, M., Almeida, J. A., Matias, F., 2015d. PCA as a geochemical analysis method for hydrothermal alteration and of skarnization zones in complex environments – the São Pedro das Águias skarn deposit case study. *X Congresso Ibérico de Geoquímica|XVIII Semana de Geoquímica*, Lisbon, 2015, Abstracts, 306-309.

Goovaerts, P., 2002. Geostatistical modelling of spatial uncertainty using *p*-field simulation with conditional probability fields. *International Journal of Geographical Information Science*, 16(2): 167-178.

Horta, A., Caeiro, M. H., Nunes, R., Soares, A. (2010). Simulation of continuous variables at meander structures: application to contamined sediments of a lagoon. *In*: Atkison, P., Lloyd, C. (Ed.), *geoEnv VII – Geostatistics for Environmental Applications. Quantitative geology and Geostatistics*, 16: 161-172.

José, M. A. S., Pieren, A. P., Garcia-Hidalgo, L., Vilas, L., Herranz, P., Pelaez, J. R., Perejon, A., 1990. 2.1.2 Ante-Ordovician Stratigraphy. *In*: Dallmeyer, R. D., Garcia, E. M. (Ed.), *Pre-Mesozoic Geology of Iberia*, Springer-Verlag, Berlin-Heidelberg-New York-London-Paris-Tokyo-Hong Kong-Barcelona, pp. 148-159.

Kwak, T. A. K., 1987. *W-Sn skarn deposits and related metamorphic skarns and granitoids*. Elsiever Science Publishers B.V., Amsterdam-Oxford-New York-Tokyo, 451 pp.

Klein, C., Dutrow, B., 2008. *The 23rd Edition of the Manual of Mineral Science (after James D. Dana)*. John Wiley & Sons, Inc., United States of America, 675 pp.

Kuznetzova, A., 2012. *Stochastic simulation of the morphology of fluvial sand channels reservoirs*. Unpublished M.Sc. thesis. NOVA University of Lisbon, Lisbon, 66 pp.

Marques, I., Almeida, J., Legoinha, P., 2015. Generation of turbidite channel structure morphology using object-based model conditional to multipoint statistics. *V Congresso de Jovens Investigadores em Geociências, LEG 2015*, Estremoz, 2015, Scientific Programme and Abstracts, 31-34.

Martins, L. P., 2012. *Mineral Resources of Portugal*. Direcção Geral de Energia e Geologia, Lisbon, 71 pp.

Matias, F. V., 2010. *Modelação 3D de um Subsector das Mineralizações Auríferas de Casas Novas, Montemor-o-Novo*. Unpublished M.Sc. thesis. NOVA University of Lisbon, Lisbon, 121 pp.

Matias, F. V., Almeida, J. A., Chichorro, M., 2015. A Multistep Methodology for Building a Stochastic Model of Gold Grades in the Disseminated and Complex Deposit of Casas Novas in Alentejo, Southern Portugal. *Resource Geology*, 65(4): 361-374.

McHargue, T., Pyrcz, M. J., Sullivan, M. D., Clark, J. D., Fildani, A., Romans, B. W., Covaul, J. A., Levy, M., Posamentier, H. W., Drinkwater, N. J., 2011. Architecture of turbidite channel systems on the continental slope: Patterns and predictions. *Marine and Petroleum Geology*, 60: 121-139.

Meinert, L., 1992. Skarns and Skarn Deposits. *Geoscience Canada*, 19 (4): 145-162.

Meinert, L., Dipple, G. M., Nicolescu, S., 2005. World Skarn Deposits. *Economic Geology 100th Anniversary Volume*: 299-336.

Meireles, C., Castro, P., Ferreira, N., 2013. New data on the lithostratigraphy of Beiras Group (Schist Greywacke Complex) in the region of Góis-Arganil-Pampilhosa da Serra (Central Portugal). *Cadernos do Laboratório Xeolóxico de Laxe*, 37: 105-124.

Moura, A., Velho, J. L., 2012. *Recursos Geológicos de Portugal*. Palimage, Coimbra, 571 pp.

Murton, J. W., 2007. *NI 43-101 Technical Report on the Penedono Gold Concession (Northern Portugal)*. Unpublished technical report. J. W. Murton & Associates, Kelowna, 78 pp.

Neiva, A. M. R., 2001. Geochemestry of Granites from Northern and Central Portugal Associated with Tin and Tungsten Mineralizations. *Memórias da Academia das Ciências de Lisboa: Classe de Ciências*, XXXXIX: 145-159.

Neiva, A. M. R., 2002. Portuguese granites associated with Sn-W and Au mineralizations. *Bulletin – Geologial Society of Finland*, 74: 79-101.

Neiva, J. M. C., 1979. Alterações metassomáticas nas rochas encaixantes de jazigos minerais de diferenciação granítica. *Memórias e Notícias*, 88: 45-59.

Noronha, F., Ribeiro, M. A., Almeida, A., Dória, A., Guedes, A., Lima, A., Martins, H. C.,

Sant'Ovaia, H., Nogueira, P., Martins, T., Ramos, R., Vieira, R., 2013. II.1.8. Jazigos filonianos hidrotermais e aplitopegmatíticos especialmente associados a granitos (norte de Portugal). *In*: Dias, R., Araújo, A., Terrinha, P., Kullberg, J. C. (Ed.), *Geologia de Portugal: Volume I – Geologia Pré-mesozóica de Portugal*, Escolar Editora, Lisbon, pp. 403-438.

O'Donovan, 2012. *Tabuaço Tungsten Project, Portugal. NI 43-101 Technical Report*. Unpublished technical report. SRK Exploration Services Limited, Cardiff, 99 pp.

Pereira, M. F., Linnemann, U., Hofmann, M., Chichorro, M., Solá, A. R., Medina, J., Siva, J. B., 2012. The provenance of Late Ediacaran and Early Ordovician siliciclastic rocks in the Southwast Central Iberian Zone: Constraints from detrital zircon data on northern Gondwana margin evolution during the late Neoproterozoic. *Precambrian Research*, 192-195: 166-189.

Pinto, A. F., 1984. Rochas calco-silicatadas do Complexo Xisto-Grauváquico: mineralogia, geoquímica, evolução genética. *Comunicações dos Serviços Geológicos de Portugal*, 70 (1): 55-62.

Pirajno, F., 1992. *Hydrothermal Mineral Deposits: Principles and Fundamental Concepts for the Exploration Geologist*. Springer-Verlag, Berlin-Heidelberg-New York-London-Paris-Tokyo-Hong Kong-Barcelona-Budapest, 709 pp.

Pirajno, F., 2009. *Hydrothermal Processes and Mineral Systems*. Springer+Business Media B.V., 1250 pp.

Quental, P. A. L. A., 2011. *Modelos Geológicos Estocásticos 3D e Interface para Modelos de Simulação de Fluxo. Aplicação à Área Subjacente da Antiga Fábrica da SPEL*. Unpublished M.Sc. thesis. NOVA University of Lisbon, Lisbon, 73 pp.

Quental, P., Almeida, J. A., Simões, M., 2012. Construction of high-resolution stochastic geological models and optimal upscaling to a simplified layer-type hydrogeological model. *Advances in Water Resources*, 39: 18-32.

Quininha, M. A., 2015. *Simulação de estruturas meandriformes por objectos e estatisticas multiponto e avaliação da porosidade – aplicação a reservatórios silicilásticos*. Unpublished M.Sc. thesis. NOVA University of Lisbon, Lisbon, 85 pp.

Quininha, M., Almeida, J., Legoinha, P., 2015. Multipoint statistics of azimuth angle classes: an application to the simulation of channel structures and the evaluation of porosity in siliciclastic reservoirs . *IAMG 2015*, Freiberg, 2015, Abstracts, 971-980.

Reis, E., 1997. *Estatística Multivariada Aplicada*. Edições Sílabo, Lisbon, 343 pp.

Ribeiro, A., 1990. Introduction. *In*: Dallmeyer, R. D., Garcia, E. M. (Ed.), *Pre-Mesozoic Geology of Iberia*, Springer-Verlag, Berlin-Heidelberg-New York-London-Paris-Tokyo-Hong Kong-Barcelona, pp. 143-144.

Ribeiro, A, 2013a. I. A evolução geodinâmica de Portugal; uma introdução. *In*: Dias, R., Araújo, A.,

Terrinha, P., Kullberg, J. C. (Ed.), *Geologia de Portugal: Volume I – Geologia Pré-mesozóica de Portugal*, Escolar Editora, Lisboa, pp. 12-14.

Ribeiro, A, 2013b. II. Evolução geodinâmica de Portugal: os cilcos ante-mesozóicos. *In*: Dias, R., Araújo, A., Terrinha, P., Kullberg, J. C. (Ed.), *Geologia de Portugal: Volume I – Geologia Pré-mesozóica de Portugal*, Escolar Editora, Lisboa, pp. 15-57.

Ribeiro, A., Pereira, E., 1982. Controles paleogeográficos, petrológicos e estruturais na génese dos jazigos portugueses de estanho e volfrâmio. *GEONOVAS*, 1(3): 23-31.

Robb, L., 2005. *Introduction to ore-forming processes*. Blackwell Publishing, Oxford, 373 pp.

Rodrigues, A. M. S., 2013. *Modelação 3D de teores de depósitos minerais condicionados por tipos de mineralização. O caso de estudo do depósito mineral do Zambojal, Minas de Neves-Corvo*. Unpublished M.Sc. thesis. NOVA University of Lisbon, Lisbon, 70 pp.

Rodrigues, A. M., Almeida, J. A., 2010. Modelação 3D dos teores em cobre e zinco do depósito mineral do Zambujal (Neves-Corvo) condicionados por tipos de minério. *Comunicações Geológicas* 101, Especial III: 1647-1428.

Rossi, M. E., Deutsch, C. V., 2014. *Mineral Resources Estimation*. Springer Science+Business Media, Dordrecht-Heidelberg-New York-London, 332 pp.

Roxo, S. C. M., 2011. *Integração de informação secundária na modelação geostatistica da qualidade de solos em locais potencialmente contaminados. Aplicação à area subjacente a uma antiga refinaria*. Unpublished M.Sc. thesis. NOVA University of Lisbon, Lisbon, 64 pp.

Silva, A. F., 2005. *A litoestratigrafia e estrutura do Supergrupo Dúrico-Beirão (Complexo Xisto-Grauváquico), em Portugal, e sua correlação com as correspondentes sucessões em Espanha*. Unpublished technical report. Instituto Nacional de Engenharia, Tecnologia e Informação, Lisbon, 32 pp.

Silva, D. M., Almeida, J., 2015a. The use of rock density for improving morphological and metal grade models of the Zambujal sulphide ore deposit. *IAMG 2015*, Freiberg, 2015, Abstracts, 1075-1084.

Silva, D. M., Almeida, J. A., 2015b. Modeling Metal Grades of a Sulfide Ore Deposit Using the Rock Density as a Morphological Proxy (Neves-Corvo Mine). *V Congresso de Jovens Investigadores em Geociências, LEG 2015*, Estremoz, 2015, Scientific Programme and Abstracts, 39-43.

Simões, T. H., 2014. *Modelação automática 2D de mineralizações filonianas – aplicação às Minas da Panasqueira*. Unpublished M.Sc. thesis. NOVA University of Lisbon, Lisbon, 58 pp.

Silva, M. M. V. G., Neiva, A. M. R.,1990. Geochemestry of the granites and their minerals from Paredes da Beira-Penedono, northern Portugal. *Chemical Geology*, 85: 147-170

Soares, A., 2006. Direct Sequential Simulation and Cosimulation. *Mathematical Geology*, 33: 911-

926.

Soares, A., 2006. *Geostatística para as Ciências da Terra e do Ambiente*. IST Press, Lisbon, 214 pp.

Sousa, M. B., 1979a. O Complexo Xisto-Grauváquico do Douro. I – Características litoestratigráficas. *Memórias e Notícias*, 88: 31-37.

Sousa, M. B., 1979b. O Complexo Xisto-Grauváquico do Douro. II – Os Conglomerados de Trevões (S. João da Pesqueira, NE Portugal) e seu significado estratigráfico. *Memórias e Notícias*, 88: 39-44.

Sousa, M. B., Ramos, J. M. F., Viegas, L. F. S., 1979. Skarns da região de Tabuaço – Importância da sua descoberta para a prospecção de novas ocorrências. *Boletim de Minas*, 16 (3/4): 109-214.

Sousa, M. B., 1981. Skarns e rochas calco-silicatadas do Complexo xisto-grauváquico do Douro (NE Portugal) – seu enquadramento litoestratigráfico. *Comunicações dos Serviços Geológicos de Portugal*, 67 (2): 169-172.

Sousa, M. B., 1982. *Litostratigrafia e estrutura do "Complexo Xisto-Grauváquico Ante-Ordovícico" – Grupo do Douro Nordeste de Portugal*. Unpublished Ph.D. thesis. University of Coimbra, Coimbra, 222 pp.

Sousa, M. B., 1983. Litoestratigrafia do CXG – Grupo do Douro (NE Portugal). *Memórias e Notícias*, 95: 3-63.

Sousa, M. B., 1985. Perspectiva sobre os conhecimentos actuais do Complexo Xito-Grauváquico de Portugal. *Memórias e Notícias*, 100: 1-16.

Sousa, M. B., Sequeira, A. D., Santos, A. J., Neiva, J. C., Neiva, A., Azevedo, M., Ferreira, N., Francisco, S., Meireles, M., Santos, J., 1987. *Carta Geológica de Portugal na escala 1/50 000 Folha 10-D Alijó*. Direcção Geral de Geologia e Minas, Lisbon.

Sousa, M. B., Sequeria, A. J. D., 1989. *Notícia Explicativa da Folha 10-D Alijó da Carta Geológica de Portugal na escala 1/50* 000. Serviços Geológicos de Portugal, Lisbon, 59 pp.

Sousa, M. B., Ramos, J. M. F., 1991. Características geológico-estruturais e químico-mineralógicas das jazidas auríferas da região de Penedono-Tabuaço (Viseu, Portugal). *Estudos, Notas e Trabalhos, D.G.G.M.*, 33: 71-96.

Srivastava, R. M., 2005. Probabilistic Modeling of Ore Lens Geometry: An Alternative to Deterministic Wireframes. *Mathematical Geology*, 37: 513-544.

Thadeu, D., 1977. Hercynian paragenetic units of the Portuguese part of the Hesperica Massif. *Boletim da Sociedade Geológica de Portugal*, XX(III): 247-276.

Vilas, L., José, M. A. S., 1990. 2.1.1 Introduction. *In*: Dallmeyer, R. D., Martinez Garcia, E. (Ed.), *Pre-Mesozoic Geology of Iberia*, Springer-Verlag, Berlin-Heidelberg-New York-London-Paris-

Tokyo-Hong Kong-Barcelona, pp. 145-146.

Villaseca, C., Merino, E., Oyarzum, D., Orejana, D., Pérez-Soba, C., Chicharro, E., 2014. Contrasting chemical and isotopic signatures from Neoproterozoic metasedimentary rocks in the Central Iberian Zone (Spain) of pre-Variscan Europe: Implications for terrane analysis and Early Ordovician magmatic belts. *Precambrian Research*, 245: 131-145.

Zuo, R., Zhang, Z., Zhang, D., Carranza, E. J. M., Wang, H., 2015. Evaluation of uncertainty in mineral prospectivity mapping due to missing evidence: A case study with skarn-type Fe deposit in Southwestern Fujian Provnce, China. *Ore Geology Reviews*, 71: 502-515.